THE UNIVERSITY *of* EDINBURGH

THE UNIVERSITY OF EDINBURGH

A measurement of the effective lifetime of the B_s^0 meson using the flavour specific decay $B_s \to D_s^- \pi^+$ at the LHCb experiment.

by

Gemma Fardell

A thesis submitted in partial fulfillment for the
degree of Doctor of Philosophy

in the
The College of Science and Engineering
School of Physics and Astronomy

May 2013

Declaration of Authorship

The work contained in this thesis was carried out within the LHCb collaboration, and as such represents the combined effort of myself and many others throughout the experiment. The composition of this thesis is entirely my own work. The work has not been submitted for any other degree or professional qualification.

(G. C. Fardell)

I keep six honest serving-men
    (They taught me all I knew);
Their names are What and Why and When
    And How and Where and Who.

The Elephant's Child
Rudyard Kipling

Acknowledgements

I am grateful to both STFC and Edinburgh University for providing funding for my Ph.D. and giving me the opportunity to contribute to our understanding of fundamental physics.

This thesis would not have been possible without my Ph.D. supervisor, Professor Peter Clarke, whose knowledge and enthusiasm for physics are second to none. Thank you for putting up with missed deadlines and late meetings, I got there in the end thanks to you.

Greig Cowan has provided invaluable help throughout my Ph.D. with everything from computing support to analysis advice. I owe Greig and Ben Wynne more than a few beers for developing RapidFit, the Edinbugh fitting software, without which this analysis would not have been possible.

I owe my deepest gratitude to my parents. My father I have to thank for my love of physics, thank you for not only putting up with, but for encouraging my questions and always helping me find answers. Thanks to mother who put up with me living at home throughout my write up, thank you for all the dinners and cups of tea that helped fuel my work.

Thank you to Sam, Laurence and Michele, post-docs in different groups and on different experiments who always had time to spare if I asked for help.

Last but not least, my warmest thanks to all my friends, old and new, that have helped make the last few years so enjoyable, for the winter sports, and free sofas and cheese based meals; above all Sara, Kitty, Chrissy, James, Julia, Ross and Hajrah deserve special mentions, without the stress-relief and coffee breaks we shared I would have fallen at the first hurdle.

Abstract

This thesis presents a measurement of the effective B_s^0 decay width, Γ_{FS}, from a single-exponential fit to the flavour-specific decay channel $B_s^0 \to D_s^- \pi^+$.

This measurement is based on an integrated luminosity of $340\,\mathrm{pb}^{-1}$ recorded by LHCb in 2011 at a center of mass energy of 7 TeV.

The dataset is divided into two exclusive selections. $B_s^0 \to D_s^-((\phi \to K^-K^+)\pi^-)\pi^+$ only has a significant background contribution arising from combinatorial background, and the modelling of this is determined entirely by the data. $B_s^0 \to D_s^-((K^-K^*(892)^0 \to K^+\pi^-))\pi^+$ has a larger contribution from combinatoric and mis-identified background and provides an alternative measurement.

A simultaneous fit for the effective B_s^0 decay width is performed to both the datasets leading to the result:

$$\Gamma_{FS} = 0.668 \pm 0.017 \pm 0.031\,\mathrm{ps}^{-1}$$

The result is then combined with information from the LHCb $B_s^0 \to J/\psi\phi$ analysis leading to an improved measurement of the average B_s^0 decay width:

$$\Gamma_s = 0.666 \pm 0.010 \pm 0.031\,\mathrm{ps}^{-1}$$

Contents

List of Figures

List of Tables

For my friend Matthew Fearn, whose memory keeps me smiling.

Chapter 1

Introduction

1.1 Particle Physics

In 1896 the British physicist J. J. Thomson discovered the electron [2] and particle physics was born. Over the next century thousands of physicists have worked towards theories and discoveries that have shaped our understanding of the universe. Probing the structure of matter we have found that everything in the universe is made from 12 fundamental particles, and governed by four fundamental forces. Our best understanding of how these building blocks of the universe relate to each other is encapsulated in the Standard Model of particle physics. The Standard Model was developed in the 1970s and since then has successfully explained and predicted a wide variety of experimental results.

Despite the Standard Model's experimental successes it is incomplete. Three of the most fundamental questions we can ask about our universe remain unanswered:

- What is mass?
- What is 96% of the universe made of?
- Why is there no more antimatter?

It is hoped that CERN, with the help of the LHC, will start to be able to answer these.

1.2 CERN and the LHC

CERN, the European Organization for Nuclear Research, was founded in 1954 with the mandate of establishing a world-class fundamental physics research organization in Europe [3]. It straddles the French-Swiss border and is one of the world's largest science laboratories. The majority of CERN users are currently working at the Large Hadron Collider (LHC), and the experiments for it.

The LHC is the world's highest energy particle accelerator. It is situated in the 27 km long former Large Electron-Positron Collider (LEP) tunnel and is designed to accelerate two proton beams to 7 TeV. There are four main interaction points where there are detectors located. These include the ATLAS detector, ALICE detector, CMS detector and LHCb detector at underground point 8. These are shown in Figure 1.1 [4].

The LHC first entered beam commissioning in September 2008, however after 9 days of running a fault occurred in the electrical connection between two of the superconducting dipole magnets. This produced an electrical arc which compromised the liquid-helium containment. The shock wave produced from the liquid-helium filling the vacuum was sufficient to break the 10 tonne magnets from their mountings and stop LHC operation for a year.

Proton beams were successfully circulated once more in November 2009 with beam energies of 450 GeV. Shortly after the circulating beams reached an energy of 1.18 TeV per beam, surpassing the previous record held by the Tevatron at Fermilab.

On 30th March 2010 the LHC achieved an energy 3.5 TeV per beam which is the energy the 2011 data this analysis uses was generated at. The LHC will continue at this energy until further upgrades are undertaken this year.

1.2.1 The Beam and Magnets

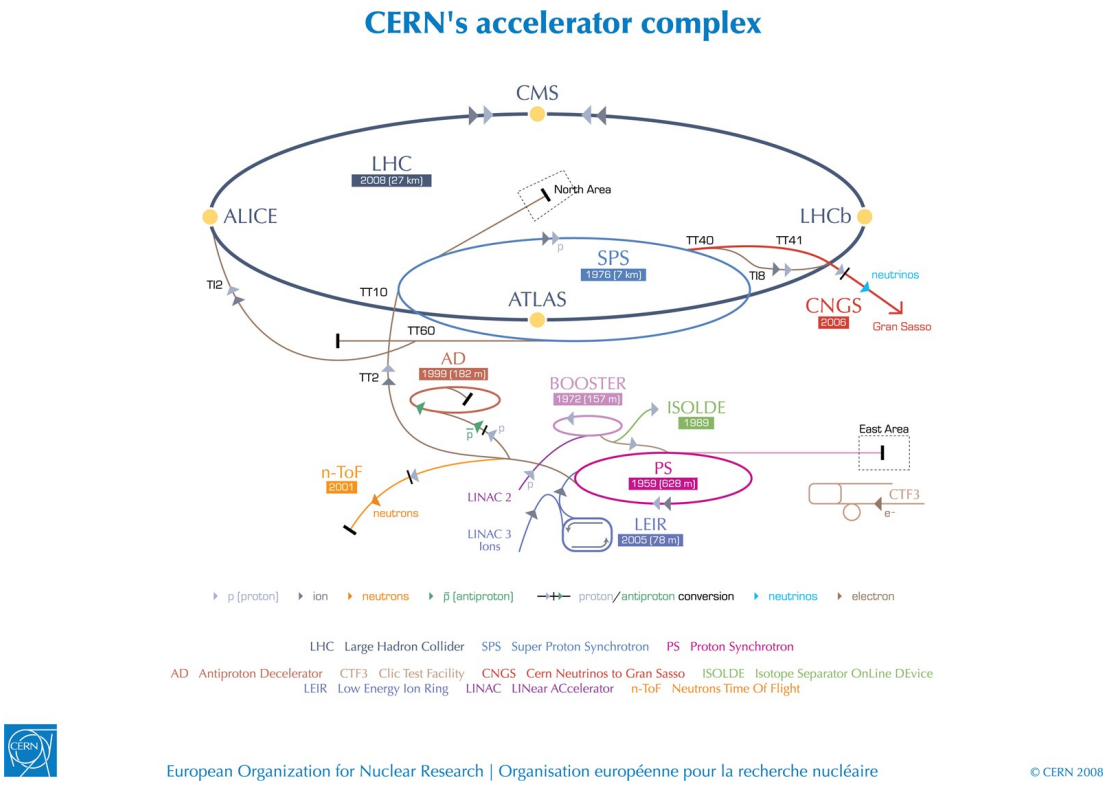

FIGURE 1.1: The LHC is the last ring (dark grey line) in a complex chain of particle accelerators. The smaller machines are used in a chain to help boost the particles to their final energies and provide beams to a whole set of smaller experiments.

The performance requirements of the LHC set significant challenges for the design and construction of the accelerator. The LHC is the last part of a series of accelerator systems that produce and accelerate the beam in stages.

The booster rings to the LHC are illustrated in Figure 1.1. The first system is the linear particle accelerator (LINAC 2) which generates 50 MeV protons that are fed into the Proton Synchrotron Booster (PSB). Within the PSB the protons are accelerated to 1.4 GeV and injected into the Proton Synchrotron (PS), where the protons energy reaches 26 GeV. The last stage before entering the LHC is the SPS which is used to further increase the proton energy to 450 GeV before they are at last injected into the

LHC. Within the LHC the protons are accumulated into bunches of $\sim 10^{11}$ particles that are then accelerated up to the desired energy.

To keep the beams circulating within the ring the LHC uses 1,232 dipole magnets, shown in Figure 1.2 [5], which cover $\sim 20\,\text{km}$ of the ring length. The beam is focused using quadrupole magnets, of which there are 392 used along the straight sections of the ring.

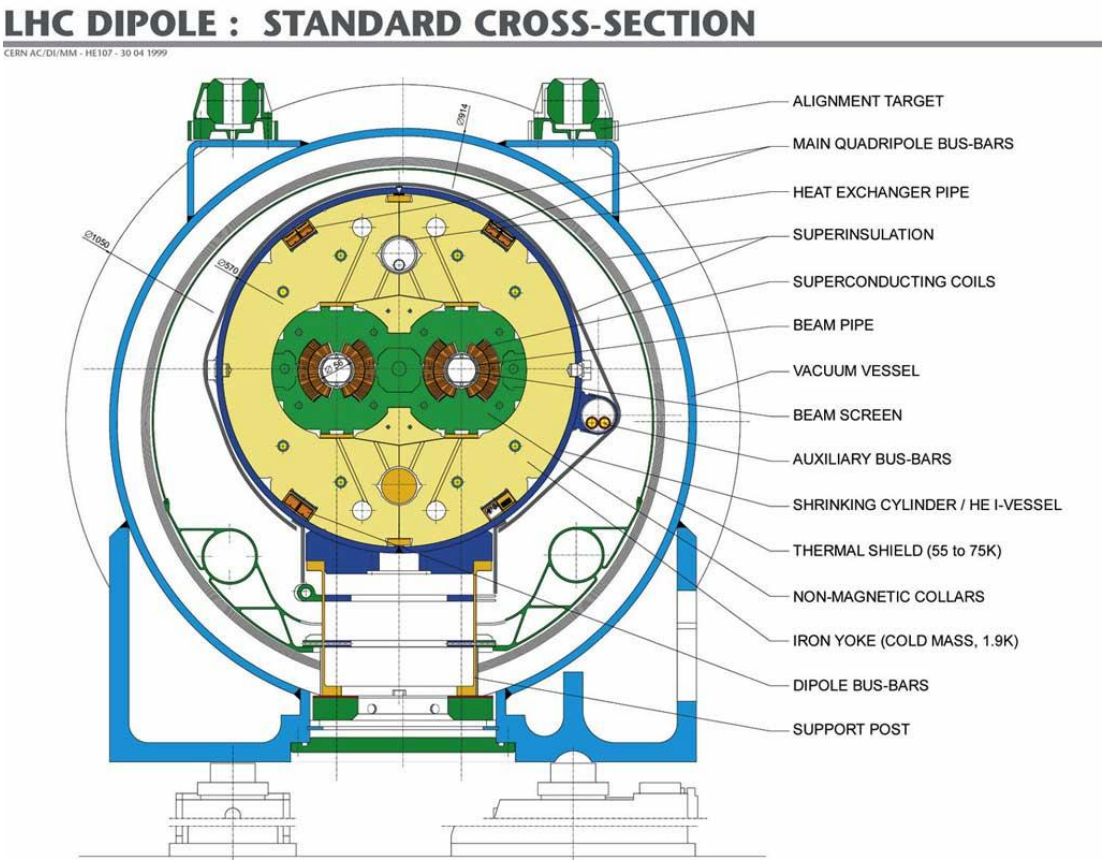

FIGURE 1.2: Cross section of the LHC dipole magnet system

The luminosity, the number of events per unit cross-section per unit time of a circulating accelerator is given by:

$$\mathcal{L} = nf\frac{N_1 N_2}{A}$$

where there are n bunches in each beam revolving at a frequency f, with N_1 and N_2 particles in the colliding bunches with an overlapping area of A.

The design luminosity of the LHC is $10^{34}\,\mathrm{cm}^{-2}\mathrm{s}^{-1}$, providing a bunch collision rate of 40 MHz [6]. LHCb however is optimised around a reduced luminosity of $2 \times 10^{32}\,\mathrm{cm}^{-2}\mathrm{s}^{-1}$. At the LHCb luminosity the bunch crossings are dominated by single interactions.

The LHC is primarily a 'discovery machine' with the focus of the physics programmes being searches for signatures of new physics. The high luminosity and increased cross-sections at the LHC will also enable high precision tests of QCD, electroweak interactions and flavour physics.

1.3 Thesis Introduction

This thesis will focus on the decay width measurements in the $B_s \to D_s\pi$ channel and present a model for a simultaneous fit to various signal selections. The thesis is divided into 9 chapters outlined here:

- **Chapter 2 - The LHCb Detector:** describes the LHCb experiment and gives a technical overview of its sub-detectors.
- **Chapter 3 - Theoretical Motivation:** introduces the relevant theory pertaining to decay width and lifetime measurements and defines the key definitions and terms for this analysis.
- **Chapter 4 - Lifetime Measurements in HEP:** focuses on the experimental difficulties of lifetime and decay width measurements. It also presents the current world average and LHCb results for related lifetime parameters.
- **Chapter 5 - The $B_s \to D_s^-\pi^+$ Decay:** introduces the $B_s^0 \to D_s^-\pi^+$ channel and the signal selection. The backgrounds to the analysis are identified here.
- **Chapter 6 - Fitting to Monte Carlo Data:** presents mass and decay width fits to LHCb Monte Carlo in an effort to understand the data.

- **Chapter 7 - Lifetime Fitting Results:** presents the fit results from LHCb data.
- **Chapter 8 - Systematic Uncertainties:** gives a study of the systematic uncertainties pertaining to the result.
- **Chapter 9 - Conclusion** presents the final result.

Chapter 2

The LHCb Detector

2.1 The LHCb Detector

The LHCb detector is a single-arm spectrometer built along the beam-pipe. A right-handed co-ordinate system has been adopted, with the z-axis along the beam, and the y-axis along the vertical. A schematic of the detector is shown in Figure 2.1 [7]. A full description of the sub-components of the detector are given in this chapter.

LHCb is a dedicated b-physics experiment, designed to exploit the large quantity of B-hadrons produced at the LHC. The $b - \bar{b}$ cross-section at 14 TeV is estimated to be $\sim 500\,\mu$b, hence LHCb will see much greater yields than previous b-physics experiments. At 7 TeV the cross-section has been measured to be $284\,\mu$b.

The detector geometry is motivated by the high rapidity of $b\bar{b}$ quarks, causing B-hadrons to be produced in forward and backwards cones around the beam-pipe. Figure 2.2 shows a PYTHIA simulation of the polar-angles of the $b\bar{b}$ quark production at the LHC [8]. The LHCb detector has a minimum angular acceptance of ~ 15 mrad, and an upper acceptance of ± 250 mrad in the non-bending $(y - z)$ plane, and ± 300 mrad in the bending $(x - z)$ plane. It is able to measure particle tracks with pseudo-rapidities

in the range $1.6 - 4.9$. LHCb's acceptance makes it sensitive to 34% of the B mesons produced at point 8.

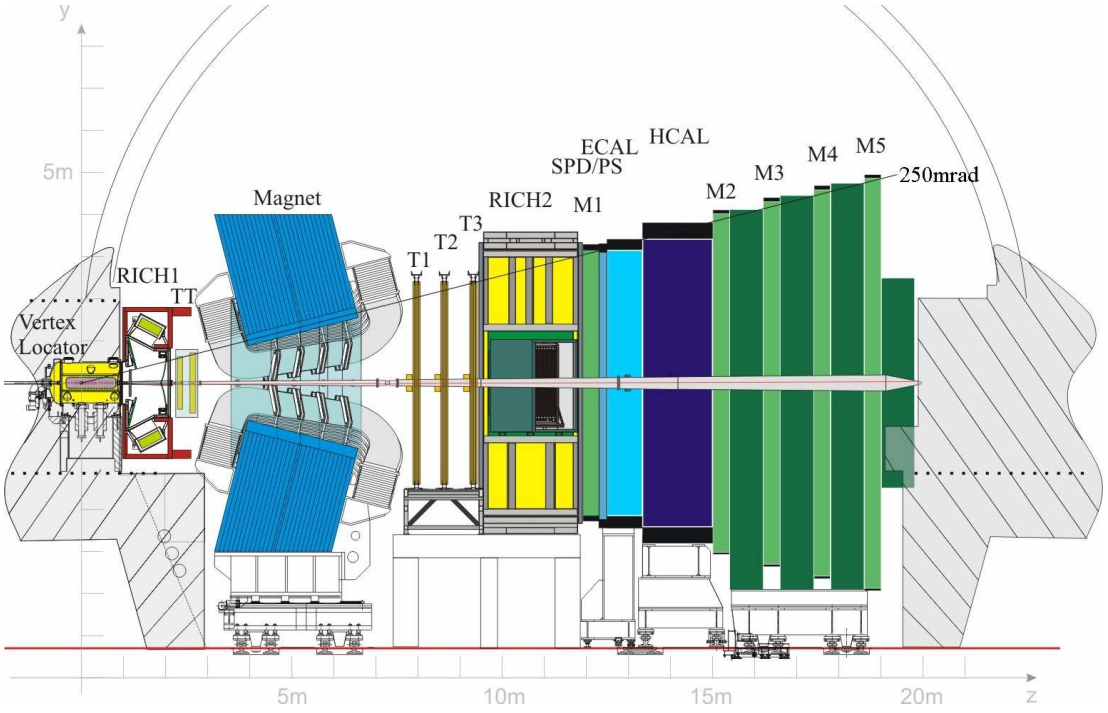

FIGURE 2.1: A schematic diagram of the LHCb detector

The sub-detectors of LHCb are labelled in Figure 2.1. Surrounding the interaction point (the left of the image) is the Vertex Locator (VELO), as we move downstream there are the tracking systems (TT, T1, T2, T3), two ring image Cherenkov detectors (RICH1, RICH2), electromagnetic and hadronic calorimeters (ECAL, HCAL) and a muon detection system (M1-M5).

2.2 The Tracking System

The LHCb tracking system consists of the Vertex Locator (VELO) and four tracking stations; the Trigger Tracker (TT) upstream of the dipole magnet and T1-T3 downstream of the magnet. The VELO and TT use silicon microstrip detectors. In T1-T3,

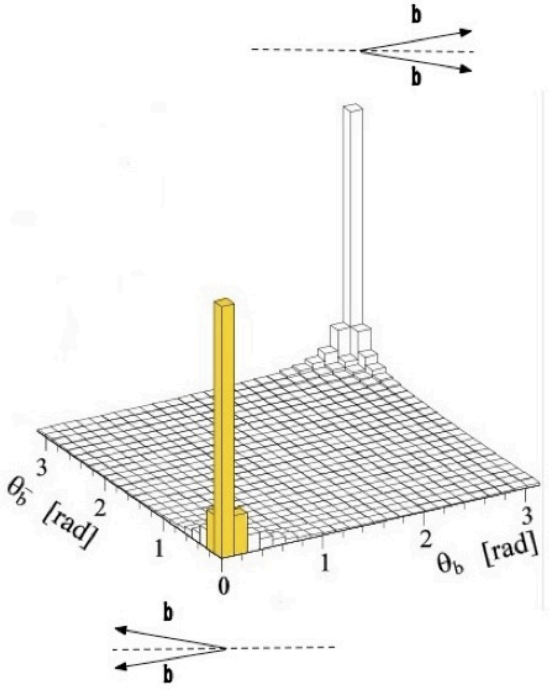

FIGURE 2.2: The angular distribution of $b\bar{b}$ quark production at the LHC, LHCb's acceptance region is marked in yellow.

the detectors are comprised of two distinct sections; the Inner Tracker (IT) in the region closest to the beam-pipe, and the Outer Tracker (OT) in the outer regions of the trackers.

2.2.1 The Beam-Pipe

LHCb focuses on the high rapidity regions and hence the particle density is high. The number of secondary particles observed is heavily influenced by the amount of material seen by the primary particle so the material, bellows and flanges of the beam-pipe have been carefully designed to minimise this. Of the 18 m length of beam-pipe within the LHCb, 12 m is constructed of Beryllium, due to its high transparency to the particles. The remaining 6 m, at points where transparency is not crucial, is constructed from aluminium.

2.2.2 The Magnet

The magnet is situated downstream of RICH1 and upstream of the first tracking station T1. The LHCb experiment uses a warm dipole magnet to measure the momentum of charged particles. The magnetic field is vertically orientated and the integrated magnetic field of the magnet is 4 Tm which gives a resolution of 0.4% for momenta up to $200GeV\,c^{-1}$. The field has been mapped and is known to a precision of $\frac{\sigma_B}{B} = 4 \times 10^{-4}$.

The polarity of the magnet is able to be reversed allowing studies of detector asymmetry, which could impact CP violation measurements. Figure 2.3 plots the magnetic field along the z-axis [7].

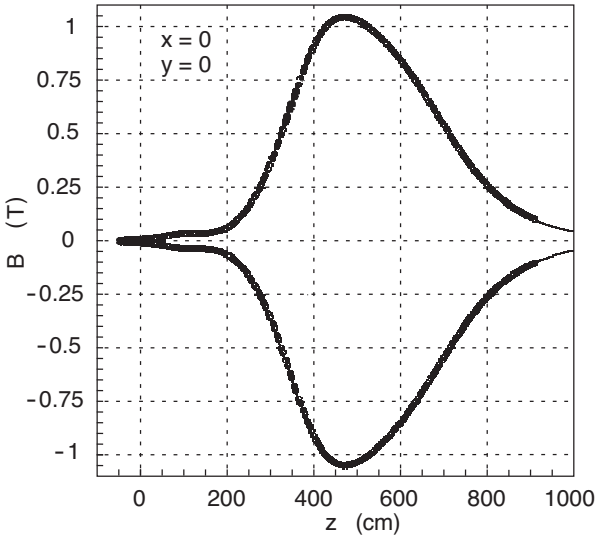

FIGURE 2.3: The magnetic field along the z-axis

2.2.3 The VELO

The VELO is a silicon micro-strip detector designed to provide precise tracking information close to the collision point. The VELO allows the measurement of decay vertex locations, and for b-physics it is is particularly useful to locate and measure the secondary vertices of B decays.

The VELO is of two interlocking halves, each half consists of 21 semicircular hybrids of 300 μm thick silicon strip detectors which surround the beam-pipe. The VELO halves are retractable by 3 cm; this allows them to be moved as the nominal radial distance of the VELO to the beam is smaller than the aperture required by the LHC during injection. During stable LHC running the innermost tracking strips sit within 8 mm of the beam. Figure 2.4 shows a schematic cross-section of the VELO as well as a view of the hybrids in the open and closed position [7].

Each hybrid consists of two back-to-back sensor modules, as shown in Figure 2.5 [7], one measuring the radial (r) and the other measuring the azimuthal (ϕ) co-ordinate of each track. Each module contains 2048 silicon strips, either radial or azimuthal, covering a radius surrounding the beam-pipe of $8 - 42$ mm [9].

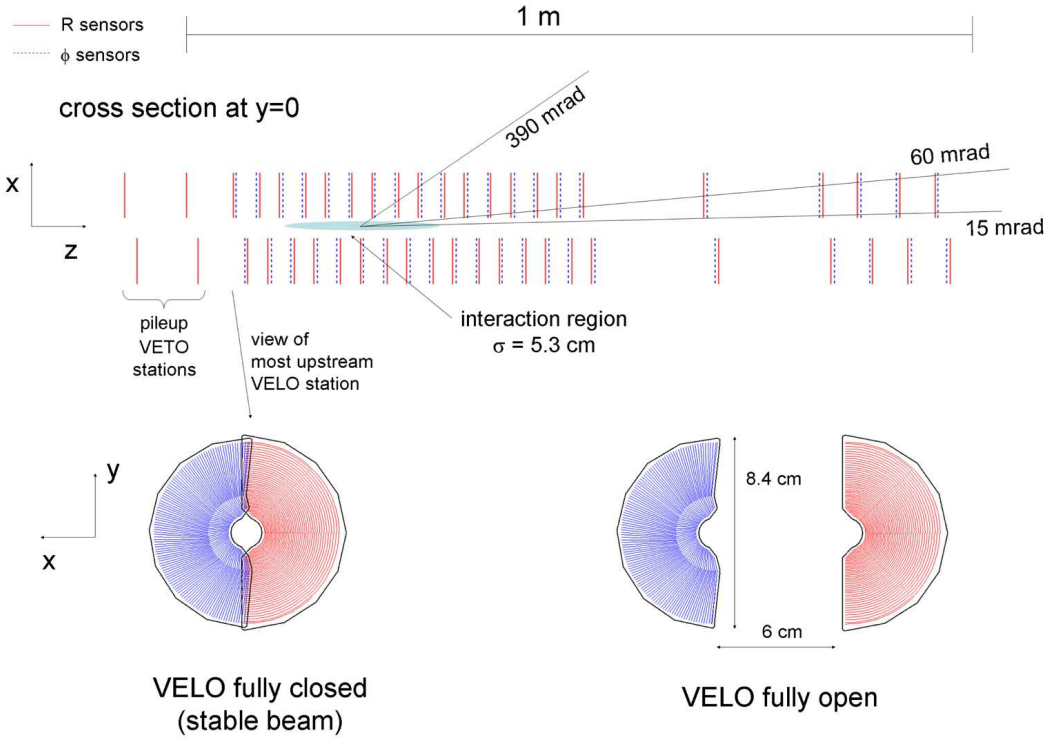

FIGURE 2.4: (top) A cross-sectional view of the VELO in the xz plane at y = 0 and (bottom) two hybrids in the closed and open positions

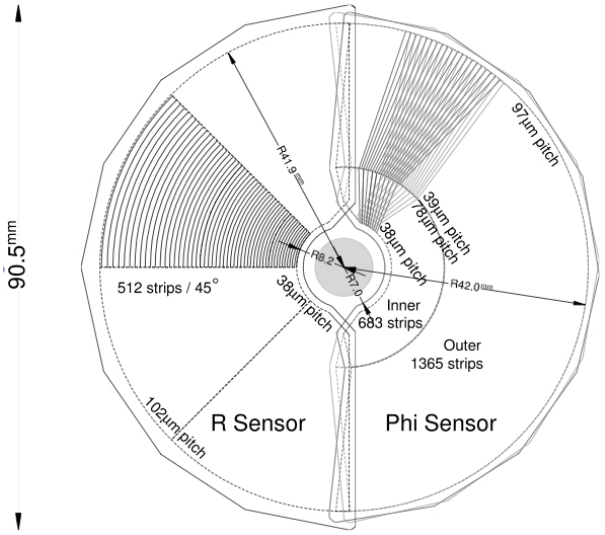

FIGURE 2.5: A schematic of the VELO hybrid showing the r and ϕ modules in each hybrid.

The pileup counters consist of four additional radial modules behind the interaction point and are used as part of the LHCb trigger to reject events with multiple interactions.

The VELO layout has been designed to keep the amount of material within the detector acceptance region to a minimum whilst providing the required geometrical coverage of the charged tracks. Any charged particle produced within the acceptance region will pass through at least 4 stations; allowing one missing hit gives us a guarantee of 3 stations per charged track. The resolution achieved by the VELO in both the r and ϕ directions is 9 μm.

Each VELO half is surrounded by a thin-walled aluminium box, allowing the modules to sit within a vacuum. The outsides of the two boxes have a corrugated shape which allows the two halves to overlap as can be seen in Figure 2.6 [7].

2.2.4 The Tracking Stations

The LHCb detector's tracking stations consist of the Tracker Turicensis (TT), located before the magnet, and three additional stations (T1, T2, and T3) after the magnet.

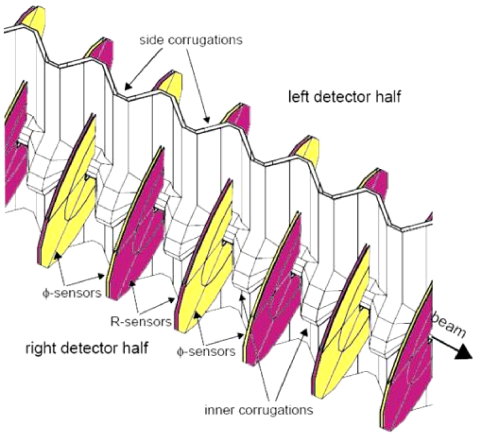

FIGURE 2.6: The VELO hybrids in the aluminium container, demonstrating how the two halves interlock.

The TT is a purely silicon detector, whilst T1-3 are each composed of a silicon inner tracker (IT) and a drift-time outer tracker (OT) [10].

The TT consists of four layers of silicon strip detector layers distributed along the beam axis. The layers are arranged in two pairs, TTa and TTb, separated by $\sim 30\,\text{cm}$ with each layer rotated relative to each other. This is best illustrated graphically in Figure 2.7 [11]. The arrangement of the layers is given the name $x-u-v-x$, where the two outer layers (x) are aligned vertically and hence measure the x co-ordinate, and layers v and u are rotated alignment of $+5^\circ$ and -5° respectively.

In total TTa and TTb stations cover an active area of $8.4\,\text{m}^2$. The sensors of each layer are staggered by 1 cm in the z-direction and overlap by a few mm in the x-direction. The TTa layer is split into 15 vertical ladders which in turn are subdivided into several readout sectors. The TTb layer is split into 17 vertical ladders [10]. Finer segmentation is given to the central sectors to help improve the trigger performance.

The IT does not cover the full acceptance (unlike the TT), but instead covers the high multiplicity region closest to the beam-pipe. A schematic image of the IT is shown by Figure 2.8. The remainder of the acceptance region is covered by the OT. Figure 2.9 [11] gives a view of the tracking stations with the inner and outer tracking regions clearly marked [12].

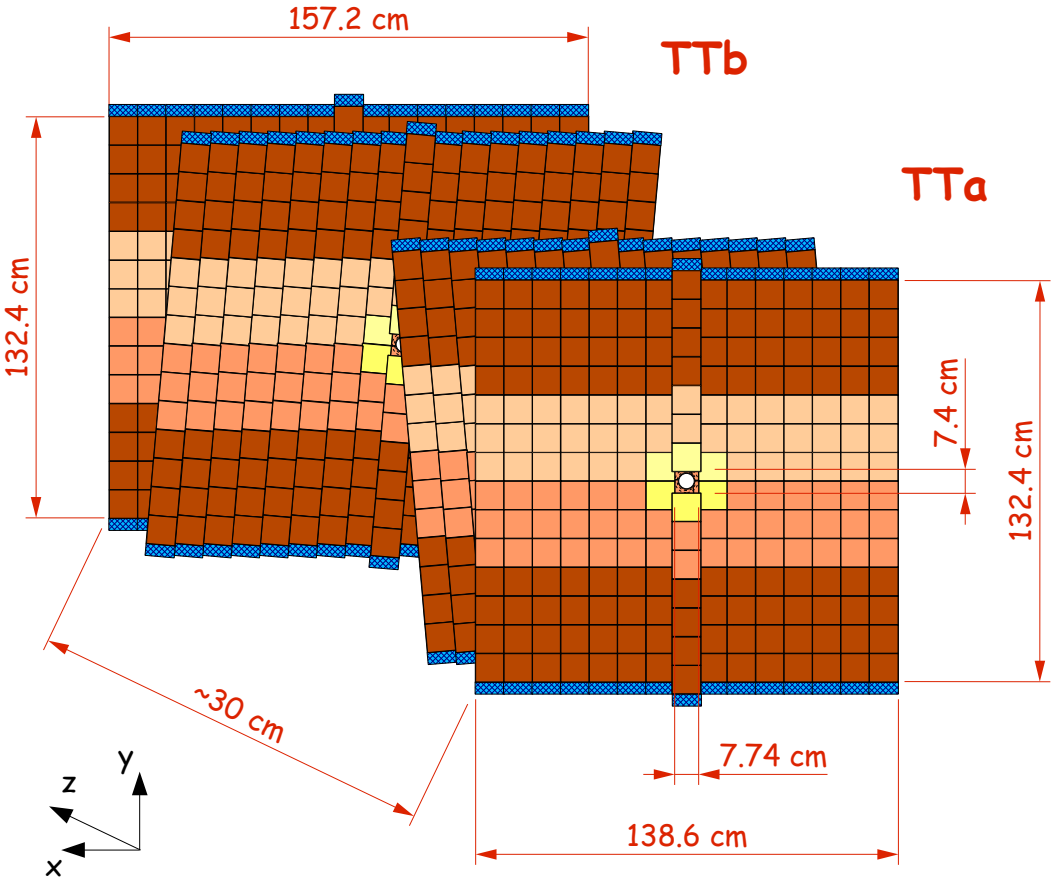

FIGURE 2.7: The Tracker Turicensis is comprised of four silicon-strip layers rotated relative to each other in an $x - u - v - x$ arrangement along the beam-pipe.

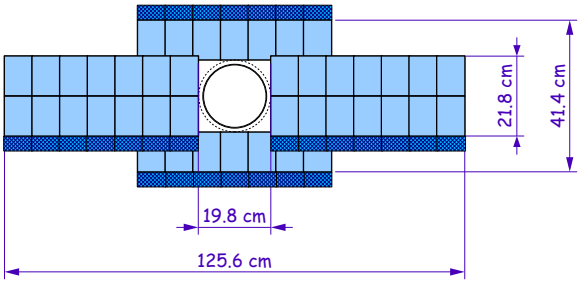

FIGURE 2.8: Image of an inner tracker layer.

Each IT station consists of 4 detector boxes surrounding the beam-pipe each consisting of four layers of silicon detector, again in the $x - u - v - x$ layout. The IT is able to

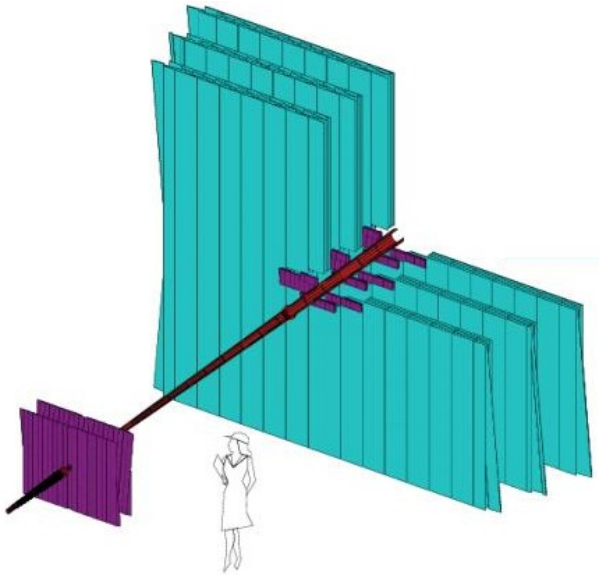

FIGURE 2.9: Image of the tracking stations T1, T2 and T3 showing the Inner and Outer tracker in each.

achieve a spatial resolution of 50 μm.

Surrounding the IT is the OT. The OT sees a lower particle flux than the IT so instead of silicon the OT makes use of straw drift-tubes. Similarly to TT and IT detectors, each OT station is made of two pairs of relatively rotated modules in the $x-u-v-x$ layout. The OT is designed to cover a large area of the LHCb acceptance the total active area of each station being $5.971 \times 4.850\,\mathrm{m}^2$ [13].

The OT is built of four layers of drift-tube modules, each module is composed of two layers of 5 mm diameter straw tubes. Each straw tube is filled with a gas mixture chosen to optimize drift speed, the gas is composed of 75% Argon, 10% CO_2 and 15%CF_4 which yields a maximum drift time of ~ 50 ns with a spatial resolution of $\sim 200\,\mu$m.

2.3 Particle Identification

The LHCb sub-detectors that provide Particle Identification (PID) information are the Ring Imaging Cherenkov Detectors (RICH), the hadronic and electromagnetic calorimeters and the muon chambers. These will be discussed in the following sections.

2.3.1 The RICH

Cherenkov radiation is emitted when a charged particle propagates through a medium at a faster rate than the speed of light in that medium. The phenomenon is analogous to the sonic-boom emitted when the sound barrier is broken. The Cherenkov light is emitted in a cone where the Cherenkov angle θ (defined in Figure 2.10) depends only on the particle's velocity and the refractive index of the medium.

$$\cos\theta = \frac{1}{n\beta} \tag{2.1}$$

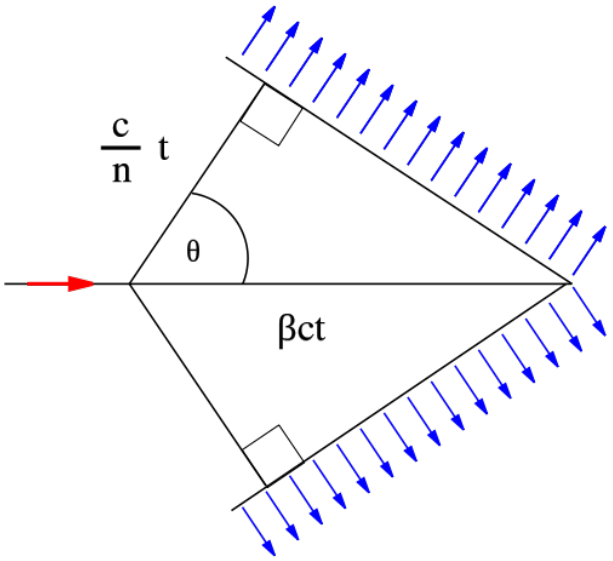

FIGURE 2.10: The geometry of Cherenkov radiation. The particle travels along the x-axis at βc, radiation is emitted at angle θ to the particle's track, and the wavefront travels at $\frac{c}{n}$

The diameter of the photo ring therefore defines the angle θ, and hence the value of β for each charged track.

LHCb has two RICH detectors that identify particles based on this principle. The detectors make use of Hybrid Photon Detectors (HPDs) to detect individual photons and to allow accurate determination of θ. A combination of flat and spherical mirrors are used so the HPDs can be placed outside the LHCb acceptance [14].

RICH1 is situated before the magnet, between the VELO and the TT; it is designed to identify low momentum particles $1 - 60\,\mathrm{GeVc}^{-1}$. A schematic of RICH1 can be seen in Figure 2.11 [10]. The photons are reflected to the HPDs by first spherical mirrors and then larger plane mirrors. RICH1 makes use of two radiators; the first is silica aerogel which has a refractive index of $n = 1.03$ and can separate pions and kaons up to $15\,\mathrm{GeVc}^{-1}$; the second radiator is C_4F_{10} with $n = 1.0014$ which identifies the higher-momentum particles.

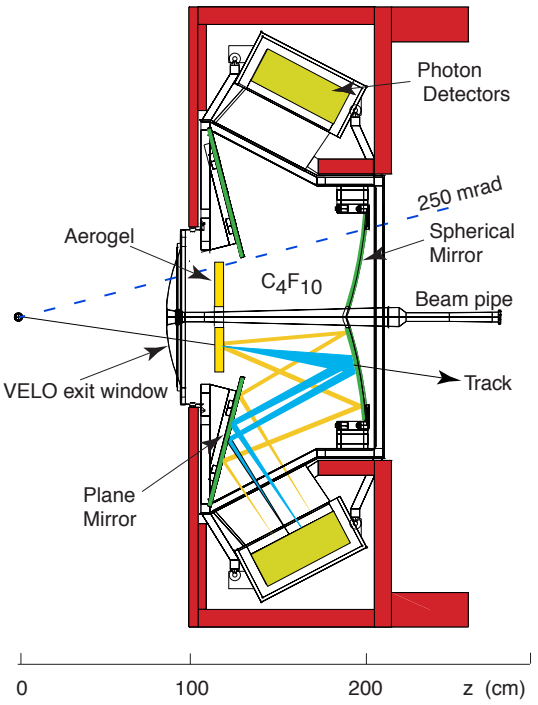

FIGURE 2.11: A schematic of the RICH1 detector

RICH2 is situated downstream of the magnet, between the third tracking station (T3) and the first muon chamber (M1). It is substantially larger than RICH1 and is used for identification of the high momentum $(50 - 150\,\mathrm{GeVc}^{-1})$ particles. RICH2 has a CF_4 gas radiator with refractive index $n = 1.0005$.

HPDs combine vacuum photo-cathode and solid-state technology. A schematic cross-section of an HPD can be seen in Figure 2.12 [15]. A photo-electron is emitted from

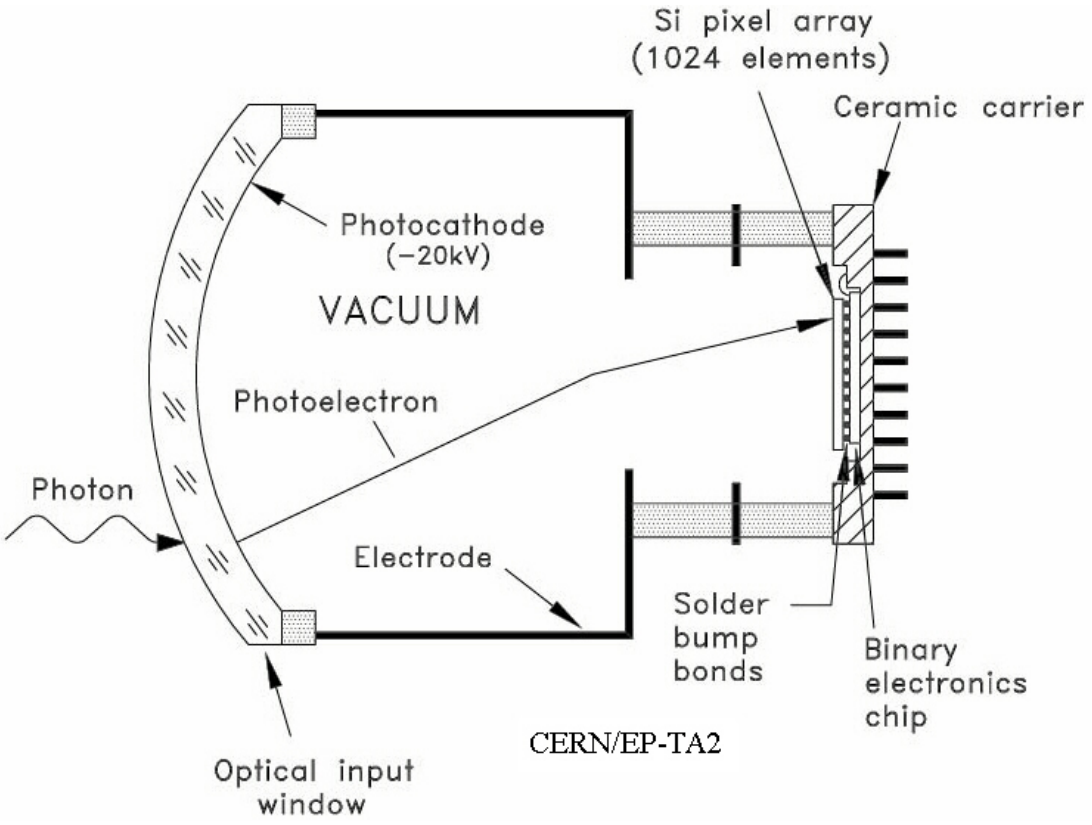

FIGURE 2.12: A schematic of an HPD

the conversion of an incident photon on the photo-cathode. The photo-electron is then accelerated by an applied voltage of $12 - 20\,\mathrm{kV}$ onto a reverse-biased silicon sensor where its energy is then dissipated near the silicon surface. This energy dissipation results in the creation of $3000 - 5000$ electron-hole pairs. The light pattern incident on the photo-cathode is focused onto the silicon detector with collection efficiencies close to 100% making the HPD sensitive to individual photons. RICH1 used 168 HPDs, whereas RICH2 uses 262. In total the HPDs cover an area of $2.6\,\mathrm{m}^2$.

2.3.2 The Calorimeters

The calorimeter system has multiple functions in LHCb. It is primarily used to measure the energy of electrons, photons and hadrons. It is also used by the level-0 trigger to

identify high p_T particles. It provides PID separation between photons and neutral-pions. The calorimeter systems are located between the first and the second muon stations. The detectors which make up the LHCb calorimeters are all comprised of cells which increase in size with distance from the beam and reduction in particle flux.

The calorimeters are divided into four detectors:

- Scintillating Pad Detector/Preshower Detector (SPD/PS)
- Electromagnetic Calorimeter (ECAL)
- Hadronic Calorimeter (HCAL)
- Muon Chambers

The SPD/PS is the part of the calorimeter closest to the collision point consisting of two layers of 15 mm scintillator sandwich a 12 mm lead plate. In conjunction with the ECAL, high p_T neutral pion events which are responsible for a large background are identified and rejected. The scintillation light is collected by a wavelength shifting fibre embedded in the scintillation tiles, and sent via clear fibres to multi-anode photomultiplier tubes placed outside the acceptance.

The ECAL is located directly behind the SPD/PS system. It consists of 120 μm thick Tyvek (a synthetic paper) and 4 mm thick scintillator plates inter-spaced with 66 lead absorber sheets with a thickness of 2 mm. The readout is achieved using wavelength shifting fibres passing through the lead-scintillator stacks to photo-multipliers tubes outside the detector acceptance region. The ECAL structure is segmented into three regions dictated by the distance from the beam-pipe. The modules have the same external dimensions but the number of readout cells varies for each region. The inner part contains 167 modules with 9 readout cells each; the middle section consists of 448 modules with 4 readout cells each; and the outer part 2688 modules containing only one readout cell.

The HCAL is located behind the ECAL detector. The HCAL consists of a sampling structure parallel to the beam and composed of 4 mm thick scintillator plates interspaced with 16 mm iron tiles. The overall material thickness is 1.2 m. The readout is again provided by the wavelength shifting fibres. In the case of the HCAL, the structure is divided into only two regions: the inner and the outer part.

The LHCb Muon System sits furthest from the collision point of the experiment. The muon system provides fast triggering and offline muon identification.

The muon system consists of five stations (M1-M5) of rectangular shape. A schematic diagram of the muon stations and iron filters can be seen in Figure 2.13 [16]. The first station, M1, is located in front of the SPD/PS detector whereas the four other stations are placed behind the HCAL. M2-M5 are separated by 800 mm thick iron filters. The muon would require a momentum of $6\,\mathrm{GeVc}^{-1}$ to traverse the entire muon detection system.

The five stations cover an acceptance of ± 300 mrad horizontally and ± 200 mrad vertically, and a total area of $435\,\mathrm{m}^2$. Each station is further divided into four regions known as R1 - R4, numbered based on their proximity to the beam-pipe.

Gas Electron Multipliers (GEMs) detectors are used in the inner-most region (R1) of Station M1. This is due to GEM detectors having better ageing properties than that of MWPCs [16]. Multi Wire Proportional Chambers (MWPC) are used in all other regions [17]. GEMs and MWPC both consist of a series of gas chambers across which a potential difference of several kV is applied. As a particle traverses each chamber the gas is ionised and the subsequent charge avalanche is proportional to the signal.

2.4 The LHCb Trigger

The LHCb experiment is designed to study the $\sim \times 10^{12}$ $b\bar{b}$ pairs produced at a luminosity of $2 \times 10^{32}\,\mathrm{cm}^{-2}\mathrm{s}^{-1}$. To exploit such high yields the trigger has to be extremely efficient and sensitive to final-states of interest to LHCb analyses.

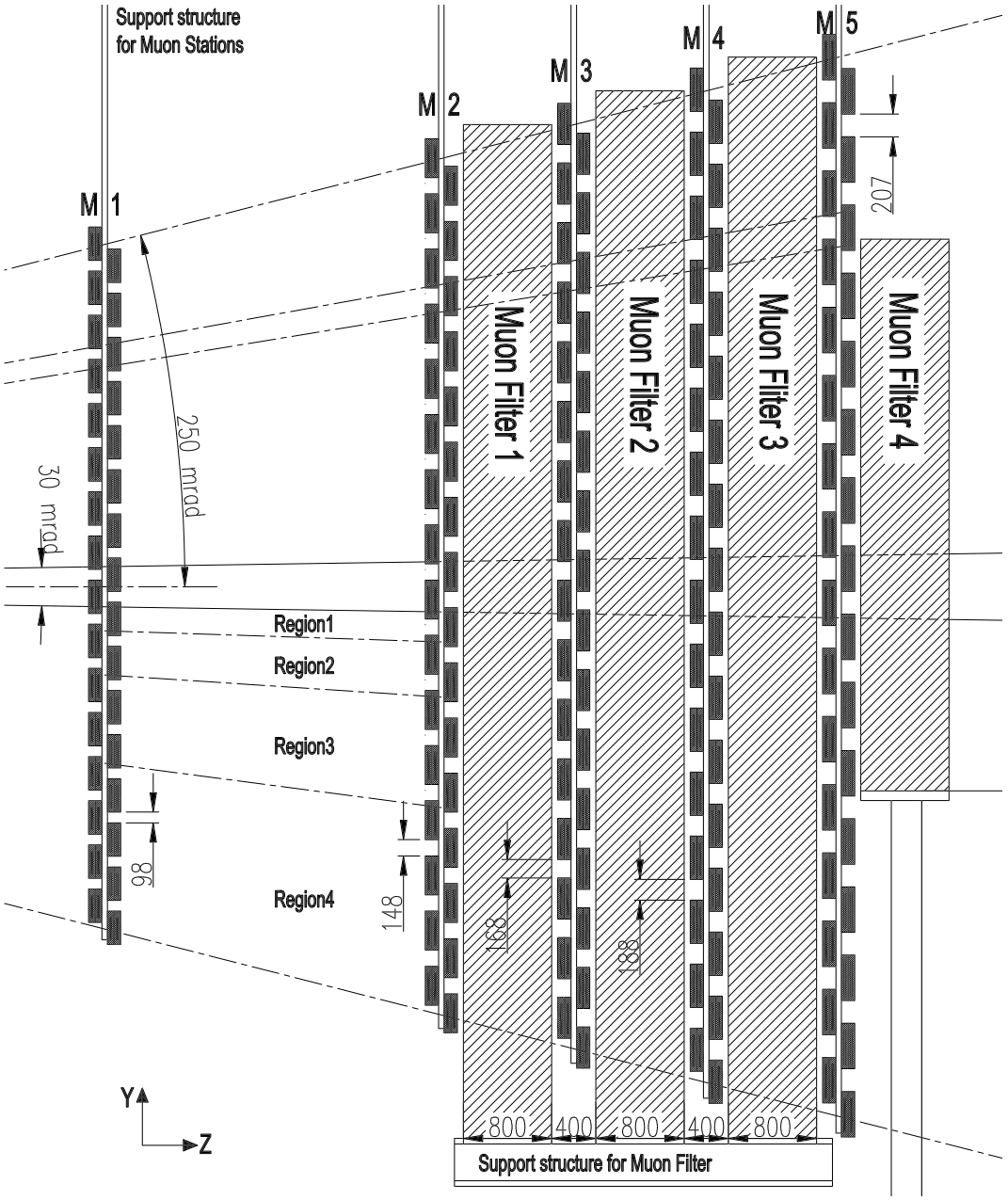

FIGURE 2.13: A schematic view of the Muon Chambers

At this luminosity the number of interactions per bunch crossing is dominated by single interactions. This ensures a low occupancy that allows ease of triggering and reconstructing. Another advantage of running at this lower luminosity is that radiation

damage to the detector is significantly reduced.

The initial visible interactions in LHCb are at a rate of 10 MHz. This is then reduced by a two stage trigger to a few kHz, and at this rate the events can be written to storage. This reduction is achieved initially by the Level-0 (L0) hardware trigger, followed by the High Level Trigger (HLT). A flow diagram of the trigger sequences is shown in Figure 2.14 [7].

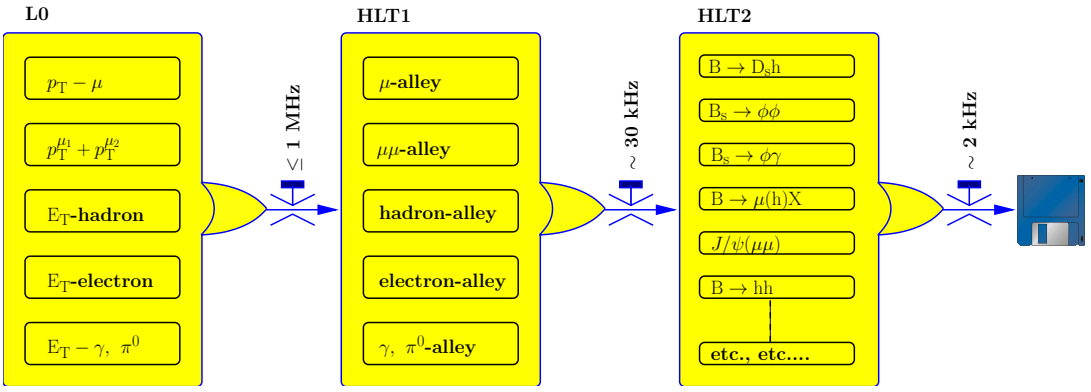

FIGURE 2.14: A flow diagram of the trigger sequences

The L0 hardware trigger functions at 40 MHz, the LHC clock frequency, with a designed output rate of 1 MHz. The L0 trigger primarily uses high energy leptons, hadrons and photons by performing a fast reconstruction of clusters in the calorimeters; it also triggers on high p_T events in the muon chambers. This information is combined with the pile-up counter and events with a high number of primary vertices are vetoed. An overview of the L0 trigger showing the number of channels from each sub-detector received every 50 ns can be seen in Figure 2.15 [7].

The pile-up counter is a dedicated part of the VELO which identifies bunch crossings which resulted in more than one proton-proton collision. The L0 trigger decides whether an event is kept and if so the relevant data is passed to the HLT.

The majority of the L0 output (90%) is events with a single high p_T muon, electron or hadron. The p_T threshold of the L0 can be adjusted according to physics needs. The remaining 10% of the output rate is reserved for events with high p_T photons.

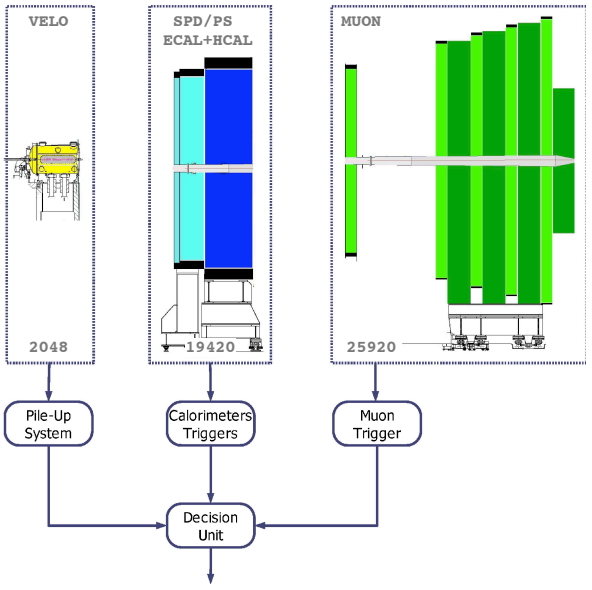

FIGURE 2.15: Overview of the L0 trigger

The events that pass the L0 trigger are passed to the HLT which further reduces the 1 MHz rate to 2 kHz by making use of the full event data. The HLT runs on a filter farm and is a series of C++ algorithms tailored to the LHCb analyses. The HLT is divided in two levels, HLT1 and HLT2. The HLT1 uses a generic algorithm to refine the L0 trigger candidates and divide them into independent alleys, where each alley corresponds to one trigger line. The alley selection first confirms the L0 trigger by reconstructing the candidate tracks in the VELO or the T-stations. The HLT1 requires candidate tracks to have high p_T or large impact parameters. This requirement alone reduces the rate to ~ 30 kHz.

After the rate has been significantly reduced the HLT2 applies inclusive and exclusive selections to the events. The HLT2 processes few enough events that an online reconstruction is performed, which allows HLT2 to use even-selection criteria similar to those used in offline analysis. The nominal final output rate of the trigger is 2 kHz.

During 2011 data taking a topological trigger was used as part of the HLT2. The Topological trigger is designed to select hadronic B decays by exploiting common properties of B-decays. It is designed as an inclusive trigger and hence does not require

every daughter particle in an event to pass the selection criteria for an event to be selected. The topological trigger looks for track combinations in a wide mass window which allows signal events to be accepted despite missing tracks. This means that the topological trigger achieves a high efficiency for any B decay with at least two charged daughters. For 2011 running the HLT2 used the topological trigger and had an output rate of 3 kHz[18].

Figure 2.16[19] shows the structure of the LHCb trigger used for 2011 data taking.

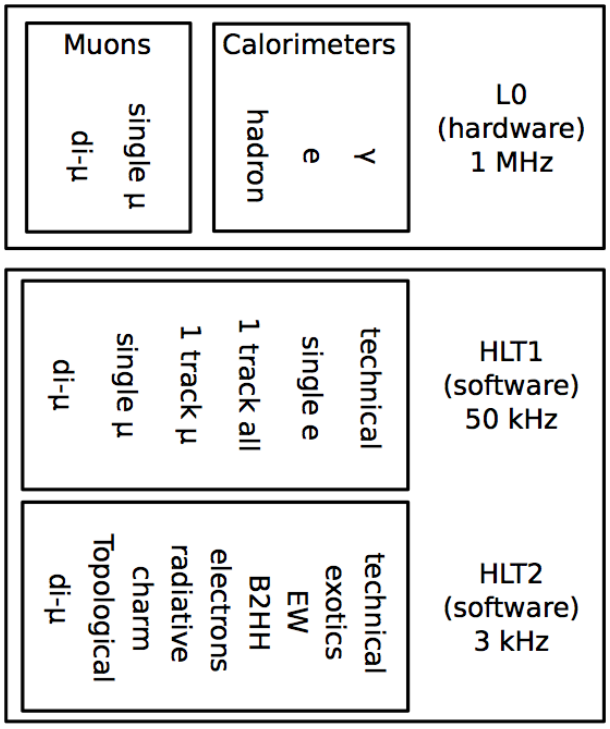

FIGURE 2.16: Overview of the 2011 LHCb trigger structure including the topological trigger.

The LHCb computing model does not allow all recorded events to be made available for physics analysis. After an initial reconstruction of all events, an event selection step stripping is executed. This is an analysis job that selects events based on selections provided by the physics groups. Only events passing one or more of these selections are made available for further analysis.

2.5 LHCb Computing

Gaudi is the framework underlying the LHCb software [20]. The LHCb software is managed using a series of packages and projects by the Apache Subversion revision control system (SVN). Each step of the LHCb analysis chain is handled by a separate project. The key projects are summarised here [21].

- **Gauss**: Gauss governs the generation of MC events and their interactions with the detector. The proton-proton collisions are simulated with PYTHIA [8] and the decays of B-mesons are handled by EvtGen [22]. Gauss then simulates the events using GEANT 4 [23].
- **Boole**: This software follows on from Gauss, and digitises the Gauss simulation output to emulate particles.
- **Moore**: Moore is responsible for all aspects of the trigger.
- **Brunel**: Brunel performs the reconstruction of particles, both from MC and data events. Charged particle tracks and energy deposits in the calorimeters are used in the reconstruction.
- **DaVinci**: DaVinci is the LHCb physics analysis software. Fully reconstructed tracks and energy clusters are input from Brunel. Python based configurables are used to reconstruct specified decays and to save outputs for further offline analysis.

Chapter 3

Theoretical Motivation

The Standard Model encapsulates our knowledge of particle physics. The model describes the physics of subatomic particles and has withstood considerable experimental scrutiny as well as accurately predicting the existence and properties of the Z and W bosons. Nevertheless there are aspects of the Standard Model that remain relatively poorly constrained by experiment.

It was understood by Sakharov that, under the Big Bang model of the universe, there are three essential elements that allow the excess of baryons over anti-baryons to accrue. These are [24]:

1. reactions that change baryon number have to occur;
2. there must be **CP** violation; and
3. they must proceed outside thermal equilibrium

therefore CP violation is an essential requirement of baryogenesis, and importantly, an area open to experimental exploration. Although the Standard Model does allow for CP violation, the amount allowed by the model is not sufficient to account for the baryon-anti-baryon asymmetry we observe in the universe today. LHCb is purpose built

to probe CP violation in the B system, and it is possible that LHCb will observe CP violation in the decays of B mesons which is incompatible with the Standard Model.

This thesis concentrates upon a decay width measurement from a decay channel which will help to constrain the fundamental parameter Γ_s, the average decay width between the two eigenstates of the B_s^0 meson. Γ_s is a quantity that LHCb will be capable of measuring to high precision. A measurement of Γ_s will help to constrain $\Delta\Gamma_s$, the decay width difference between the heavy (B_H) and light (B_L) eigenstates, which has the potential of deviating from the Standard Model prediction and giving us insight into new physics. This chapter will give an overview of the theory of B_s^0 meson lifetimes and mixing.

3.1 Charge, Parity and Time Symmetries

In particle physics the relevant discrete symmetries are:

- **C - Charge conjugation**: Transforming a particle into its antiparticle, i.e. this changes the sign of all additive quantum numbers.
- **P - Parity**: The reflection of space co-ordinates, i.e **r** into $-\mathbf{r}$.
- **CP**: The combined transformation of Charge and Parity.
- **T - Time reversal**: Reverses the direction of motion by changing the time cordinate t into $-t$.

The majority of decays are invariant under **C**, **P**, or **T** transformations, however weak interactions violate both **C** and **P** symmetry. **CP** was thought to be conserved until its violation was observed in the neutral kaon system and then subsequently in the B system.

Invariance under the combined symmetry **CPT** is a requirement of all relativistic field theories, and is constrained to $< 10^{-18}$ from measurements of the $K^0 - \bar{K}^0$ mass difference.

3.2 The Longevity of B_s^0 Mesons

The B_s^0 meson is produced at the LHCb in one of two flavours:

$$B_s^0 = (\bar{b}, s),\ \bar{B_s^0} = (b, \bar{s}) \tag{3.1}$$

B_s^0 mesons live for a long time in relation to other heavy particles. The lifetime of the particle can be found by using the concept of tracking time from space, i.e. by locating the particle's decay vertex and measuring the spatial separation (L) from its production point, this is illustrated in Figure 3.1. The proper lifetime (τ) of the particle

$$\tau = \frac{m_B}{p} L \tag{3.2}$$

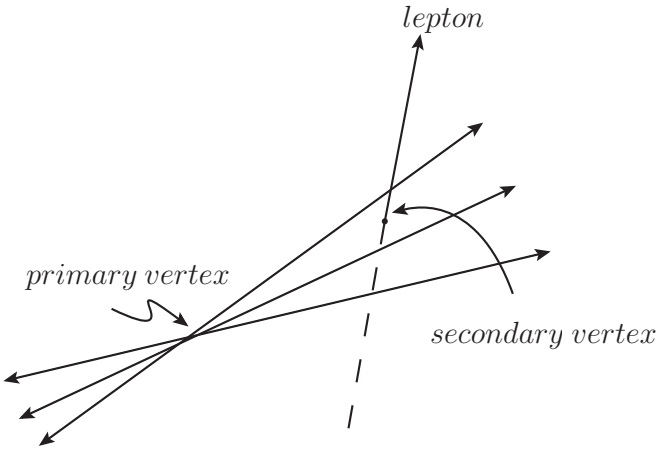

FIGURE 3.1: A B hadron is created at the primary vertex, it travels to the secondary vertex where it decays. The lifetime can be deduced by measuring the distance between the vertices.

B_s^0 mesons are unstable particles and decay to other particles through the weak interaction. The lifetime of a particle is determined by the sum of all the different interaction processes that can occur to various final states [25].

3.2.1 The Spectator Model

If we look just at the decay of the b quark, shown in Figure 3.2, we can see that the decay is analogous to that of the μ decay shown in Figure 3.3. In fact, we can go as far as to scale the expression for the μ width, Γ_μ, to find a naive approximation for the width of the b quark [26].

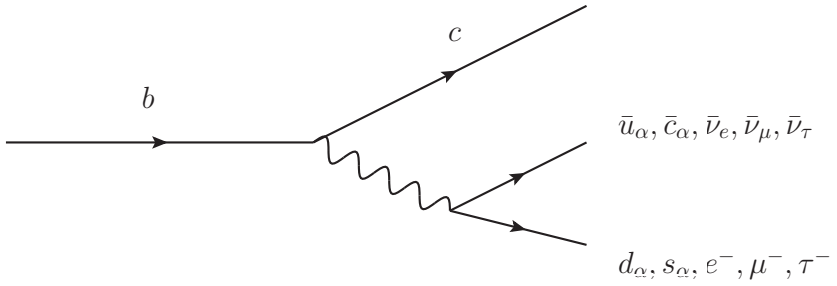

FIGURE 3.2: Feynman digram showing the b quark decay. If the final state quark masses are neglected there will be an equal contribution from each decay. There are 9 channels as quarks come in three colours.

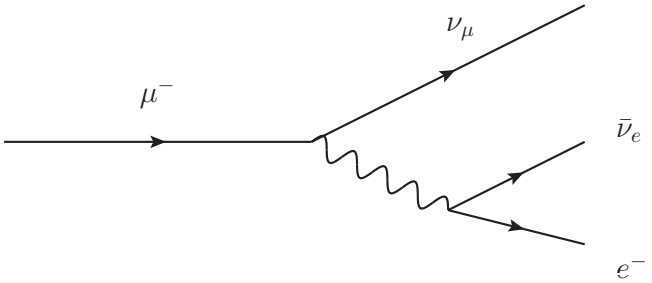

FIGURE 3.3: Feynman digram showing the μ decay.

The muon width has been analytically calculated and for the first order process is given in equation 3.3

$$\Gamma_\mu = \frac{G_F^2}{192\pi^3} m_\mu^5 \tag{3.3}$$

where m_μ is the mass of the muon and G_F is the Fermi point coupling given by:

$$G_F = \frac{\sqrt{2}}{8} \frac{g^2}{m_W^2} \tag{3.4}$$

where, g is the weak interaction coupling constant and m_W is the mass of the W boson. The value of G_F has been determined by muon lifetime experiments to be $1.166 \times 10^{-5}\,\mathrm{GeV}^{-2}$ [27].

The b quark width can be estimated simply by adapting equation 3.3 by accounting for the following difference:

- The muon mass is replaced with that of the bottom quark mass.
- A factor of $|V_{cb}|^2$ arises as there is a difference in coupling between the bottom and charm quarks and between the muon and neutrino.
- The phase space for the bottom quark decay is 9 times larger than that of the muon decay.
  - The muon is the lightest unstable particle and can only decay into an electron and neutrinos, however in the bottom quark decay W can decay to any of the three lepton generations and the two quark generations ud' and cs'.
  - Due to possible colour changes the phase space for quarks is multiplied by a factor of three.

Taking these adaptations into account the b quark decay width can be postulated and is shown in equation 3.5.

$$\Gamma_b = \frac{G_F^2}{192\pi^3} m_b^5 |V_{cb}|^2 \times (2 \times 3 + 3) \tag{3.5}$$

Using equations 3.3 and 3.5 we are able to predict the lifetime of the b quark in terms of the muon lifetime, this is given by equation 3.6:

$$\tau_b = \tau_\mu \left\{ \frac{m_\mu}{m_b} \right\}^5 \frac{1}{9|V_{cb}|^2} \tag{3.6}$$

The muon lifetime has been measured to be $2.2\,\mu$s. By using this lifetime as well as: $m_\mu = 0.106\,\text{GeV}$, $m_b = 4.2\,\text{GeV}$ and $|V_{cb}| = (41.6 \pm 0.7) \times 10^{-3}$ [28] the lifetime of a B mesons species is estimated between 1.3 and 1.6 ps, which is of the order of the observed B meson lifetimes.

This model gives all the B meson species the same lifetime, as in these calculations the lifetime only depends on the bottom quark mass. Although this gives us an estimation of the lifetime we know that the B species have distinct lifetimes, this indicates that the light quarks cannot be ignored.

3.2.2 Pauli Interference

It is possible to get an indication how the light quarks contribute to the lifetime phenomenology via a comparison between the B^- and B_s^0 mesons. The light quarks serve to give the B^- meson a longer lifetime in comparison to B_s^0, this effect is due to Pauli Interference between the possible decays. The B^- has two decay paths to the same final state as shown in Figure 3.4. The two diagrams interfere with each other destructively and this leads to a shortening of the decay width for the B^- meson [25].

Conversely, as seen in Figure 3.5, there are two unique final states and so no interference occurs, which accounts for a widening of the decay width in comparison to the B^- system. This argument can also be used to expect the B^0 lifetime to be shorter than that of the B^-, as the B^0 system also decays to two different final states. This logic gives us the hierarchy shown below.

$$\tau_{B^-} > \tau_{B^0}, \tau_{B_s^0} \tag{3.7}$$

We now have an approximation of the lifetimes of the B meson species, as well as a hierarchy between them. The measurements of the absolute lifetime of the B_s^0 will be discussed in Chapter 4.

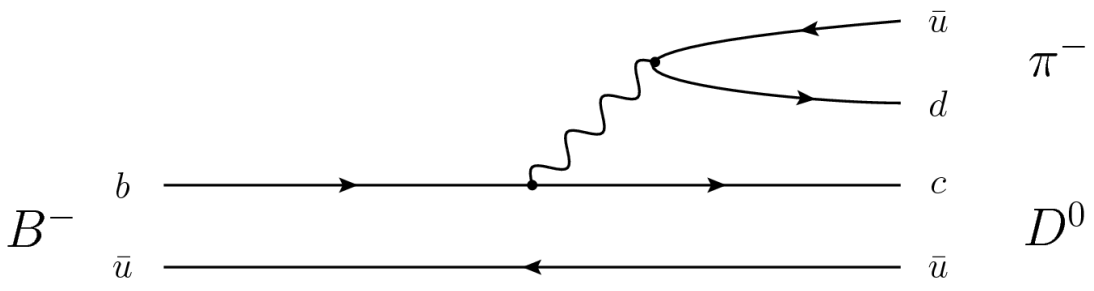

B^- decay via an external emission of a W boson.

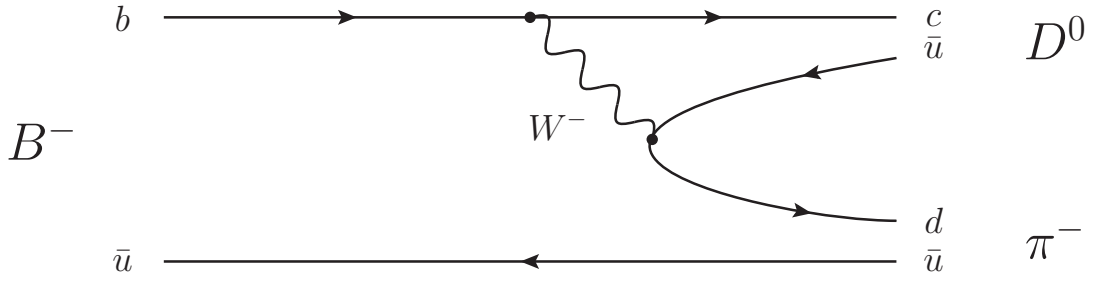

B^- decay via an internal emission of a W boson.

FIGURE 3.4: B^- decay via an external (top) and internal (bottom) emission of a W boson. The two diagrams show the B^- decays to the same final state. This causes the decays to interfere destructively. As a result the decay width $\Delta\Gamma_{B^+}$ is reduced.

3.3 B_s^0 Meson Mixing

Mixing refers to the process by which a neutral meson changes into its anti-meson (and vice-versa) as it propagates. This process is known to occur for K^0, D^0, B_d^0 and, of particular interest to us, B_s^0. The ARGUS experiment was able to observe the phenomena of $B^0 - \bar{B^0}$ mixing in 1987. CDF first observed $B_s^0 - \bar{B_s^0}$ mixing in 2006 [29].

Figure 3.6 illustrates $B_s^0 - \bar{B_s^0}$ mixing at the quark level; the process occurs via second order weak interactions as the b and s quarks mix as allowed via the CKM matrix.

Mixing in the $B_s^0 \bar{B}_s^0$ system is a consequence of the mass eigenstates not being identical to the flavour eigenstates. We can describe the superposition of the flavour eigenstates

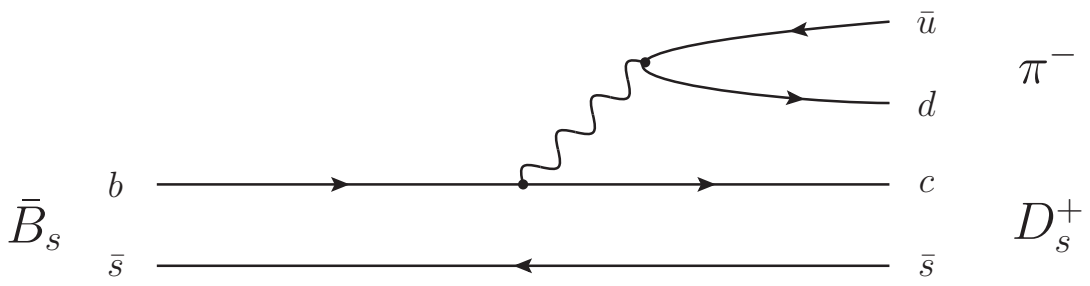

B_s^0 decay via an external emission of a W boson.

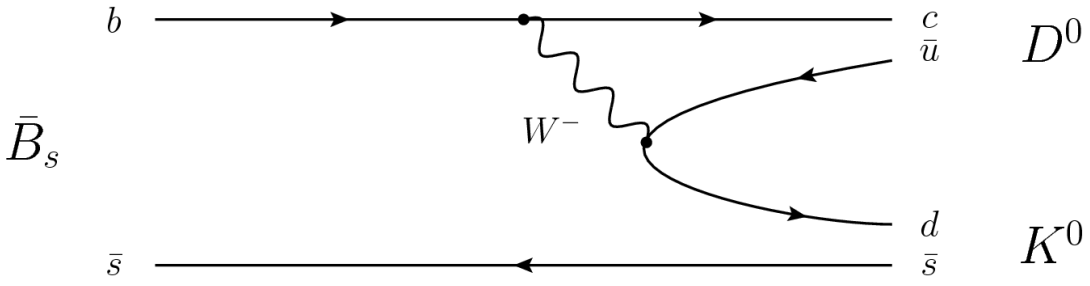

B_s^0 decay via an internal emission of a W boson.

FIGURE 3.5: B_s^0 decay via an external (top) and internal (bottom) emission of a W boson. The two diagrams show the B_s^0 decays to different final states. Hence there is no interference between the two diagrams. $\Delta\Gamma_{B_s^0} > \Delta\Gamma_{B^+}$.

in the $B_s^0\bar{B}_s^0$ system via a time dependent Schrödinger equation [30]:

$$i\hbar\frac{d}{dt}\begin{pmatrix}\alpha\\ \beta\end{pmatrix} = \mathbf{H}\begin{pmatrix}\alpha\\ \beta\end{pmatrix} \tag{3.8}$$

where the eigenvector solutions are p and q. $\mathbf{H}$ is non-hermitian as the system can decay into non $B_s^0\bar{B}_s^0$ particles. An effective Hamiltonian, $\mathbf{H}$ can be expressed in terms of hermitian matrices $\mathbf{M}$ and $\mathbf{\Gamma}$

$$\mathbf{H} = \mathbf{M} - \frac{i}{2}\mathbf{\Gamma} \tag{3.9}$$

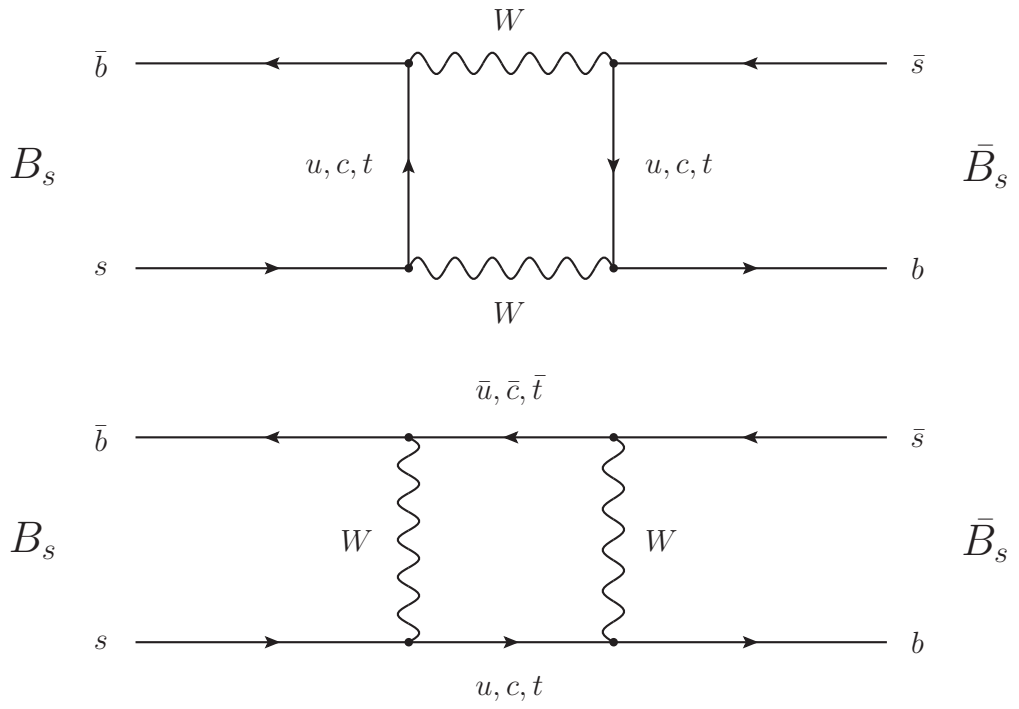

FIGURE 3.6: Box diagrams for $B_s^0 \bar{B}_s^0$ transitions.

where matrix $\mathbf{M}$ describes the mass (energy) of the system and $\frac{i}{2}\mathbf{\Gamma}$, the decay matrix, describes the decay to non-B_s^0 states; both the mass and the decay matrices are hermitian.

We can infer a lot about the $B_s^0 \bar{B}_s^0$ system based on characteristics of the matrix elements. **CPT** invariance requires that:

$$\langle B_s^0 | \mathbf{H} | B_s^0 \rangle = \langle \bar{B}_s^0 | \mathbf{H} | \bar{B}_s^0 \rangle \tag{3.10}$$

hence, if $h_{11} \neq h_{22}$ **CPT** would be violated. **H** can be expressed as:

$$\mathbf{H} = \begin{pmatrix} h_{11} & h_{12} \\ h_{12}^* & h_{11} \end{pmatrix} = \begin{pmatrix} M_{11} - \frac{1}{2}i\Gamma_{11} & M_{12} - \frac{1}{2}i\Gamma_{12} \\ M_{12}^* - \frac{1}{2}i\Gamma_{12}^* & M_{11} - \frac{1}{2}i\Gamma_{11} \end{pmatrix} \tag{3.11}$$

The eigenvectors of **H** give two physical meson states with well defined mass and decay widths. The mass eigenstates are linear combinations of the particle and anti-particle states given by equation 3.12, and the sign convention is chosen to maintain a positive mass difference.

$$|B_H\rangle = p|B_s^0\rangle - q|\bar{B_s^0}\rangle \tag{3.12}$$

$$|B_L\rangle = p|B_s^0\rangle + q|\bar{B_s^0}\rangle \tag{3.13}$$

Subscripts 'H' and 'L' stand for heavy and light physical states, with mass $M_{H,L}$ and width $\Gamma_{H,L}$. In the absence of **CP** violations $p = q = \frac{1}{\sqrt{2}}$ the mass eigenstates can further be defined as:

$$|B_H\rangle = \frac{1}{\sqrt{2}}(|B_s^0\rangle - |\bar{B}_s^0\rangle) \tag{3.14}$$

$$|B_L\rangle = \frac{1}{\sqrt{2}}(|B_s^0\rangle + |\bar{B}_s^0\rangle) \tag{3.15}$$

B_H and B_L have physical lifetimes and propagate as:

$$|B_H(t)\rangle = e^{-im_H t - \frac{1}{2}\Gamma_H t}|B_H(0)\rangle \tag{3.16}$$

$$|B_L(t)\rangle = e^{-im_L t - \frac{1}{2}\Gamma_L t}|B_L(0)\rangle \tag{3.17}$$

These physical states have a mass difference given by:

$$\Delta m_s = m_H - m_L > 0 \tag{3.18}$$

and a difference in decay width:

$$\Delta\Gamma_s = \Gamma_L - \Gamma_H \tag{3.19}$$

The average decay width of the B_s^0 meson is given by:

$$\Gamma_s = \frac{1}{2}(\Gamma_L + \Gamma_H) \tag{3.20}$$

It is useful to define the following phase, η [31]:

$$\eta = \arg(\frac{-M_{12}}{\Gamma_{12}}) \tag{3.21}$$

The mass and width difference in the B_s^0 system are related to M_{ij} and Γ_{ij} by:

$$(\Delta m)^2 - \frac{1}{2}(\Delta\Gamma)^2 = 4|M_{12}|^2 - |\Gamma_{12}|^2 \tag{3.22}$$

$$\Delta m \Delta\Gamma = 4\mathcal{R}e(M_{12}\Gamma_{12}^*)\cos\eta \tag{3.23}$$

To a good approximation this gives:

$$\Delta m = 2|M_{12}| \tag{3.24}$$

and:

$$\Delta\Gamma = 2|\Gamma_{12}|\cos\eta \tag{3.25}$$

Both η and Γ_{12} are physical and their values can be calculated from the SM. This results in a theoretical prediction of $\Delta\Gamma$ [32]:

$$\Delta\Gamma_{SM} = 0.087 \pm 0.021\,\text{ps}^{-1} \tag{3.26}$$

3.4 Time Dependent Decay Rates of Untagged B_s^0 Mesons

This analysis is performed on untagged B_s^0 mesons, therefore it is insensitive to the flavour of the particle. The decay rate for untagged mesons to final state f can be written as[1]:

$$\Gamma(f,t) = \Gamma(B_s^0(t) \to f) + \Gamma(\bar{B}_s^0(t) \to \bar{f}) \tag{3.27}$$

This analysis deals with flavour specific decays, meaning that final state f is only accessible to the B_s^0 and the final state $\bar{f}$ is only accessible to the $\bar{B}_s^0$. We will still however see a contribution from each term in equation 3.27 as the $B_s^0(t)$ and $\bar{B}_s^0(t)$ oscillate as a function of time. This leads to the time dependent decay rate for untagged flavour-specific decays described by equation 3.28, where $\mathcal{N}_f$ is a time-independent normalisation factor calculated to be 0.25 [33].

$$\Gamma(t) = \mathcal{N}_f e^{-\Gamma_s t} \cosh \frac{\Delta\Gamma}{2} t \tag{3.28}$$

Substituting in for the mass eigenstates we obtain the key equation for this thesis:

$$\Gamma(t) = \mathcal{N}_f (e^{-\Gamma_L t} + e^{-\Gamma_H t}) \tag{3.29}$$

[1] No production asymmetry for B_s^0 mesons at LHCb is expected

Chapter 4

Lifetime Measurements in HEP

This chapter will cover the experimental history of Γ_s measurements, including: the fitting theory to the channel; experimental aspects of a lifetime measurement; and current measurements of this parameter.

4.1 Lifetime Measurement Theory

Particles have a constant decay probability which leads to an exponential lifetime distribution. The B_H and B_L mesons have slightly different lifetimes, as discussed in section 3.3. Every decay $B_s^0 \to f$ is therefore a sum of two exponentials with a decay rate given by [34]:

$$R(t) \propto A_H e^{-\Gamma_H t} + A_L e^{-\Gamma_L t} \tag{4.1}$$

with A_H and A_L being weighting coefficients of the eigenstate contributions. Different channels are sensitive to different combinations of these lifetimes and hence have to be modelled accurately in order to obtain a measurement of Γ_s and $\Delta\Gamma_s$.

4.1.1 Flavour Specific Decays

The class of channels which includes $B_s \to D_s\pi$ are B flavour-specific final states; they allow both CP-even and CP-odd decays. The lifetime distribution is therefore the sum of two exponentials and the distribution is given by the form shown in equation 4.1 with the coefficients A_L and A_H equal [35]. Illustrations of the double exponential function are shown on both linear and logarithmic scales in Figures 4.1 and 4.2 respectively.

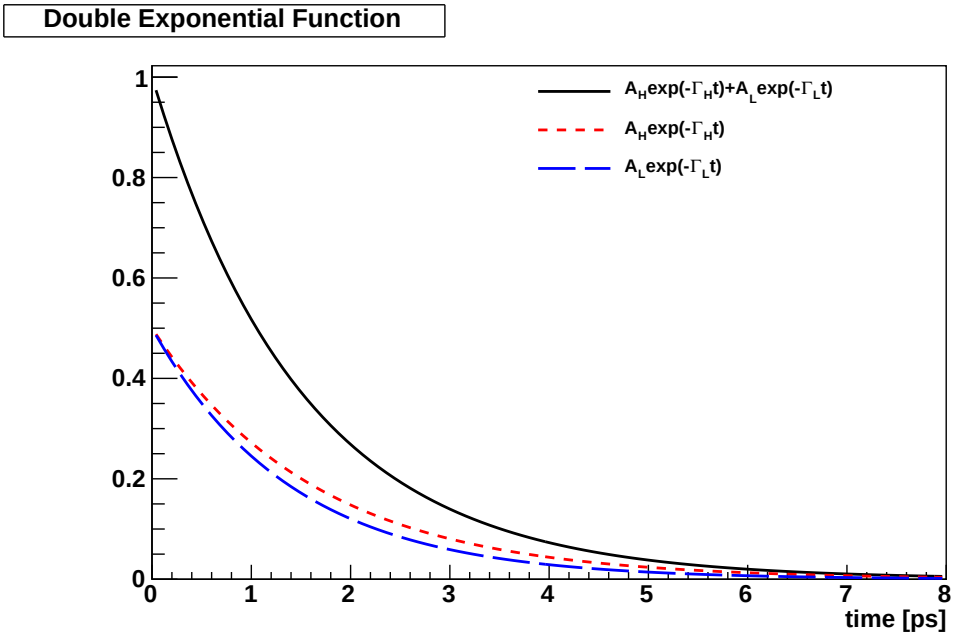

FIGURE 4.1: The lifetime distribution of flavour specific decays is represented by a double exponential, in flavour specific decays $A_H = A_L$.

Experiments traditionally fit lifetime distributions from flavour-specific decays with a single exponential in order to make a measurement of the effective lifetime. Fitting for a single exponential one obtains a measurement of the observed decay width Γ_{FS}, which is a combination of $\exp(-\Gamma_L t) + \exp(-\Gamma_H t)$. If $\Delta\Gamma$ is small it becomes hard to differentiate between the two exponentials, hence Γ_{obs} is approximately Γ_s.

Fitting a single exponential results in a fit to:

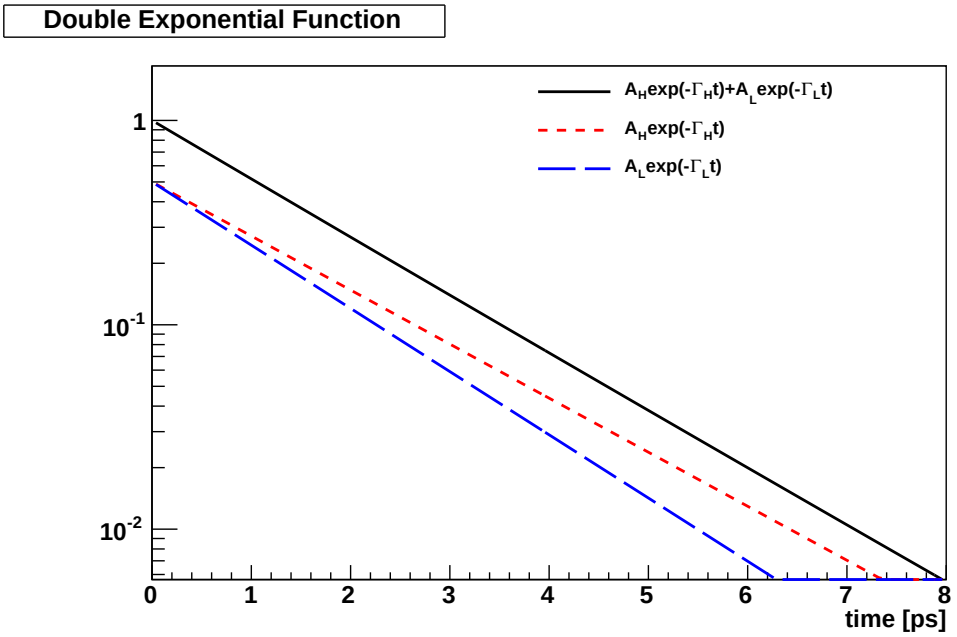

FIGURE 4.2: The lifetime distribution of flavour specific decays is represented by a double exponential on a logarithmic scale, in flavour specific decays $A_H = A_L$.

$$\frac{1}{\Gamma_{FS}} = \frac{A_H \frac{1}{\Gamma_H^2} + A_L \frac{1}{\Gamma_L^2}}{A_H \frac{1}{\Gamma_H} + A_L \frac{1}{\Gamma_L}} \tag{4.2}$$

in the flavour-specific class of channels the coefficients $A_H = A_L$ which simplifies the correction to:

$$\frac{1}{\Gamma_{FS}} = \frac{1}{\Gamma_s} \frac{1 + \left(\frac{\Delta\Gamma_s}{2\Gamma_s}\right)^2}{1 - \left(\frac{\Delta\Gamma_s}{2\Gamma_s}\right)^2} \tag{4.3}$$

for small values of $\frac{\Delta\Gamma_s}{\Gamma_s}$ this approximates to:

$$\frac{1}{\Gamma_{FS}} \approx \frac{1}{\Gamma_s}\left[1 + \left(\frac{\Delta\Gamma_s}{\Gamma_s}\right)^2\right] \tag{4.4}$$

It is evident that Γ_{FS} is related to Γ_s by a second order correction $\mathcal{O}\left(\Delta\Gamma^2/\Gamma_s^2\right)$, as shown in Equation 4.4 [36]. As $\Delta\Gamma_s$ increases the measured lifetime will also increase. This method of measuring Γ_s is valid whilst the correction is less than the statistical precision of the measurement; however if the selection efficiencies is dependent on proper-time this can lead to a bias in the fit towards Γ_L or Γ_H.

It can be seen that the correction gives a 4% effect when $\Delta\Gamma \sim 0.1ps^{-1}$ and $\Gamma \sim 0.7\,\mathrm{ps}^{-1}$. At LHCb the statistical precision exceeded this very early in the data taking and thus naive fitting to flavour specific channels will not be meaningful without dealing appropriately with $\Delta\Gamma$.

To avoid biasing the fit towards either of the mass eigenstates it is necessary to use the correct double exponential in the fit and perform a simultaneous fit to both Γ_s and $\Delta\Gamma_s$ [35], however this class of channel gives a poor constraint on $\Delta\Gamma$. A fit for both Γ_s and $\Delta\Gamma_s$ using this channel alone is not straightforward as the likelihood for $\Delta\Gamma$ is not parabolic. This phenomenology is described fully in Appendix D and is illustrated in Figure 4.3 which is obtained from toy Monte Carlo studies. Thus one cannot guarantee to obtain a useful parameter set for $[\Gamma_s, \Delta\Gamma_s]$ with its correlation matrix until the data set is very large (such that all of the fitting then takes place in an approximately parabolic valley near one or other minimum).

Naturally one can simply assert a fixed value of $\Delta\Gamma$ to extract Γ_s from Γ_{FS} but that will not be useful in subsequent simultaneous fits. This analysis primarily presents fit results for Γ_{FS} from FS $B_s^0 \to D_s\pi$ channel alone.

4.1.2 Decays to CP Eigenstates

This thesis will not present measurements of Γ_s and $\Delta\Gamma_s$ using this channel, however it will use the results from the β_s analysis note [37] to constrain the decay width fit. Here we present a simple overview of the channel.

The $B_s^0 \to J/\psi\phi$ channel involves decays to both CP even and CP odd eigenstates. The different CP eigenstates are predominantly the result of either B_H or B_L decays

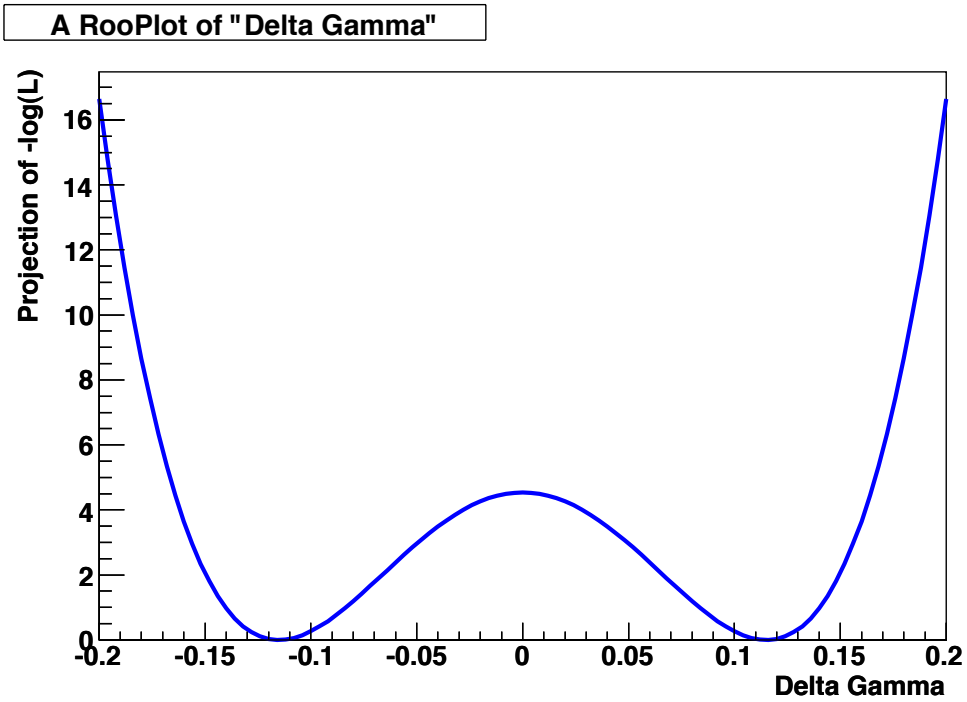

FIGURE 4.3: The negative log-likelihood scan of $\Delta\Gamma_s$ in $B_s^0 \to D_s\pi$.

and hence allows us to measure Γ_H and Γ_L independently of each other via an angular analysis.

There are three decay angles (θ, ϕ, ψ) as shown in Figure 4.4 each with analogous expressions for differential cross-section. Equation 4.5 shows the differential cross-section as a function of the single decay angle, θ_{tr}.

$$\begin{aligned}\frac{d\Gamma(t)}{d\cos\theta} \propto &(1-R_\perp)[(1+\cos\phi_s)e^{-\Gamma_L t}+(1-\cos\phi_s)e^{-\Gamma_H t}]\frac{1}{2}(1+\cos^2\theta) \\ &+\ R_\perp[(1-\cos\phi_s)e^{-\Gamma_L t}+(1+\cos\phi_s)e^{-\Gamma_H t}]\sin^2\theta\end{aligned} \tag{4.5}$$

In this expression $R_\perp$ is the fraction of CP-odd final state, expected to be ~ 0.2 in the SM. Setting $\phi_s = 0$, a good approximation in the SM ($\phi_s^{SM} = -0.036 \pm 0.002$ [38]), the equation simplifies to 4.6.

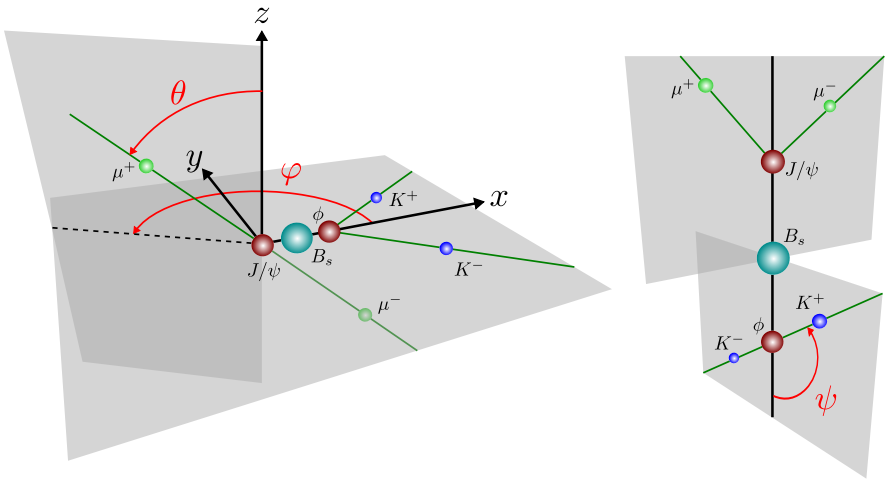

FIGURE 4.4: The $B_s^0 \to J/\psi\phi$ decay angles. In the J/ψ rest frame the angle formed between the μ^+ and the z-axis is θ and the azimuthal angle is ϕ. In the ϕ meson rest frame the polar angle ψ is defined between the K^+ and the x-axis.

$$\frac{d\Gamma(t)}{d\cos\theta_{tr}} \propto (1 - R_\perp)e^{-\Gamma_L t}(1 + \cos^2\theta_{tr}) + 2R_\perp e^{-\Gamma_H t}\sin^2\theta_{tr} \tag{4.6}$$

It is evident that the expression is the sum of two exponentials with different weights, but these can be partially separated by using the angular information. If the angular analysis gave perfect separation then this channel would yield independent measurements of Γ_H and Γ_L with no correlation. In fact the separation is not perfect and hence there remains some negative correlation.

The analogous expressions when all three decay angles (θ, ψ, ϕ) are used are significantly more complicated. The characteristics are the same and the separation of the different CP final states is naturally better as there is more information available and

hence the measurements of Γ_H and Γ_L are even less correlated.

4.1.3 Combining the Measurements

By combining the results from both the $B_s^0 \to J/\psi\phi$ and $B_s^0 \to D_s\pi$ channels an improvement on the precision of Γ_s and $\Delta\Gamma_s$ will be obtained. The improvement in the Γ_s value is simply from adding primary information which constrains both Γ and $\Delta\Gamma$ to the $B_s^0 \to J/\psi\phi$ information. The improvement seen in the precision of $\Delta\Gamma_s$ is not from additional information, rather the correlation between $\Delta\Gamma_s$ and Γ_s is reduced and hence a more precise fit is obtained.

The channels are combined by applying a χ^2 constraint to a fit for Γ_s and $\Delta\Gamma_s$ in $B_s^0 \to D_s\pi$ data. The constraint is based on the current LHCb measurements and correlation of $\Delta\Gamma_s$ and Γ_s from channel $B_s^0 \to J/\psi\phi$.

4.2 Lifetime Measurements Experimentally

The aim of lifetime fitting techniques in HEP is to model and correct for effects that distort the measured lifetime from its expected exponential shape. Many things can distort the measured lifetime, for example at detector level a change in geometry acceptance as a function of lifetime, however this is more relevant for fixed target experiments that study lifetimes of long lived particles that travel a much greater distance before decaying.

During the event selection other effects can distort the lifetime at trigger level and due to off-line reconstruction of the decay. A common way to distinguish heavy meson decays from other events is to apply an impact parameter (IP) cut. The impact parameter is the shortest distance between a track and a primary vertex (PV).

Both B_s^0 and D_s mesons have lifetimes of the order 1 ps, this means the IP of the tracks produced from the final state daughter particles are non-zero. The cut requires

a minimum distance between the final state tracks and the primary vertex, and so cuts away the majority of the prompt background, however it also rejects true signal events that decay at small lifetimes. This cut directly leads to a bias on the lifetime distribution at low lifetimes. This is known as a proper-time acceptance and can drastically distort the basic exponential distribution of the lifetime. Correcting for this bias is the main difficulty in making lifetime measurements from hadronic decays and will be further discussed in 5.4.

4.3 Edinburgh Lifetime Fitter

LHCb measures momenta, masses, and decay lengths of particles. From these quantities we are able to reconstruct observables such as the decay time and the decay angles of the particles. Our physics model describes, by way of a Probability Density Function (PDF), how these observables should behave. The PDF however depends upon unknown physics parameters, and these are what we hope to measure.

RapidFit is a fitting tool developed by the Edinburgh LHCb group. It is written in C++ and aims to use common code so that it can be maintained and developed by everyone in the group. RapidFit is designed to work out-of-the-box; the user only need add the relevant PDFs to the software. RapidFit fitter performs negative log-likelihood minimisation using Minuit or Minuit2 [39] and both numerical and analytical integrations of the specified PDFs.

A simple XML (Extensible Markup Language) configuration file is used to set up data generation or predefined data sets, and fitting. The software makes a clear distinction between observables and physics parameters and allows constraints to be placed on the physics parameters in the fit. The user builds their desired fitting model from combinations (sums or products) of PDFs. Once the PDF has been defined no additional coding is necessary to run a fit, and no recompilation is required if changes are made to the configuration XML file.

The XML requires that the physics parameters used by the relevant PDFs be initialised with an input value and boundary limits if the parameter is to be floated. The XML enables you to specify a PDF and datafile that you want to fit to; or to specify PDFs for fitting and generation, where the PDFs used can be the same or different. A fit parameter space is then defined that controls which discrete or continuous observables are of interest as well as their range of validity. Once the fit is performed it can then be validated by plotting the fitted PDF on to the input dataset.

As stated, the physics model for fitting can be built up of several PDF components; the example below shows one such model used by this analysis. It can be seen that the mass and lifetime descriptors of each component are initially combined by taking their product (ProdPDF), then each component is combined by use of a normalised sum (NormalisedSumPDF) with a fraction weight between the PDFs. Only two PDFs can be included by a normalised sum PDF which leads to the nested nature of the definitions.

```
<NormalisedSumPDF>
<FractionName>SignalFraction</FractionName>
        <ProdPDF>
                <PDF>
                        <Name> B_s^0 mass PDF</Name>
                </PDF>
                <PDF>
                        <Name>Bs2DsPi lifetime PDF</Name>
                </PDF>
        </ProdPDF>
        <NormalisedSumPDF>
        <FractionName>CombinatoricFraction</FractionName>
                <ProdPDF>
                        <PDF>
                                <Name>Combinatoric bkg mass PDF</Name>
                        </PDF>
                        <PDF>
                                <Name>Combinatoric bkg lifetime PDF</Name>
                        </PDF>
                </ProdPDF>
                <ProdPDF>
                        <PDF>
                                <Name>Partially Reconstructed bkg mass PDF</Name>
                        </PDF>
                        <PDF>
                                <Name>Partially Reconstructed bkg lifetime PDF</Name>
                        </PDF>
                </ProdPDF>
        </NormalisedSumPDF>
</NormalisedSumPDF>
```

4.4 Current Lifetime Measurements

In order to understand the result obtained by this analysis it is necessary to look at the broader context of the measurement. The current world average results are taken from

$1/\Gamma_{FS}$	$1.417 \pm 0.042\,\text{ps}$

TABLE 4.1: Current world averages of $1/\Gamma_{FS}$.

	without constraint from $\tau(B_s \to \text{FS})$	with constraint from $\tau(B_s \to \text{FS})$
$1/\Gamma_s$	$1.515^{+0.034}_{-0.034}\,\text{ps}$	$1.472^{+0.024}_{-0.026}\,\text{ps}$
$\tau_{Short} = 1/\Gamma_L$	$1.407^{+0.035}_{-0.034}\,\text{ps}$	$1.408^{+0.033}_{-0.030}\,\text{ps}$
$\tau_{Long} = 1/\Gamma_H$	$1.642^{+0.091}_{-0.083}\,\text{ps}$	$1.543^{+0.058}_{-0.060}\,\text{ps}$
$\Delta\Gamma_s$	$0.102^{+0.043}_{-0.043}\,\text{ps}^{-1}$	$0.062^{+0.034}_{-0.037}\,\text{ps}^{-1}$

TABLE 4.2: Current world averages of Γ_{FS}, Γ_s and $\Delta\Gamma_s$ measured in various channels, results are shown both with and without a constraint from Γ_{FS}.

the Heavy Flavour Averaging Group [40] (HFAG) results prepared for the PDG2011 [28].

The current world average results of $1/\Gamma_{FS}$ is shown in Tables 4.1. This measurement is predominantly found from $B_s \to D_s \ell X$ decays.

Table 4.2 gives the world average measurements of $1/\Gamma_s$, $1/\Gamma_L$, $1/\Gamma_H$ and $\Delta\Gamma_s$ from a combined fit to CDF, D0, ALEPH and DELPHI data. $1/\Gamma_s$ is found from measurements of the $B_s^0 \to J/\psi\phi$ decay. The measured value of $1/\Gamma_{FS}$ is then used as input in order to extract the values of $1/\Gamma_L$ and $1/\Gamma_H$ which subsequently gives us $\Delta\Gamma_s$. The table shows the world average measurements both with and without taking in to consideration a constraint from a flavour-specific $1/\Gamma_{FS}$ measurement.

This analysis is particularly interested in a comparison of the value of $1/\Gamma_s$ and $1/\Gamma_{FS}$. It can be seen that $1/\Gamma_s$ is greater than $1/\Gamma_{FS}$ by a significant margin. As discussed in section 4.1.1, a flavour-specific fit to $1/\Gamma_{FS}$ is expected to yield a lower value than that of a fit to $1/\Gamma_s$. There is therefore evidence of tension between these measurements.

The results are shown graphically in Figure 4.5. The plot shows the 1σ and 2σ contours of the current measurements in the plane $(1/\Gamma_s, \Delta\Gamma_s)$; the average of all direct

measurements is shown in red, the constraint given by the $B_s \to$ flavour specific decays in blue, and their combination in black. The yellow band is a theory prediction $\Delta\Gamma_s = 0.088 \pm 0.017\,\mathrm{ps}^{-1}$ from [32].

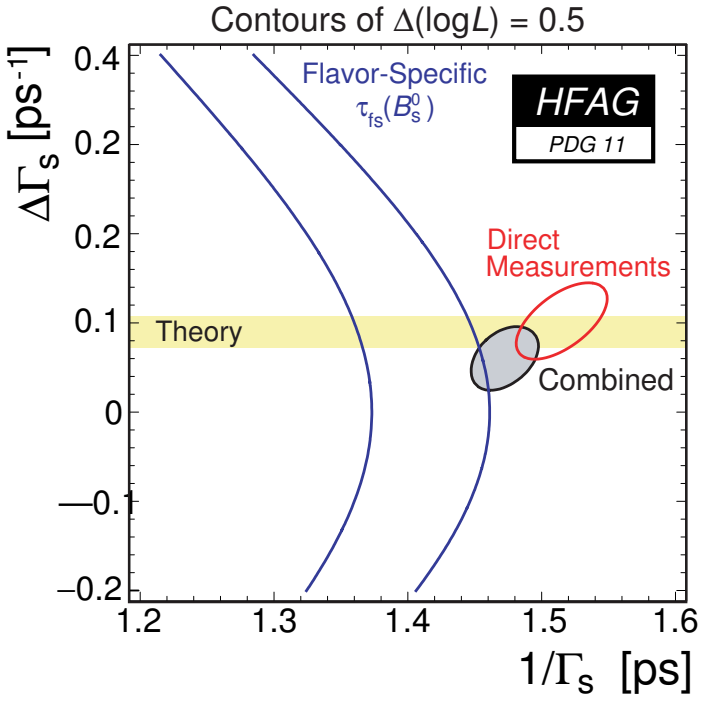

FIGURE 4.5: The current constraints in plane $(1/\Gamma_s, \Delta\Gamma_s)$ showing the average of all direct measurements (red), constraint from FS decays (blue) and their combination (black). The yellow band gives the theoretical prediction. Plot from HFAG.

The updated theory prediction of $\Delta\Gamma_s = 0.087 \pm 0.021\,\mathrm{ps}^{-1}$ is given by the paper [35].

The LHCb experiment has measured Γ_s, $\Delta\Gamma_s$ and their correlation ρ from $B_s \to J/\psi\phi$ in the β_s analysis [37]. These values will be used as constraints in this analysis.

$$\Gamma_s = 0.657 \pm 0.009 \pm 0.008\,\mathrm{ps}^{-1}$$

$$\Delta\Gamma_s = 0.123 \pm 0.029 \pm 0.011\,\mathrm{ps}^{-1}$$

$$\rho_{\Gamma_s,\Delta\Gamma_s} = -0.3$$

Taking the LHCb measurements of Γ_s and $\Delta\Gamma_s$ we can use equation 4.3 to make a prediction for $1/\Gamma_{FS} = 1.633\,\text{ps}$ of $\Gamma_{FS} = 0.646 \pm 0.009 \pm 0.008\,\text{ps}^{-1}$.

Chapter 5

The $B_S \to D_S^- \pi^+$ Decay

This chapter will introduce the $B_s \to D_s^- \pi^+$ channel used in this analysis and discuss how a clean sample is obtained from all the events that pass the LHCb trigger. This comprises the selection applied to reduce background contributions; understanding and parametrising the proper-time acceptance that is introduced at trigger level [41].

5.1 $B_s \to D_s^- \pi^+$ Decay Topology

$B_s \to D_s^- \pi^+$, Figure 5.1, is a flavour specific decay therefore the B_s flavour at the point of its decay is known from the charge of its decay products. The B_s decays to $D_s^- \pi^+$ final state, and the $\bar{B}_s$ to a $D_s^+ \pi^-$ final state.

$B_s \to D_s^- \pi^+$channel has a large branching fraction $(3.2 \pm 0.5) \times 10^{-3}$ [28] and can be cleanly reconstructed. The decay has one contributing tree diagram shown in Figure 5.2.

This channel is reconstructed using the the decay chain $B_s \to D_s^- (K^- K^+ \pi^-) \pi^+$ as this exploits the most abundant decay mode of the D_s with a combined branching fraction of $5.50 \pm 0.27\%$. This decay mode specifies the final state particles of the decay, K^-,

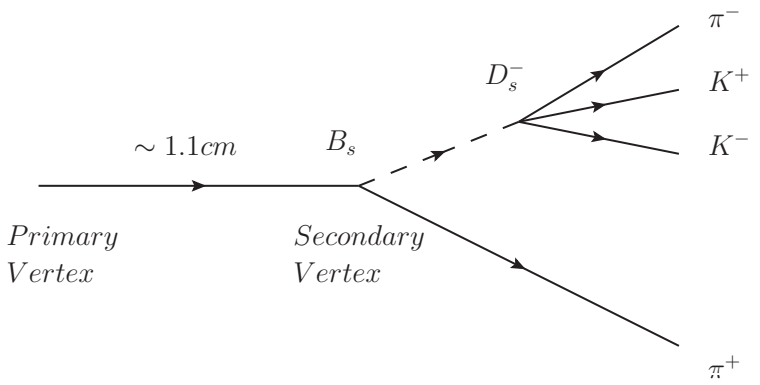

FIGURE 5.1: Illustration of the flavour specific decay $B_s \to D_s^-(K^+K^-\pi^-)\pi^+$

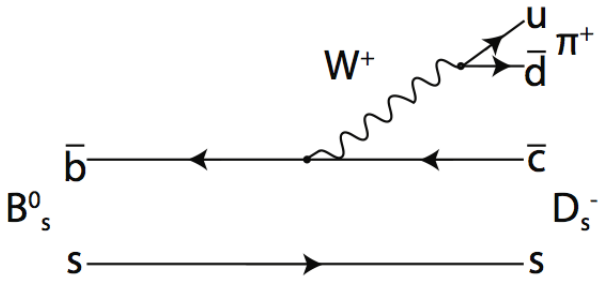

FIGURE 5.2: Feynman diagram representing the tree $B_s \to D_s^- \pi^+$ decay

K^+, π^- and π^+, however the same final state can also be obtained via a resonance. The decay descriptors for the two most prominent resonances are:

- $B_s \to D_s^-((\phi \to K^-K^+)\pi^-)\pi^+$
- $B_s \to D_s^-((K^-K^*(892)^0 \to K^+\pi^-))\pi^+$

5.2 $B_s \to D_s^- \pi^+$ Signal Selection

The $B_s \to D_s^- \pi^+$ selection used in this analysis is described in this section. The selections were generated and optimised by the flavour physics working group, and do

not constitute my own work [1]. This section will initially define the types of variable that provide good signal-background separation for this channel, and then present the values of the cuts used, followed by histograms of the selection applied to 2011 data.

5.2.1 Variable Discriminating Power

The cuts used in the selection are defined below, the more complex of which are expanded on in the relevant subsections. The 'bachelor' refers to the pion decaying directly from the B_s and is distinct from the daughters of the D_s.

- **DLL(A - B) separation:** used to distinguish between particles of type A and B. The Delta Log Likelihood (DLL) cut is the difference in the log-likelihoods of the RICH reconstructions of a track under different particle hypotheses. This is expanded upon in section 5.2.2.
- **Momentum (P):** Final state particles from B-decays typically have a higher momentum than those from prompt and non B-decays.
- **Transverse momentum (P_T):** Final state particles from B-decays typically have a higher transverse momentum than those from prompt and non B-decays. The bachelor has a high transverse momentum relative to the daughter pions and kaons of the D_s.
- **Impact Parameter:** The perpendicular distance between the track and the vertex is defined as the impact parameter. This is illustrated in two dimensions in Figure 5.3.
- **Impact Parameter χ^2:** The daughters of the B_s and D_s arise from displaced vertices, hence they are expected to have high impact parameter significances with respect to the primary vertex.
- **Vertex χ^2:** A measure of how precisely tracks can be fitted to a common vertex. The χ^2 requirement is illustrated in figure 5.4.

[1] The selection is also used by the LHCb Δm_s analysis [42]

- B_s **and** D_s **Mass Window:** An invariant mass window requirement rejects unwanted events when the mass of the reconstructed particle is well known.

- **Cut on the** B_s **direction (**$cos(\theta)$**):** This cuts on the cosine of the angle between the momentum of the particle and the direction of flight from the best PV to the decay vertex. For a well reconstructed particle the momentum should lie on line connecting the particle's PV and decay vertex.

- **Cut on the Distance Of Closest Approach (DOCA):** This cuts on the distance of closest approach between all possible pairs of particles.

- **Absolute ID (ABSID):** This cuts on the absolute value of PID, i.e. specifying $ABSID = \pi^+$ will select both positive and negative pions.

- **cos(DIRA):** The cosine of the angle between the momentum of the particle, and the direction of flight vector from the best PV to the decay vertex.

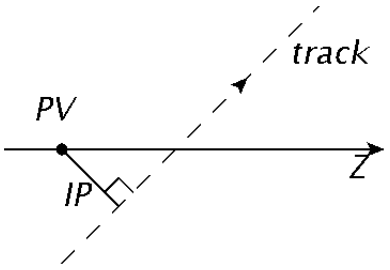

FIGURE 5.3: The Impact Parameter is a 3D distance projected here on to 2D.

5.2.2 Particle Identification

At the first stage of event selection, after the tracks have been reconstructed, information from each relevant sub-detector is used to assign the track with a PID. The relevant sub-detectors are the RICH systems which distinguish charged pions, kaons and protons; the calorimeters which assign electrons, photons, hadron tags; and the muon chambers. It is possible for each track to be assigned several PIDs. The PID

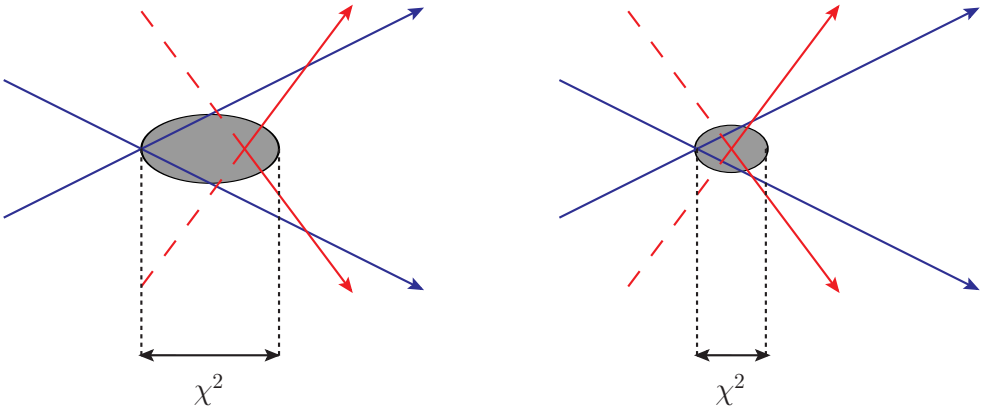

A loose vertex χ^2 requirement A tight vertex χ^2 requirement

FIGURE 5.4: An illustration of the Vertex χ^2 requirement. The red and the blue tracks should originate from the same vertex, a tight vertex χ^2 requirement constrains this.

information from each sub-detector is then consolidated to output a likelihood probability that the track is an electron (e), a muon (μ) or a hadron (h), examples of the outputs of the sub-detectors are given in equations 5.1 5.2 and 5.3 respectively.

$$\mathcal{L}(e) = \mathcal{L}_{RICH}(e)\mathcal{L}_{CALO}(e)\mathcal{L}_{MUON}(non\mu) \tag{5.1}$$

$$\mathcal{L}(\mu) = \mathcal{L}_{RICH}(\mu)\mathcal{L}_{CALO}(\mu)\mathcal{L}_{MUON}(\mu) \tag{5.2}$$

$$\mathcal{L}(h) = \mathcal{L}_{RICH}(h)\mathcal{L}_{CALO}(h)\mathcal{L}_{MUON}(non\mu) \tag{5.3}$$

LHCb then uses this PID to assign four likelihood hypotheses to each track, these are $\Delta \ln \mathcal{L}_{e\pi}$, $\Delta \ln \mathcal{L}_{\mu\pi}$, $\Delta \ln \mathcal{L}_{K\pi}$ and $\Delta \ln \mathcal{L}_{p\pi}$ where all tracks are initially classed as pions. These likelihoods can then be combined and analysed by calculating the delta log-likelihood (DLL) between two hypotheses, as shown in equation 5.4:

$$DLL(A-B) = \Delta \ln \mathcal{L}_{AB} = \ln \mathcal{L}(A) - \ln \mathcal{L}(B) = \ln \left[\frac{\mathcal{L}(A)}{\mathcal{L}(B)} \right] \tag{5.4}$$

The function tends to have positive values for correctly identified 'A' particles and negative values for correctly identified 'B' particles. A simple inequality cut based on the DLL between two particles imposes a requirement on the PID of that particle.

Figure 5.5 shows a PID performance plot [43] for $\Delta \ln \mathcal{L}(K-\pi) > 5(\Delta \ln \mathcal{L}(K-\pi))$, we can compare the kaon identification rate and the pion mis-identification rate along the momentum spectra.

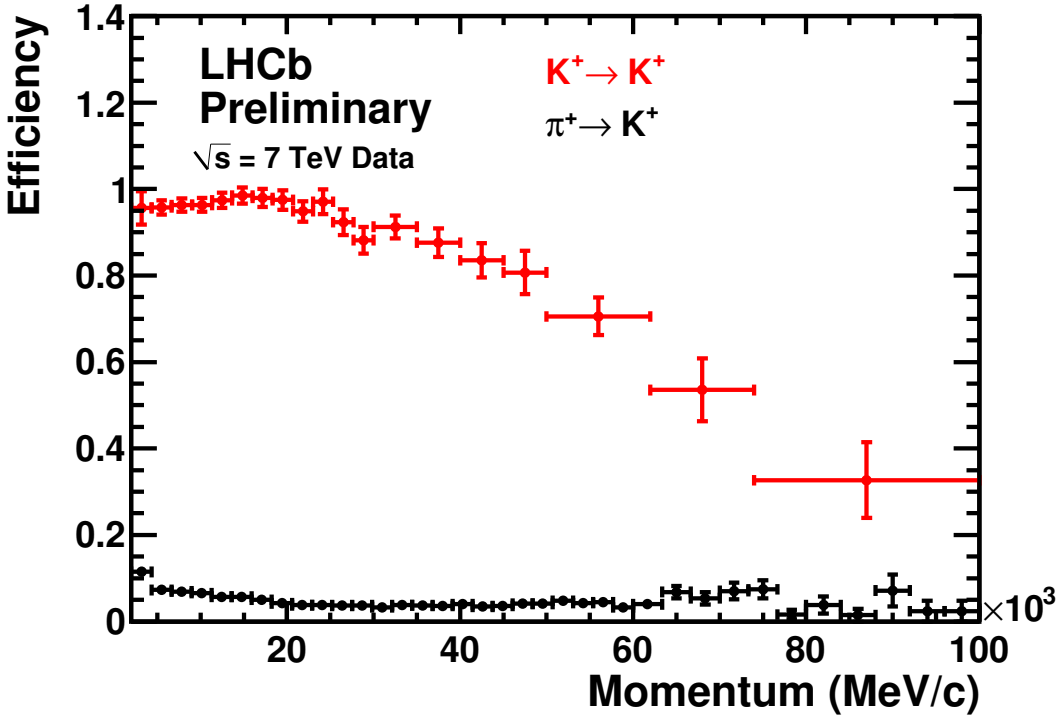

FIGURE 5.5: RICH PID performance measured on data as a function of track momentum. The PID requirement is $\Delta \ln \mathcal{L}(K-\pi) > 5$, kaon identification is shown in red, pion mis-identification is shown in black.

5.2.3 The Selection

The data selection process first applies a set of loose cuts from the initial stripping selection. The stripping line selects $B \to DX$ and $B_s \to D_s X$ decays, with the D or D_s decaying to three hadrons. These cuts are given in Table 5.1. This stripping line does not distinguish between the B meson flavour and selects events with π^+ or K^+ bachelors.

After stripping the offline selection is then applied. The initial set of cuts on $B_s \to D_s^- \pi^+$ events are given in table 5.2. These cuts are applied to the entire data set and do not impose requirements on intermediate states. However, due the the multiple contributing signal channels for the D_s decay the data are then divided into two exclusive groups, decays via a ϕ resonance (SelA) and decays via a $K^*(892)$ (SelB). Only the decays via a resonance are used in this analysis as they provide a far cleaner signal than the non-resonant decay to K^-, K^+, π^- and π^+ final states. The SelA cuts are given in Table 5.3 and the SelB cuts in Table 5.4.

Dividing the signal in this way allows us to make use of the extra constraint of a resonance to discriminate against the background in each channel; the backgrounds will be modelled independently for each signal selection.

5.2.4 The Selection Applied to Data

The full selections were applied to the 2011 LHCb data and the B_s^0 mass distributions for the data passing each selection are shown in Figures 5.6 and 5.7.

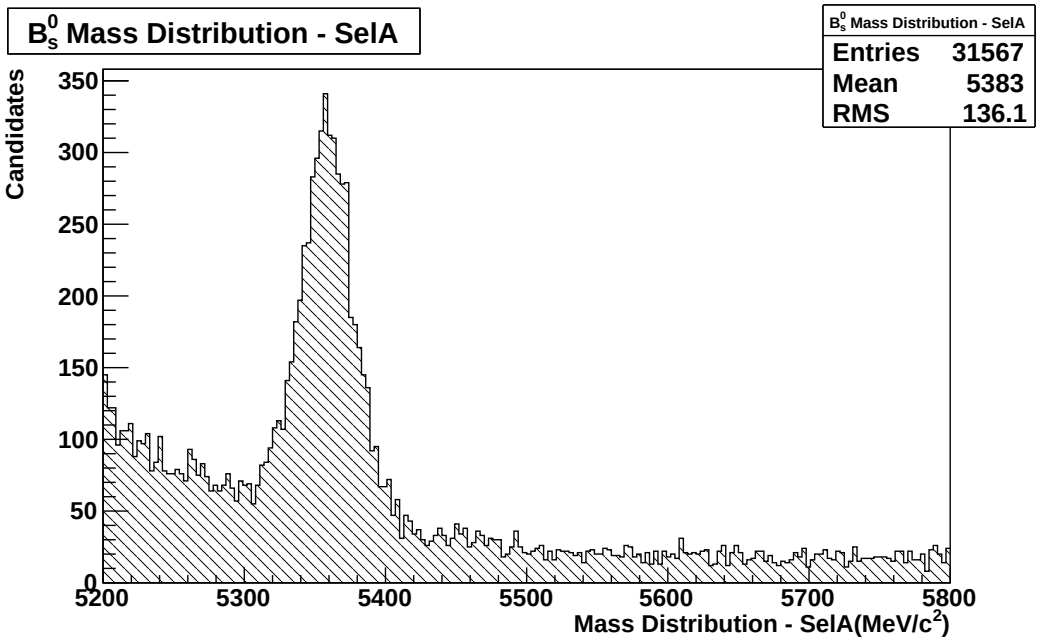

FIGURE 5.6: 2011 $B_s \to D_s^- \pi^+$ signal selection via a ϕ resonance (SelA)

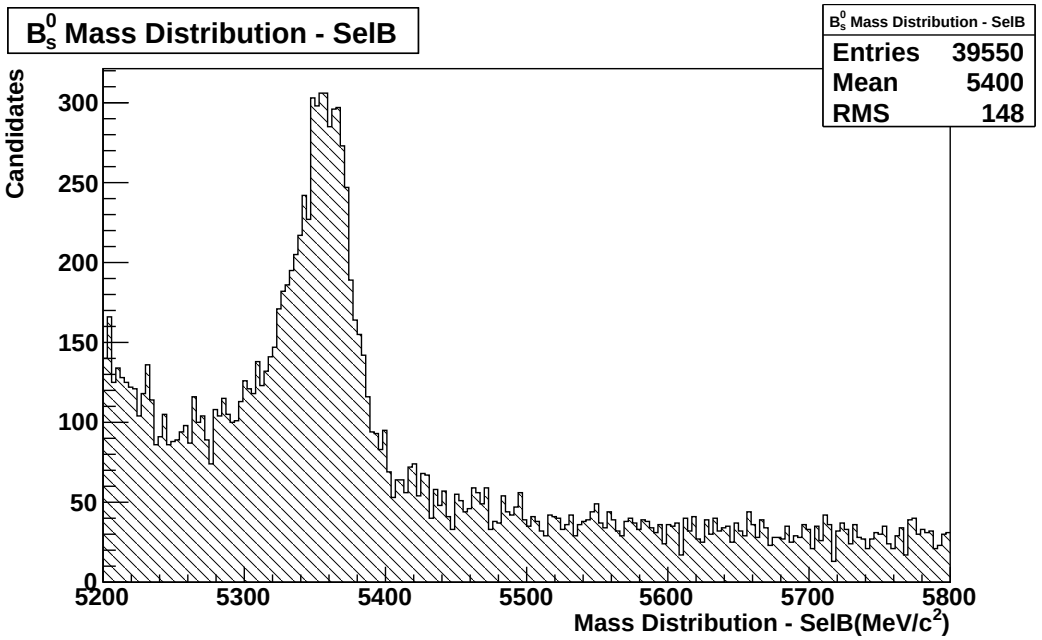

FIGURE 5.7: 2011 $B_s \to D_s^- \pi^+$ signal selection via a $K^*(890)$ (SelB)

Cuts on the B_s candidate	
Mass('B_s')	$< 500\,\mathrm{MeV/c^2}$
Best PV IP χ^2	< 250
Best PV Lifetime	< -1000
Best PV Direction Angle	> -1
Vertex χ^2	< 12
Cuts on the D_s^- candidate	
p_T	$> 1500\,\mathrm{MeV/c}$
Mass('D_s^+')	$< 110\,\mathrm{MeV/c^2}$
Max DOCA	$< 1.5\,\mathrm{mm}$
Absolute ID	='K^+' OR 'π^+'
Min IP χ^2 (to PV)	> 40
Vertex χ^2	< 12
Best PV IP χ^2	> 0
Best PV Direction Angle	> 0.9
Cuts on the D_s^- Daughters	
Track χ^2/DOF	< 5
p_T	$> 250\,\mathrm{MeV/c}$
p	$> 2000\,\mathrm{MeV/c}$
Min IP χ^2 (to PV)	> 4
Cuts on the bachelor π^+	
Track χ^2/DOF	< 5
p_T	$> 500\,\mathrm{MeV/c}$
p	$> 5000\,\mathrm{MeV/c}$
Min IP χ^2 (to PV)	> 16

TABLE 5.1: The stripping line B2DXWithDhhh used in event selection. In addition to the above cuts the selection vetoes events with more than 180 tracks.

Cuts on the B_s candidate	
P	$> 2GeV/c$
IP χ^2	< 16
cosDIRA	> 0.9999
primary vertex separation significance	> 64
Cuts on the D_s^- candidate	
P_t	$> 2GeV/c$
primary vertex separation significance	> 100
$\lvert m(D_s^-) - m(D_s^-)_{PDG} \rvert$	$< 30MeV/c^2$
Cuts on the D_s^- daughters	
P_t	$> 300MeV/c$
min(IP χ^2)	> 9
DLL(K-π) for kaons	> -10
DLL(K-π) for pion	< 10
Cuts on the bachelor π^+	
DLL(K-π)	< 5
*ABSID	='π^+'

TABLE 5.2: The base set of cuts that are applied in this analysis to select $B_s \to D_s \pi$ events. *This cut has been added for this analysis to discriminate against decays $B_s^0 \to D_s^- K^+$.

$D_s \to \phi(K^+K^-)\pi^+$ Cuts	
$\lvert m(\phi) - m(\phi)_{PDG} \rvert$	$< 30MeV/c^2$

TABLE 5.3: SelA: The additional cuts that are applied in this analysis to select $B_s \to D_s \pi$ events.

$D_s \to K^*(892)^0(\pi^+K^-)K^+$ Cuts	
$\lvert m(K^*) - m(K^*)_{PDG} \rvert$	$< 30MeV/c^2$
DLL(K-π) for *discriminating kaon	> 0
DLL(K-p) for *discriminating kaon	> -10

TABLE 5.4: SelB: The additional cuts that are applied in this analysis to select $B_s \to D_s \pi$ events, with $D_s \to K^*(892)^0(\pi^+K^-)K^+$. *The discriminating kaon refers to the particular kaon of the same sign as its parent D_s.

5.3 Backgrounds

It is important to understand the background contribution to the selected events before fitting for signal. Figures 5.6 and 5.7 given in section 5.2.4 show the mass distribution of selected events from 2011 data. It is evident that there are background contributions that need to be understood and modelled before an accurate fit can be made to this data.

The background contributions can be split into three categories:

- **Partially reconstructed backgrounds:** This background is due to D_s decays to the final state particles $K^+K^-\pi^-$, but the B_s decay included additional final state particles that have not been reconstructed. The badly reconstructed B_s mesons from these background channels have a lower mass than a true B_s^0 due to the missing particle(s), and hence this background will only appear in the lower side-band of the B_s mass peak.
- **mis-ID backgrounds:** These arise from a final state particle being mis-identified, for example a pion being mis-identified and reconstructed as a kaon. This is arguably the most dangerous background as it often results in a peaking background underneath the signal peak.
- **Combinatoric backgrounds:** These are due to random combinations of tracks that pass the selection criteria but did not originate from the same mother particle. It is expected that this will be the only contributing background to the upper B_s mass side-band.

The three types of backgrounds can be studied using different MC data sets, which will be identified in the following sections. It is important to understand that the two signal selections will have different background rejection efficiencies. The fraction of the background as well as its lifetime and mass distributions will be modelled separately for each selection. However initially the contributing background channels must be identified.

5.3.1 Partially Reconstructed Backgrounds

This class of background are studied by MC data generated for decays $B_s \to D_s(^*)X$; $D_s(^*)$ is an excited state of the D_s; X represents any hadronic system. The B_s mass distribution obtained from the base cuts is shown in Figure 5.8, where the MC truth matched signal has been removed from the sample to allow the background to be studied. It can be seen that the partially reconstructed backgrounds only contribute to the lower B_s^0 mass side-band; in such a decay there is always at least one particle missing which tends to lower the measured mass of the B_s^0.

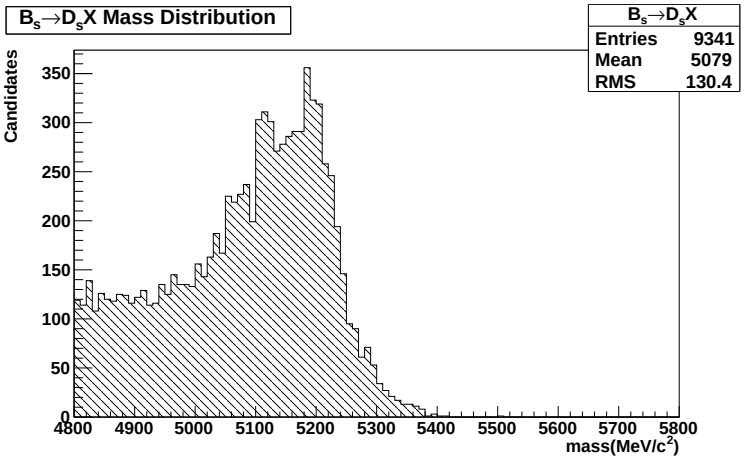

FIGURE 5.8: The mass distribution of $B_s \to D_s^- X$ background events.

By using the MC truth information of the generated events a picture of the contributing decays can be constructed. Looking at the reconstructed D_s in the selection, a substantial contribution of these can be seen to originate from D_s^*. Figure 5.9 slows the D_s MC parents ID's. The two contributing peaks are at ± 433 and ± 531; these ID codes refer to D_s^* and B_s respectively [2]. It can be seen that 42% of the D_s in this sample truly came from a B_s, and 52% of the D_s's originate from a D_s^* [3]. Hence $B_s \to D_s^{-*}(D_s^-\gamma)\pi^+$ is the most prominent background contribution from the D_s branch of the decay.

[2]The codes used are the pythia generation codes and can be found in reference [1]. 0 represents a prompt particle with no mother; the sign on the codes indicates the particles flavour.

[3]The additional 6% of D_s's result from a wide variety of decays; the full table can be seen in Appendix A.

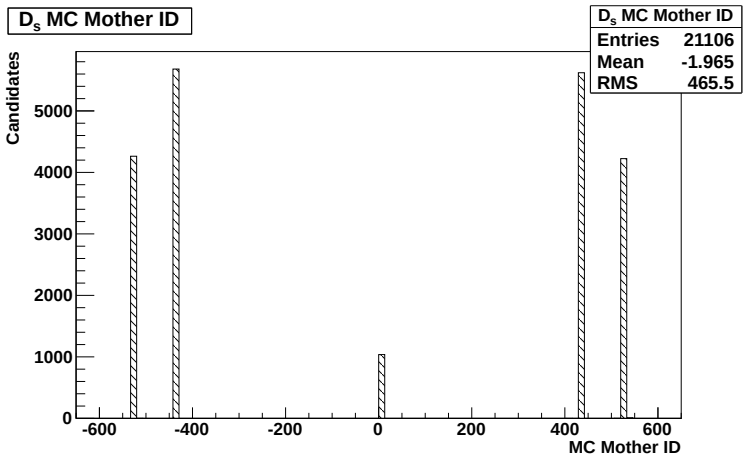

FIGURE 5.9: The MC parents to the D_s's selected from $B_s \to D_s^- X$ background events passing the base selection.

Parent	Percentage Contribution
ρ^0	$1.8 \pm 0.1\%$
$\rho^\pm$	$49.5 \pm 0.4\%$
B_s	$45.9 \pm 0.4\%$

TABLE 5.5: Parents of the bachelor; for full table see appendix.

Figure 5.10 slows the bachelor pion's MC parent's IDs. The most prominent peaks can be seen at 113 and ± 213 and ± 531; these ID codes refer to ρ^0, $\rho^\pm$ and B_s respectively. Table 5.5 gives the percentages of each bachelor's mother particle, as well as showing the origin and percentage of the parent particle. It is evident that the decay $B_s \to D_s^- \rho^+(\pi^+\pi^0)$ is also a prominent background in this sample.

The main decays that have been identified to contribute to the background are:

- $B_s \to D_s^{-*}(D_s^-\gamma)\pi^+$; in this decay the D_s^{-*} emits a photon which is then missed by the reconstruction.
- $B_s \to D_s^- \rho^+(\pi^+\pi^0)$; the π^0 is missed by the reconstruction in this scenario.
- $B_s \to D_s^{-*}(D_s^-\gamma)\rho^+(\pi^+\pi^0)$ also contributes to the background.

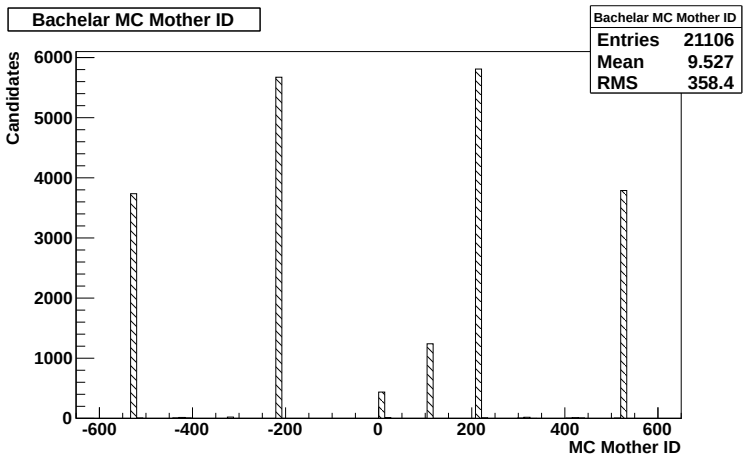

FIGURE 5.10: The MC parents to the bachelor pion selected from $B_s \to D_s^- X$ background events passing the base selection.

5.3.2 Backgrounds Arising from Mis-identified Particles

Mis-ID backgrounds can be determined from knowledge of decays with similar kinematics. The channels that are likely to contribute to this background are:

- $B_d \to D^-(K^-\pi^+\pi^-)\pi^+$ with the D meson daughter π^+ being identified as K^+, and therefore faking the $K^+K^-\pi^-$ signal.
- $\bar{\Lambda_b} \to \Lambda_c^-(\bar{p}K^+\pi^-)\pi^+$ in which the $\bar{p}$ is identified incorrectly as a K^-

The mass distributions of these backgrounds passing the base selection are shown in figures 5.11 and 5.12. The events are reconstructed with one fake K to match the signal PID. These histograms are not normalised and so can only be used to infer the shape and the mean of the resulting distributions. The quantitative contribution from each will vary after the full selections have been applied. It is evident that both of these channels have a mass distribution under that of the signal $B_s \to D_s^- \pi^+$ and contributions will have to be modelled and understood.

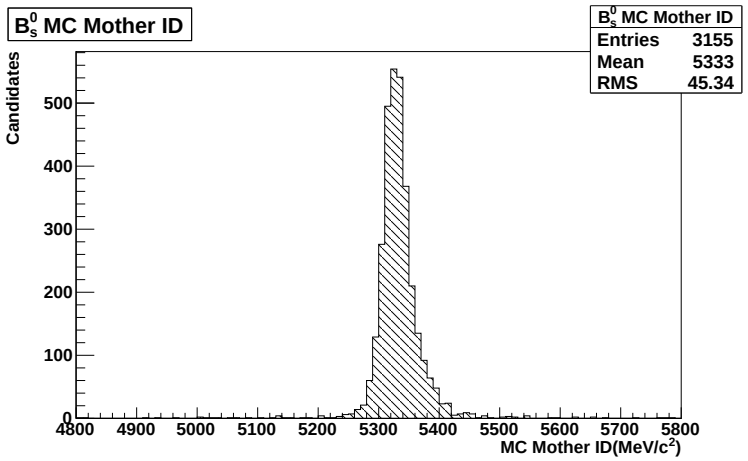

FIGURE 5.11: The mass distribution of $B_d \to D^-(K^-\pi^+\pi^-)\pi^+$ MC10 events passing the base cuts.

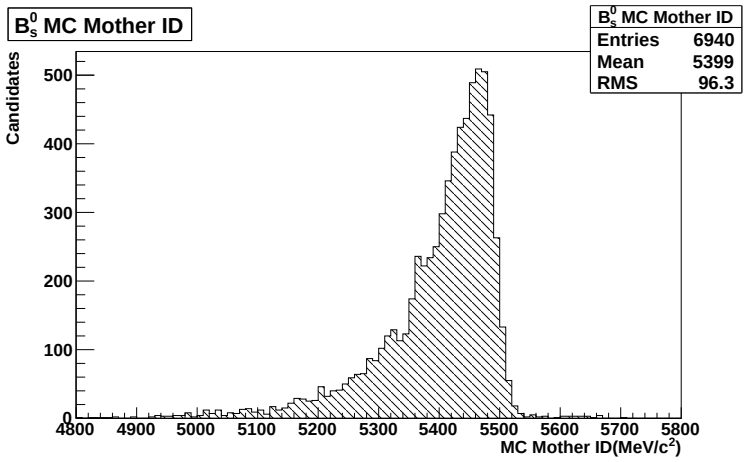

FIGURE 5.12: The mass distribution of $\bar{\Lambda}_b \to \Lambda_c^-(\bar{p}K^+\pi^-)\pi^+$ MC10 events passing the base cuts.

5.3.3 Combinatoric Background

Combinatoric backgrounds will be fitted directly from the data. Neither partially reconstructed or mis-ID background has a distribution in the B_s^0 mass upper side-band (with the exception of the shoulder of the $\bar{\Lambda}_b \to \Lambda_c^-(\bar{p}K^+\pi^-)\pi^+$). This makes it suitable to use the upper side-band to fit a single exponential to model the combinatoric background.

5.4 Detector Effects

The proper-time distribution of untagged B_s mesons measured at LHCb will not be as given by equation 3.29 due to detector effects. The distribution we measure is shown in equation 5.5

$$\Gamma(t) = \mathcal{N}_f(e^{-\Gamma_L t} + e^{-\Gamma_H t}) \times \Theta(t) \times \epsilon(t) \otimes R(t) \tag{5.5}$$

where $\Theta(t)$ is 0 if $t < 0$ and 1 if $t \geq 0$; $\epsilon(t)$ is a proper-time acceptance function and $R(t)$ is a proper-time resolution function that smears the proper-time.

5.4.1 How IP Cuts Bias Proper-Time

Trigger cuts on the impact parameter have the effect of biasing the proper-time distribution of the particle. This correlation is not directly obvious, but has to be understood for any lifetime measurements. The correlation is explained in figures 5.13, 5.14 and 5.15. The figures show a simple two-body decay with displaced secondary vertex as it is shifted along the z-axis, the daughter tracks are extended backwards and the perpendicular lines show the IP distance. If the reconstructed track intersects the solid region of the IP line it shows that the track will pass the cut, whereas if it intercepts with the dashed track it indicates that the track will not pass the cut. Figure 5.15 shows both daughters passing the IP cut; in this scenario the original particle is the longest lived so travels the furthest until its decay.

It can be seen that B_s mesons of a shorter lifetime do not pass the IP cut, whereas the longer B_s lifetimes always pass the cut. The bias is known as proper-time acceptance and is parametrised in the following section.

It is hard to reliably correct for this bias at trigger level as the reconstruction is limited by the computing time available and the selection is preliminary. The rejected events are not stored and so there is no way to find the bias by a comparison of the sample

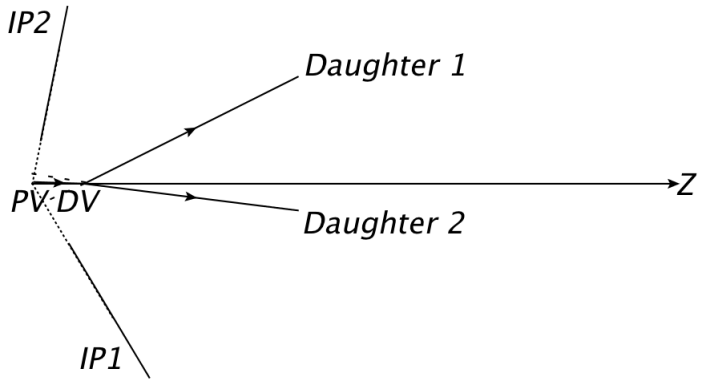

FIGURE 5.13: A two-body decay with displaced secondary vertex; neither daughter particle passes the IP cuts and the event is rejected.

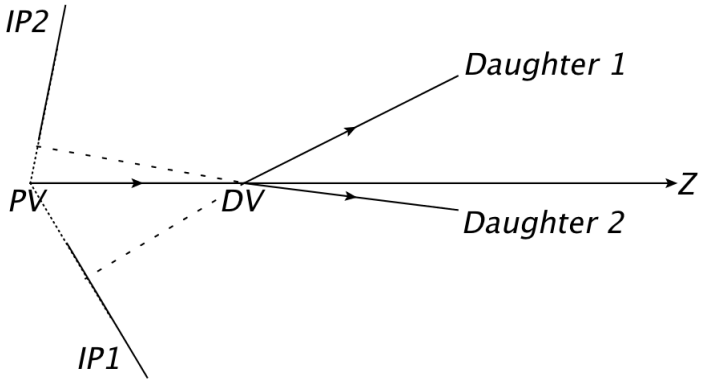

FIGURE 5.14: A two-body decay with displaced secondary vertex; one daughter particle passes the IP cuts and the event is rejected.

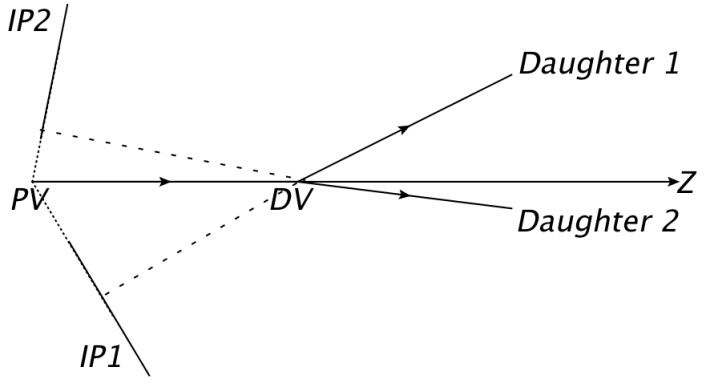

FIGURE 5.15: A two-body decay with displaced secondary vertex; both daughter particles pass the IP cuts and the event is accepted.

before and after the trigger. Lifetime biasing cuts introduced after the selection can be reliably corrected via a direct comparison between the before and after data samples.

In general there are two possible ways to correct for the proper-time acceptance. One is to determine a acceptance function from MC simulations, the alternative is to use an event-by-event acceptance function [44] without making use of MC data. This body of work will only use MC simulations to model the proper-time acceptance.

5.4.2 Proper-Time Acceptance in $B_s \to D_s \pi$

The proper-time acceptance on $B_s \to D_s \pi$ decays at LHCb is due to a minimum IP cut on decays passing the trigger which causes low proper-times to be biased. An upper proper-time acceptance bias is also observed in the MC data. This is due to the event reconstruction efficiency decreasing linearly with proper-time [45] as the LHCb tracking software is tuned around the proton-proton interaction point and tracking resolution deteriorates out from this point [41].

The proper-time acceptance function used for $B_s \to D_s \pi$ is a power-law function [46] developed as an ansatz to fit the data, and used in many LHCb analyses. The form is given by equation 5.6

$$\epsilon(t) = \frac{[b(t-t_0)]^n}{1+[b(t-t_0)]^n}(1+ct)\Theta(t-t_0) \tag{5.6}$$

where t_0 is a small offset from 0; b relates to the proper-time dependence at low proper-times; c relates to the proper-time scale at high proper-times; n is the order of the power-law and influences the sharpness of the function; $\Theta(t-t_0)$ is the Heaviside step function equal to 0 when $t \leq t_0$ and 1 when $t > t_0$.

Typical parameters for acceptance are $n \to 3$, $t_0 \to 0.1\,\text{ps}$, $1\,\text{ps}^{-1} < b < 10\,\text{ps}^{-1}$ and $c \leq 0\,\text{ps}^{-1}$. The shape of the acceptance curve generated with these values ($b = 2\,\text{ps}^{-1}$, $c = 0\,\text{ps}^{-1}$) is shown in figure 5.16, and the corresponding effect it has on the proper-time distribution is shown by figures 5.17 and 5.18.

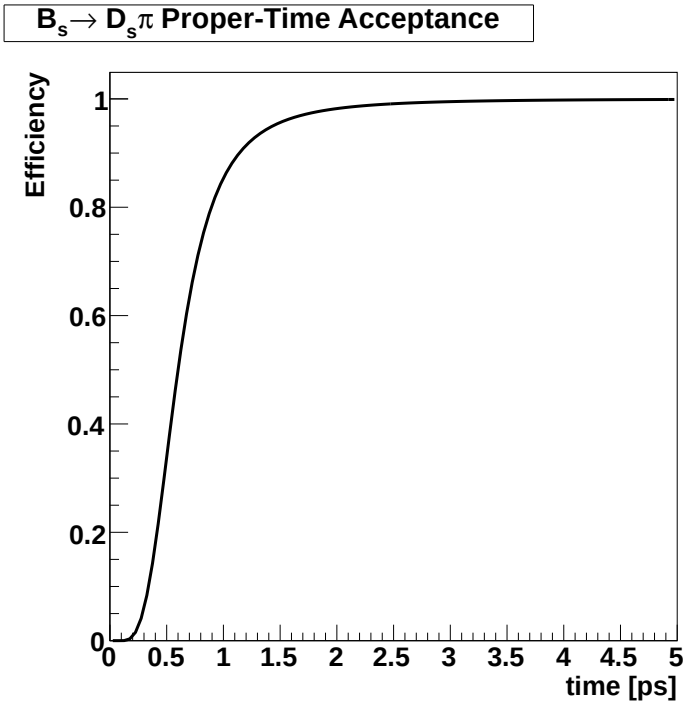

FIGURE 5.16: The form of the proper-time acceptance in $B_s \to D_s\pi$; generated with example values $b = 2\,\mathrm{ps}^{-1}$, $c = 0\,\mathrm{ps}^{-1}$, $n = 3$ and $t_0 = 0.1\,\mathrm{ps}$

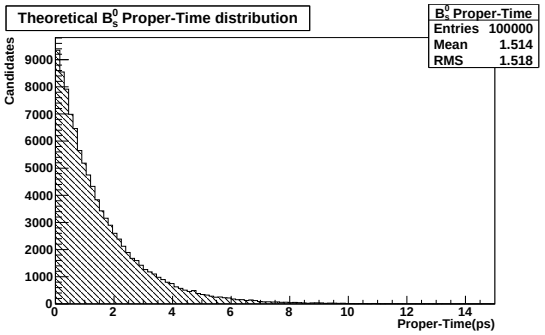

FIGURE 5.17: Example proper-time distribution before acceptance

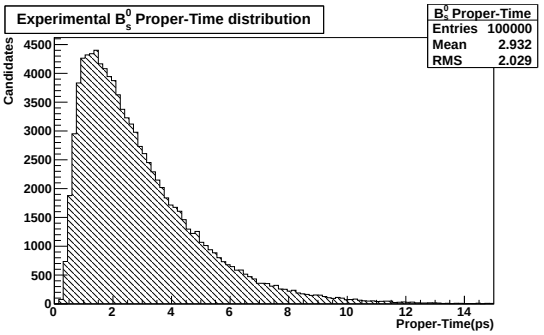

FIGURE 5.18: Example proper-time distribution after acceptance

It is evident that the acceptance function will vary for different decay kinematics passing the same IP cuts. Therefore it is expected that the signal and background samples will have different proper-time acceptance parameters.

5.4.3 Proper-time Resolution

The proper-time resolution for this channel is a single Gaussian of the order of $\sigma = 40\,\text{fs}$ which is negligible in the scale of the lifetime of the B_s^0 mesons. A systematic study can be seen in section 8.1.2 showing that the measurement of Γ_{FS} is insensitive to the LHCb proper-time resolution.

Chapter 6

Fitting to Monte Carlo Data

This chapter will look at the signal and background contributions after each selection. The fitting model is built up from several probability density functions (PDFs) that describe different contributions to the data. These PDFs have been defined by carefully studying the MC exclusive samples of the relevant decays. This section will look in detail at both the expected mass and time distributions of the relevant decays and attempt to generalise the form of the distributions for use in the fit to data.

6.1 Assessing the Size of the Background Contributions

The MC10 samples used in this analysis[1] are given in table 6.1. These are the absolute numbers of events in each sample before normalisation. The MC samples have the same trigger, stripping and selection as applied to the 2011 data.

Two different signal selections are used in this analysis, hence the background contribution will vary in each channel. Both selections are applied to MC samples for each identified background. By normalising the MC samples the relevant backgrounds for each selection can be defined. Table 6.1 lists the MC10 data sets used in this analysis.

[1]The samples were produced by the D_sH analysis working group and do not constitute my own work, I have subsequently applied SelA and SelB to the NTuples.

MC10 Sample	# events processed	# events selected (SelA)	# events selected (SelB)
Signal			
$B_s \to D_s\pi$	1622384	45302	41085
Partially Reconstructed Background			
$B_s \to D_s^- X$	unavailable	4097	4434
Miss-ID Backgrounds			
$B_d \to D^-(K^-\pi^+\pi^-)\pi^+$	475494	99	427
$\bar{\Lambda}_b \to \Lambda_c^-(\bar{p}K^+\pi^-)\pi^+$	unavailable	97	322

TABLE 6.1: MC10 datasets and event numbers used in this study.

The MC10 data sets are normalised to represent one nominal year of running at the LHCb with integrated luminosity of $2\,\text{fb}^{-1}$. This normalisation was performed directly on the signal $B_s^0 \to D_s\pi$ and the $B_d^0 \to D\pi$ samples based on the number of events processed, however this information was unfortunately not available for the other NTuples. The $B_s \to D_sX$ normalisation is trivial as the sample contains both signal and background events, so by making the $B_s \to D_sX$ signal events equal to the $B_s \to D_s\pi$ events the background is also normalised. The $\bar{\Lambda_b} \to \Lambda_c^-(\bar{p}K^+\pi^-)\pi^+$ normalisation was estimated at 70% of the B_d background based on a direct normalisation of additional MC samples generated with an older form of the trigger.

This normalisations assumes the LEP $b - \bar{b}$ hadronisation percentages [28] given in Table 6.2.

B^+	$(40.3 \pm 1.1) \times 10^{-2}$
B^0	$(40.3 \pm 1.1) \times 10^{-2}$
B_s^0	$(11 \pm 1.2) \times 10^{-2}$
$b-$Baryon	$(8.3 \pm 20) \times 10^{-2}$

TABLE 6.2: Hadronisation percentages of $b - \bar{b}$ quarks.

Figure 6.1 shows the normalised background contributions of all events passing the base cuts, before additional ϕ or K^* constraints are applied.

6.1.1 Backgrounds to SelA

Applying the SelA selection (decay propagates via a ϕ resonance) to the MC samples gives us the background distribution shown in figure 6.2.

It can be seen that by constraining the decay via the ϕ resonance the contributions from the Mis-ID backgrounds have become negligible, leaving only the low mass and combinatorics to be modelled for this fit.

In this channel the decays $B_s \to D_s^{-*}(D_s^-\gamma)\pi^+$ and $B_s \to D_s^-\rho^+(\pi^+\pi^0)$ are our main sources of background. The backgrounds are stacked on top of each other in the lower B_s^0 mass side-band. These backgrounds will be modelled together in the fit.

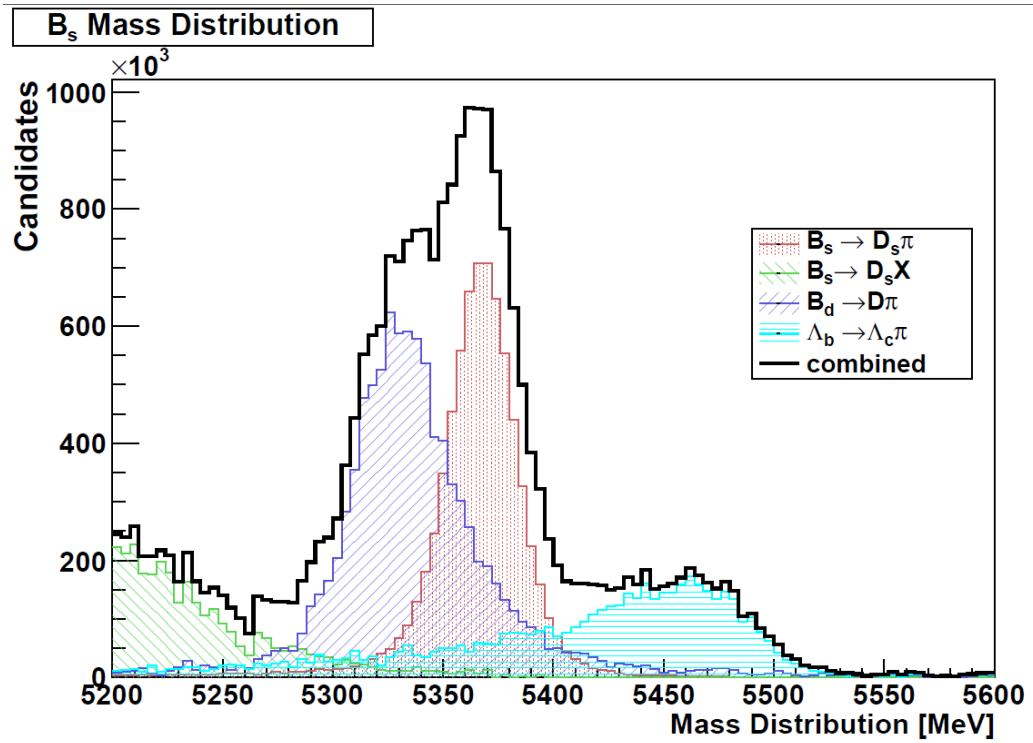

FIGURE 6.1: A normalised distribution of MC10 events passing the base cuts.

6.1.2 Backgrounds to SelB

Figure 6.3 shows the signal and background ratios after the SelB selection (decay propagates via a $K^*(892)$) has been applied to the remaining sample. As with the SelA selection there is a contribution from $B_s \to D_s^{-*}(D_s^-\gamma)\pi^+$ and $B_s \to D_s^-\rho^+(\pi^+\pi^0)$. It is also evident that now we have a substantial contribution from $B_d \to D^-(K^-\pi^+\pi^-)\pi^+$ as well as a small peak from $\bar{\Lambda}_b \to \Lambda_c^-(\bar{p}K^+\pi^-)\pi^+$.

6.2 Defining the Signal PDFs

6.2.1 Mass PDF

The signal mass peak is fitted by a double Gaussian function. The mass projections and the fit results for a simultaneous fit to SelA and SelB MC10 data can be seen in Figures

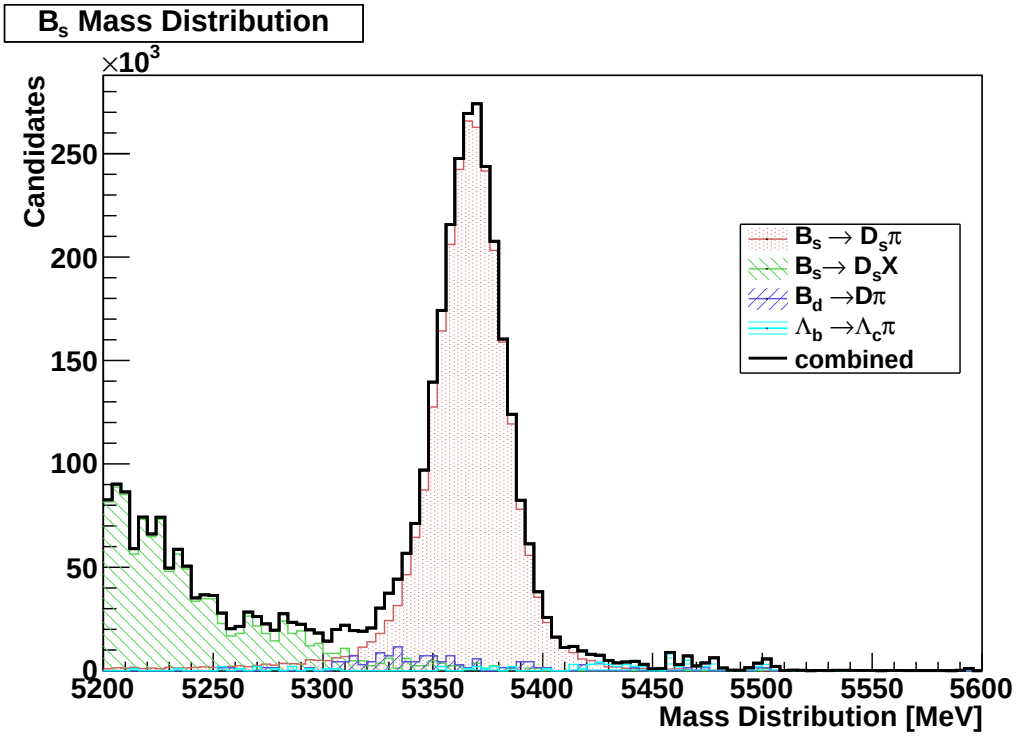

FIGURE 6.2: A normalised mass distribution of MC10 events passing the cuts SelA.

6.4, 6.5 and Table 6.3. The parameters of the double Gaussian are: $f_{\sigma_1^{sig}}$ gives the ratio between the two Gaussian, ${\sigma_m}^1$ the width of Gaussian one, $ratio_{21}^{sig}$ gives the ratio of the Gaussian widths and m_{B_s} gives the shared mean mass of the peak. In fits to data the ratio between the Gaussian widths and the fraction between the Gaussian functions will be fixed to these MC values to prevent the fit from using the wider Gaussian as a means to account for combinatoric background.

It can be seen that the double Gaussian is by no way a perfect fit to the B_s^0 mass peak. A systematic study is performed 8.1.3 comparing fitting using Crystal Ball and triple Gaussian signal mass models .

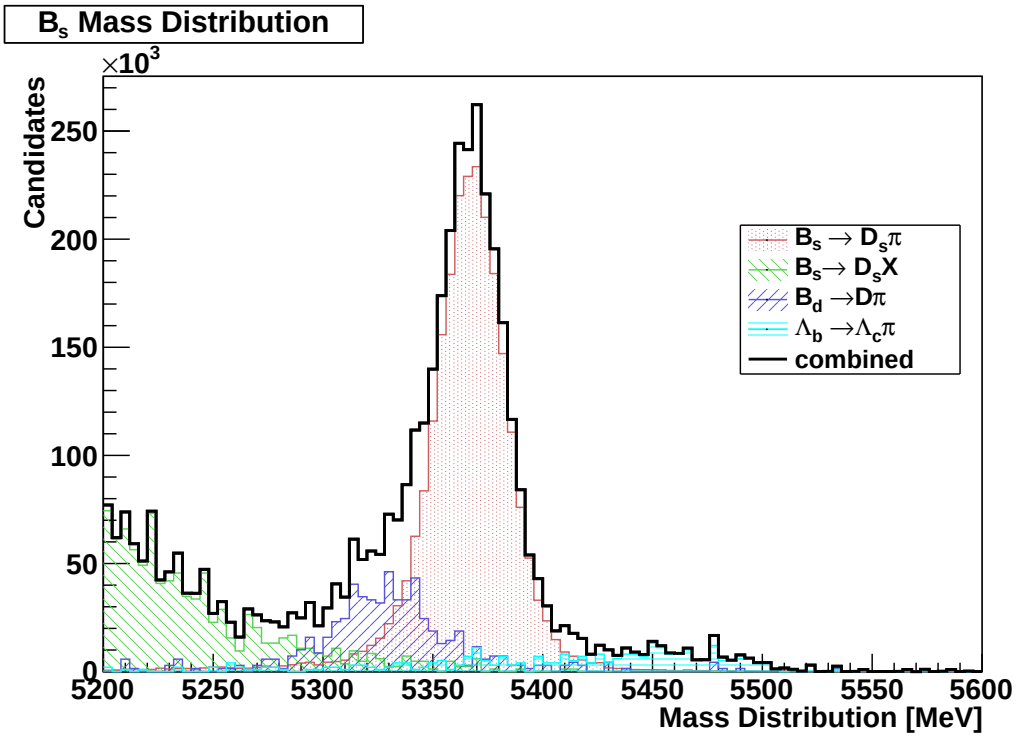

FIGURE 6.3: A normalised mass distribution of MC10 events passing the cuts SelB.

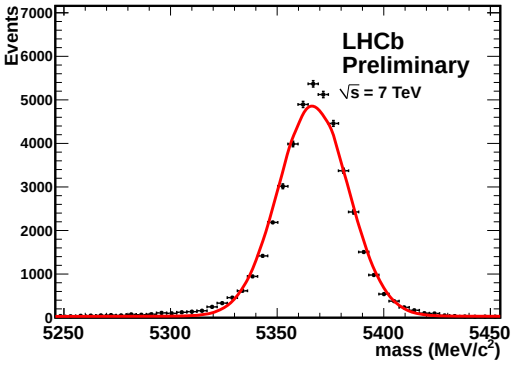

FIGURE 6.4: The SelA mass projection of a double Gaussian mass fit to the signal MC10.

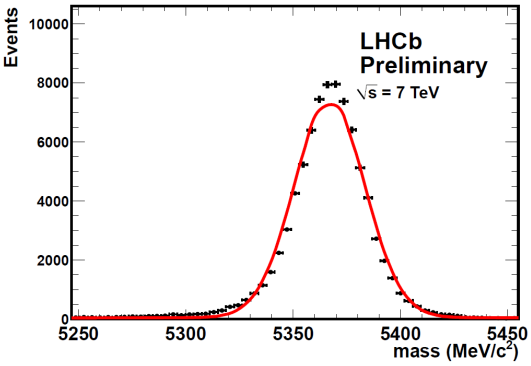

FIGURE 6.5: The SelB mass projection of a double Gaussian mass fit to the signal MC10.

Parameter	Fit result and error
$f_{\sigma_m{}^1}$	0.931 ± 0.001
$\sigma_m{}^1$	$16.6 \pm 0.1\,\mathrm{MeVc}^{-2}$
$(ratio_2 1)$	10.5 ± 0.1
m_{B_s}	$5367.2 \pm 0.1\,\mathrm{MeVc}^{-2}$

TABLE 6.3: The fit results of the double Gaussian mass fit to the signal MC10 SelA and SelB data set.

	$b\,\mathrm{ps}^{-1}$	n	$c\,\mathrm{ps}^{-1}$
ϵ_A	1.762 ± 0.092	1.206 ± 0.030	-0.0263 ± 0.0044
ϵ_B	1.772 ± 0.055	1.166 ± 0.019	-0.0258 ± 0.0034
ϵ_{AB}	1.766 ± 0.070	1.186 ± 0.022	-0.0261 ± 0.0032

TABLE 6.4: The fit results for the acceptance function in MC10 signal data in the full range $0 - 15\,\mathrm{ps}$ with c free

6.2.2 Lifetime PDF

The PDF is a double exponential based on Equation 3.29. By setting $\Delta\Gamma_s$ to $0\,\mathrm{ps}^{-1}$ we can fit for the single exponential Γ_{FS}. This theoretical distribution is modified by the proper-time acceptance (ϵ_{sig}) described in section 5.4.

The offset t_0 is fixed to 0.2 ps and the lower proper-time acceptance parameters b and n will be floated in the results. The upper proper-time acceptance parameter c is found from a MC study.

To obtain c the lifetime PDF was fitted to the MC10 dataset. The MC10 dataset has been generated with the same trigger definitions, stripping selection, and offline selection as the 2011 dataset.

Performing the study with Γ_s and $\Delta\Gamma_s$ fixed to the generator values $\Gamma_s = 0.68\,\mathrm{ps}^{-1}$ and $\Delta\Gamma_s = 0.06\,\mathrm{ps}^{-1}$ allows us to find the acceptance parameters. The fit was performed on each selection, as well as the combined data, in the proper-time region $0 - 15\,\mathrm{ps}$; the results are given in Table 6.4. It is evident that acceptance parameters, ϵ_{AB}, fitted to the combined data sets are consistent with both of the individual fits; hence the fits to data will use the value of the signal upper proper-time acceptance c given by the combined fits.

As a cross-check ϵ_{AB} was applied to a fit of Γ_s in the MC10 data. Table 6.5 gives the results of these fits. It is evident that each fit is within the error of the input value; the fit confirms that the acceptance parameters taken from the combined data gives us good fit.

ϵ parameters	MC10 data	$\Gamma_s\,\mathrm{ps}^{-1}$
ϵ_{AB}	SelA	0.680 ± 0.003
ϵ_{AB}	SelB	0.682 ± 0.003

TABLE 6.5: The Γ_s fit results for the acceptance functions applied to MC10 signal data in the full range $0 - 15\,\mathrm{ps}$

For completeness Figure 6.6 displays the acceptance shape given by parameters ϵ_{AB} in the proper-time range of interest $0-15\,\mathrm{ps}$. Figures 6.7 and 6.8 show the time projections of the fit to data sets MC10 SelA and MC10 SelB respectively.

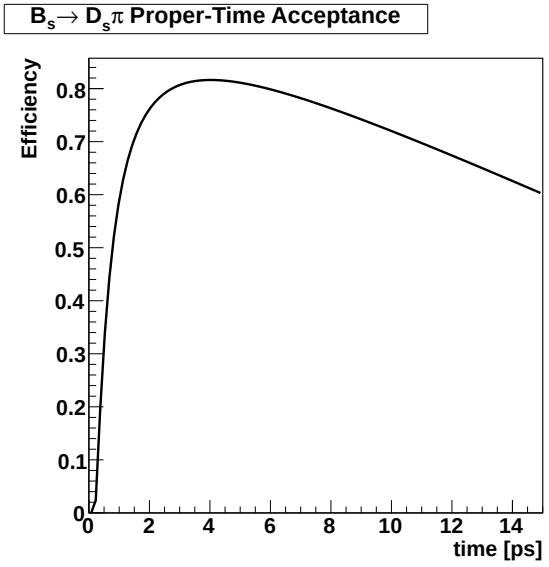

FIGURE 6.6: The shape acceptance parametrisation for ϵ_{AB}.

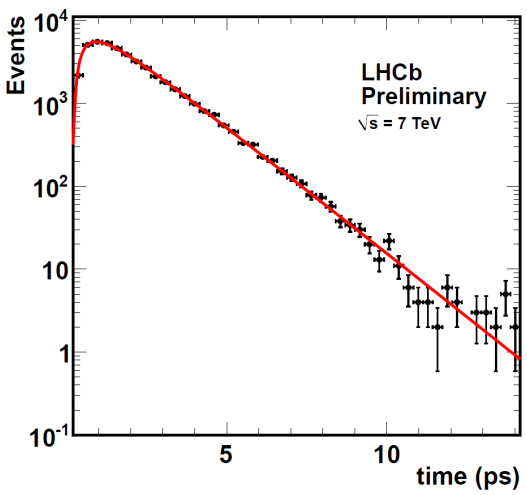

FIGURE 6.7: Fit to MC10 SelA data with defined acceptance model ϵ_{AB}.

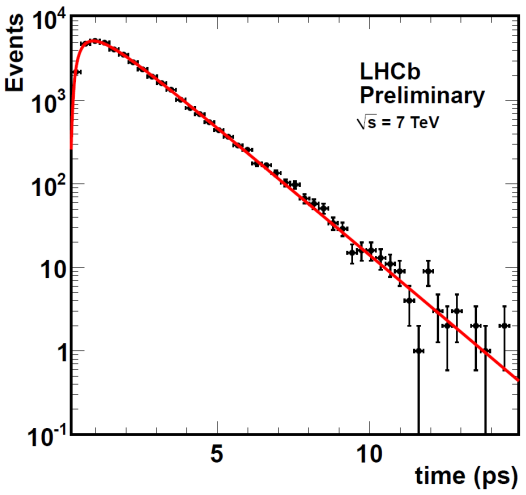

FIGURE 6.8: Fit to MC10 SelB data with defined acceptance model ϵ_{AB}.

6.3 Defining the Partially Reconstructed Background PDFs

Both selections SelA and SelB have a contribution from the partially reconstructed backgrounds. The partially reconstructed (PR) background consists of both $B_s \rightarrow D_s^{-*}(D_s^-\gamma)\pi^+$ and $B_s \rightarrow D_s^-\rho^+(\pi^+\pi^0)$. If modelled individually the ratio between the backgrounds would have to be known as they occur only in the same mass region; as the best guess at this ratio would come from MC it is therefore simpler to not separate them into two fits but keep them as one.

6.3.1 Mass PDF

The full mass histogram of the background from MC10 is shown in figure 6.9. If the fit is confined to the region $5200 - 5800\,\text{MeV}$ it can be seen in Figure 6.10 that the PR background can be modelled by a single exponential $PR\alpha_M$. In the fits to data $PR\alpha_M$ will be left free.

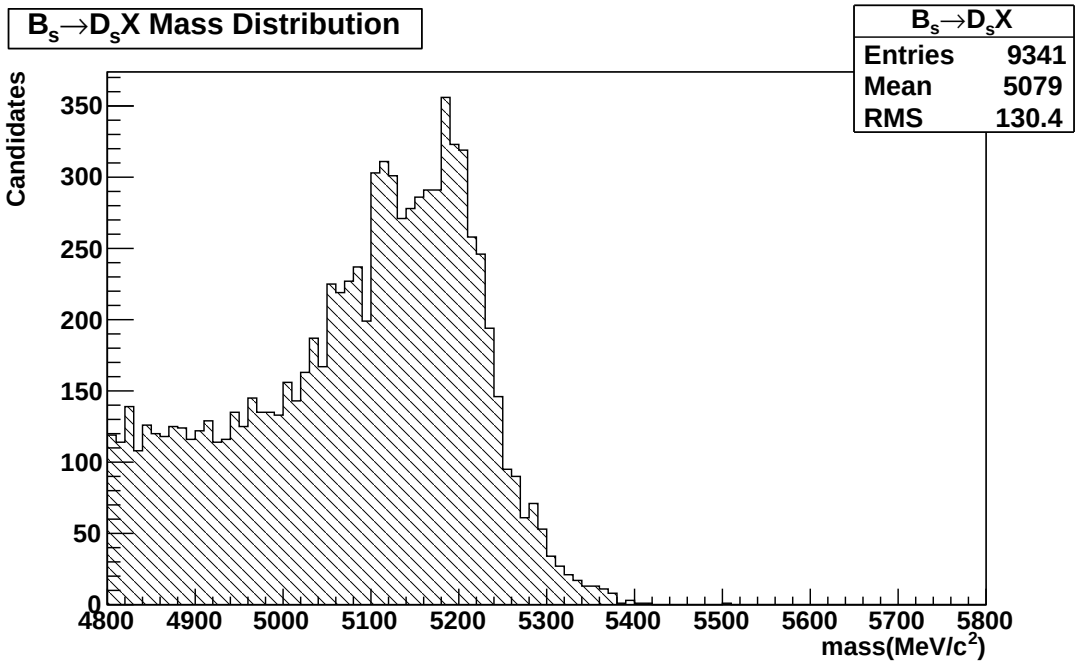

FIGURE 6.9: The Bs2DsX mass histogram from MC10.

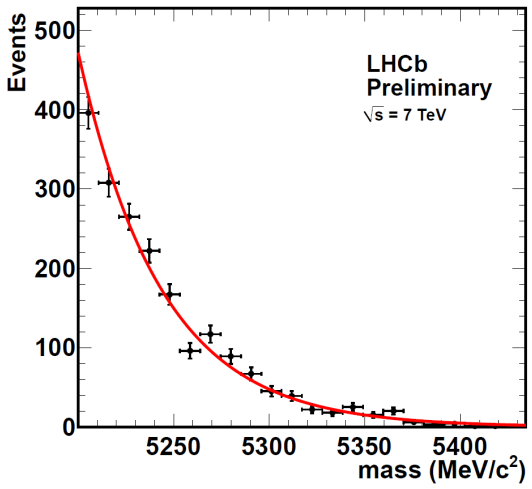

Parameter	Fit result and error
$PR\alpha_M$	0.0240 ± 0.0008

FIGURE 6.10: The mass projection and the fit results of the mass fit to the $B_s \rightarrow D_s(^*)X$ MC10 data set.

6.3.2 Lifetime PDF

The lifetime of the partially reconstructed background is modelled as a single exponential, of exponent $-\tau_{PR}$, with a proper-time acceptance bias ϵ_{PR} defined by b, n, c and t_0. In these fits we take $c = 0.0261\,\text{ps}^{-1}$ and $t_0 = 0.2\,\text{ps}$, while τ_{PR} is fixed to the PDG value $1.425\,\text{ps}$.

Figure 6.11 shows the results and lifetime projection plots of this fit to MC SelA data, and Figure 6.12 to MC SelB data. The large difference in acceptance parameter n in the SelA MC and SelB MC results is an indication of difference in distribution between the selections that will be further explored on the data fits in the lower B_s^0 mass side-band. When we fit to data the PR acceptance parameters b and n will be left free.

6.4 Defining the Mis-ID Background PDFs

Although there is no contribution from the mis-ID background in SelA data, contributions still remain in the SelB data. These backgrounds have reconstructed mass

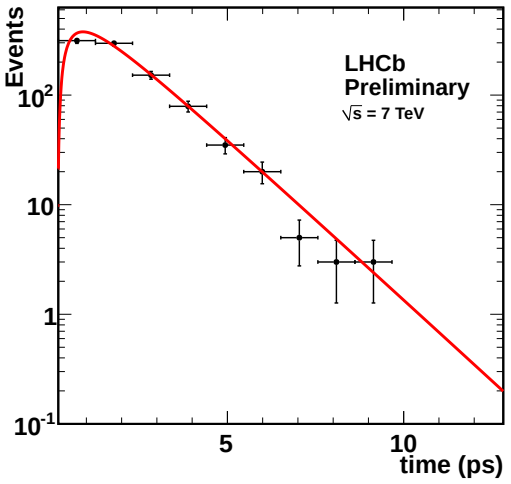

Parameter	Fit result and error
τ	1.425 ps
b	$1.77 \pm 0.42\,\text{ps}^{-1}$
n	1.07 ± 0.15
c	$-0.0261\,\text{ps}^{-1}$
t_0	0.2 ps

FIGURE 6.11: The time projection and the fit results of the proper-time fit to the $B_s \to D_s(^*)X$ MC10 SelA data set.

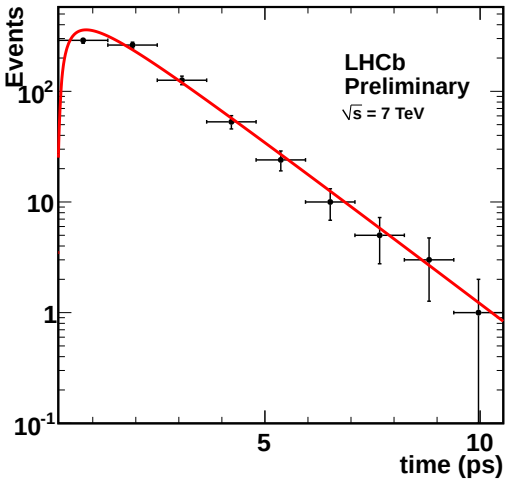

Parameter	Fit result and error
τ	1.425 ps
b	$2.06 \pm 0.58\,\text{ps}^{-1}$
n	1.02 ± 0.17
c	$-0.0261\,\text{ps}^{-1}$
t_0	0.2 ps

FIGURE 6.12: The time projection and the fit results of the proper-time fit to the $B_s \to D_s(^*)X$ MC10 SelB data set.

distributions that extend under the B_s^0 mass region and so it is extremely important to correctly model their shape and proper-time.

6.4.1 The $\bar{\Lambda}_b$ Background

6.4.1.1 Mass PDF

The $\bar{\Lambda}_b$ background can be fitted by using a Crystal Ball function. The Crystal Ball function describes a single Gaussian with power-law tail [48]. It is defined by its Gaussian parameters σ and *mean* as well as the parameters of the power-law tail α and η. Figure 6.13 shows the fit to MC10 $\bar{\Lambda}_b \to \Lambda_c^-(\bar{p}K^+\pi^-)\pi^+$ data that has passed SelB. All the mass parameters will be fixed to the MC values when the fit is performed on data.

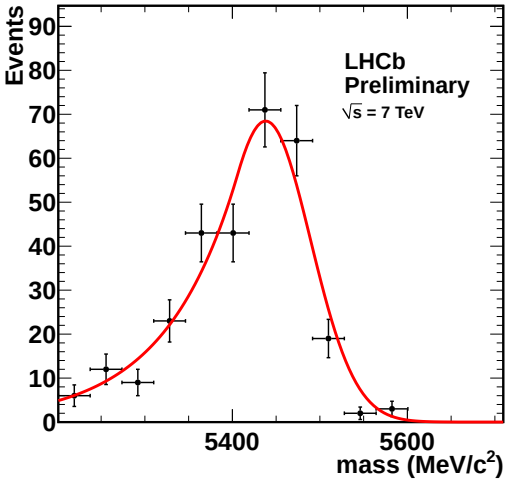

Parameter	Fit result and error
$\sigma_m^{\Lambda_b}$	$51.2 \pm 4.4\,\mathrm{MeVc}^{-2}$
$\alpha_m^{\Lambda_b}$	0.62 ± 0.11
$\eta_m^{\Lambda_b}$	125 ± 75
$mean^{\Lambda_b}$	$5437.9 \pm 6.2\,\mathrm{MeVc}^{-2}$

FIGURE 6.13: The mass projection and the fit results of the mass fit to the $\bar{\Lambda}_b$ MC10 data set selected using SelB.

6.4.1.2 Lifetime PDF

The lifetime of the $\bar{\Lambda}_b$ background can again be modelled as a single exponential of the PDG Λ_b lifetime with a proper-time acceptance bias. The fit projection and results to MC10 data of this background are given by Figure 6.14. In the fit to data the acceptance parameters will be fixed to these MC values.

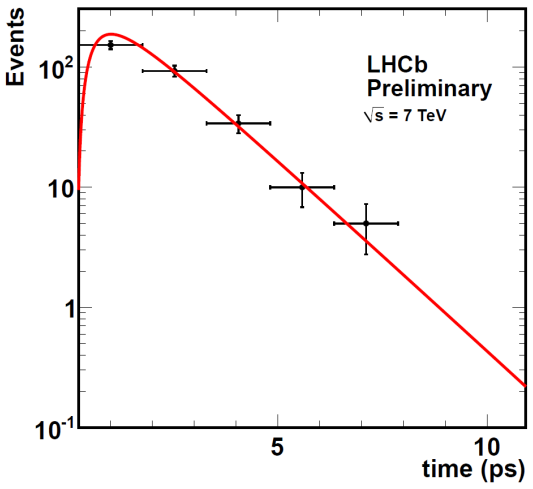

Parameter	Fit result and error
(τ^{Λ_b})	1.425 ps
$(t_0^{\Lambda_b})$	0.2 ps
(b^{Λ_b})	$1.71 \pm 0.43\,\text{ps}^{-1}$
(c^{Λ_b})	$-0.0261\,\text{ps}^{-1}$
(n^{Λ_b})	1.88 ± 0.33

FIGURE 6.14: The time projection and the fit results of the proper-time fit to the $\bar{\Lambda}_b \to \Lambda_c X$ MC10 data set.

6.4.2 The B_d Background

6.4.2.1 Mass PDF

The B_d mass peak is fitted well by a double Gaussian function. The parameters of the double Gaussian are: mean^{B_d}, the shared mean of the Gaussians; $f_{\sigma_1}^{B_d}$ being the fraction between them; the widths of the Gaussians are $\sigma_1^{B_d}$ and $\sigma_2^{B_d}$. Figure 6.15 shows the fit to MC10 $B_d \to D\pi$ data that has passed SelB. All fit parameters will be fixed from MC when the fit is performed on data with the exception of the fraction of this background which can be fitted from the 'shoulder' of the B_s^0 mass peak.

6.4.2.2 Lifetime PDF

The lifetime of the B_d background can again be modelled as a single exponential of the PDG B_d lifetime, with a proper-time acceptance bias. The fit and fit parameters to MC10 data of this background are given by Figure 6.16. The large uncertainties on the acceptance parameters indicate that there is too little MC data to accurately model the proper-time acceptance distribution seen by this background.

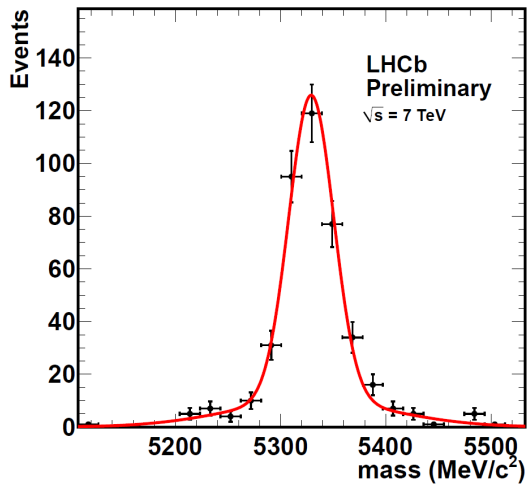

Parameter	Fit result and error
$f_{\sigma_m{}^1}$	$0.765 \pm 0.048\,\mathrm{MeVc}^{-2}$
$(\sigma_1^{B_d})$	$21.3 \pm 1.5\,\mathrm{MeVc}^{-2}$
$(\sigma_2^{B_d})$	$77.2 \pm 8.3\,\mathrm{MeVc}^{-2}$
$(mean^{B_d})$	$5329.1 \pm 1.4\,\mathrm{MeVc}^{-2}$

FIGURE 6.15: The mass projection and the fit results of the mass fit to the $B_d \to D\pi$ data set selected using SelB.

Proper-time acceptance is caused by the topology of the decay. As the decay channels $B_d \to D^-(K^-\pi^+\pi^-)\pi^+$ and $\bar{\Lambda}_b \to \Lambda_c^-(\bar{p}K^+\pi^-)\pi^+$ have near identical topologies the acceptance parameters determined in the Λ_b fit will be used for the entire mis-ID background.

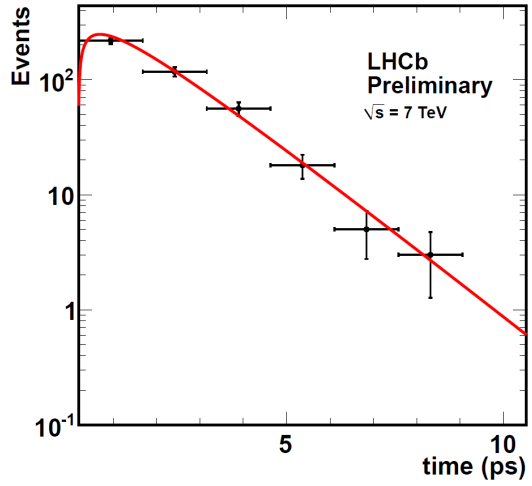

Parameter	Fit result and error
(τ^{B_d})	$1.519\,\mathrm{ps}$
$(t_0^{B_d})$	$0.2\,\mathrm{ps}$
(b^{B_d})	$0.38 \pm 1.05\,\mathrm{ps}^{-1}$
(c^{B_d})	$-0.0261\,\mathrm{ps}^{-1}$
(n^{B_d})	0.49 ± 0.19

FIGURE 6.16: The time projection and the fit results of the proper-time fit to the $B_s \to D_s(^*)X$ data set.

Chapter 7

Lifetime Fitting Results

The data used for this analysis is the LHCb 2011 data available up until the 7th July; this corresponds to $340\,\mathrm{pb}^{-1}$. The selection was applied to all of the candidates that pass the stripping line, with no other cuts applied prior to those specified in Section 5.2.

At the time that this analysis was performed the LHCb detector momentum scale was not calibrated, and as a result of this the momentum of particles in the data sets are shifted from their physical values. A comparison of the B_s^0 mass seen in MC to the mass found from a fit to data yields a mass shift of $-7.4\,\mathrm{MeVc}^{-2}$. This shift has been accounted for in the applied selection cuts, the fit range, and the fit values dependent on absolute mass.

This chapter will first use the fits to the B_s^0 mass side-bands to check the background models, followed by full fits to SelA and SelB datasets, as well as a simultaneous fit to both. Each section will show the projection plots and fit results for the full $(0 - 15\,\mathrm{ps})$ fit to Γ_{FS}. Lastly, a fit to Γ_s will be performed with constraints on Γ_s and $\Delta\Gamma_s$ taken from the $B_s \to J/\psi\phi$ measurement.

7.1 The Fitting Model Summarised

For the convenience of the reader, Table 7.1 provides a summary of the models used by each PDF and the fit parameters used by these models. Each PDF has been discussed previously in their relevant sections in Chapter 6 with the exception of the PDFs describing the combinatoric background which can only be defined directly from data. The combinatoric PDFs are summarised here, and are presented in full in the Section 7.2.1.

PDF		Model	Parameters	Description
Signal	mass	Double Gaussian	$frac_{\sigma 1}^{sig}$	Fraction between Gaussians
			$\sigma 1^{sig}$	First Gaussian width
			$ratio_{21}^{sig}$	Ratio between σ_1 and σ_2
			m_{B_s}	Shared Gaussian mean
	lifetime	Single exponential multiplied by proper-time acceptance ϵ^{sig}	Γ_{FS}	A single exponential
			t_0^{sig}	ϵ offset
			n^{sig}	ϵ power
			b^{sig}	ϵ lower slope parameter
			c^{sig}	ϵ upper slope parameter
bkg^{comb}	mass	Single exponential	α_M^{comb}	Exponent
	lifetime	Crystal Ball multiplied by proper-time acceptance ϵ^{comb}	σ^{comb}	Gaussian Width
			α^{comb}	CB parameter
			η^{comb}	CB parameter
			t_0^{comb}	ϵ offset
			b^{comb}	ϵ lower slope parameter
			Y^{comb}	ϵ turn-over parameter
bkg^{PR}	mass	Single exponential	α_M^{PR}	Exponent
	lifetime	Single exponential multiplied by proper-time acceptance ϵ^{PR}	τ^{PR}	Exponent
			t_0^{PR}	ϵ offset
			n^{PR}	ϵ power
			b^{PR}	ϵ lower slope parameter
			c^{PR}	ϵ upper slope parameter
bkg^{B_d}	mass	Double Gaussian	$frac_{\sigma 1}^{B_d}$	Fraction between Gaussians
			$\sigma_1^{B_d}$	First Gaussian width
			$\sigma_2^{B_d}$	Second Gaussian width
			$mean^{B_d}$	shared Gaussian mean
	lifetime	Single exponential multiplied by proper-time acceptance ϵ^{mis-ID}	τ^{B_d}	Exponent
			t_0^{mis-ID}	ϵ offset
			n^{mis-ID}	ϵ power
			b^{mis-ID}	ϵ lower slope parameter
			c^{mis-ID}	ϵ upper slope parameter
bkg^{Λ_b}	mass	Crystal Ball	σ^{Λ_b}	Gaussian Width
			α^{Λ_b}	CB parameter
			η^{Λ_b}	CB parameter
			$mean^{\Lambda_b}$	Gaussian mean
	lifetime	Single exponential multiplied by proper-time acceptance ϵ^{mis-ID}	τ^{Λ_b}	Exponent
			ϵ^{mis-ID}	see signal acceptance

TABLE 7.1: A summary of the model and the fit parameters used in each PDF. ϵ refers to a proper-time acceptance function.

7.2 Verifying the Background Models from Side-Bands

In this section fits are performed to the B_s^0 upper mass side-band in order to construct a PDF to describe the combinatoric background. A simultaneous fit between SelA and SelB dataset's upper and lower mass side-bands will then be performed. The fit parameters will not be used in the results, rather it is to verify the PDFs and to give an idea of the values expected for the background PDF parameters.

7.2.1 Modelling the Combinatoric Background

The upper B_s^0 mass side-band $5500-5800\,\mathrm{MeVc}^{-2}$ is entirely composed of combinatoric backgrounds so this was used to determine and test the PDF. Combinatoric background arises from an assortment of random tracks that pass the selection criteria. Some of these may be from prompt background, and others from long-lived B decays; therefore it is expected to have a short-lived and long-lived contribution. The mass PDF for the combinatoric background is a single exponential of negative exponent $-\alpha_M^{comb}$; the lifetime PDF is modelled by a Crystal Ball function with $mean = 0\,\mathrm{ps}$ and free parameters: σ^{comb}, α^{comb} and η^{comb} as well as a proper-time acceptance. The Crystal Ball function gives us a Gaussian component with which to define the prompt background, and a power-law tail to define the long lived contribution.

The acceptance function used for the combinatoric background is developed as an ansatz to fit the data. It is of the form:

$$\epsilon^{comb} = (1 - Y) + Y(1 - e^{(-b(t-t_0)}) \tag{7.1}$$

where t_0 again represents the off-set of the function which is fixed to 0.2 ps due to IP cuts, and parameters b and Y govern the distribution. The form of the acceptance can be seen in Figure 7.1 with input parameters $b = 8$, $Y = 0.3$ and $t_0 = 0.2\,\mathrm{ps}$; it is evident that the function is 0 at proper-times less than 0.2 ps, the function switches on at $1-Y$ and rises to 1 in accordance with the exponential term governed by b.

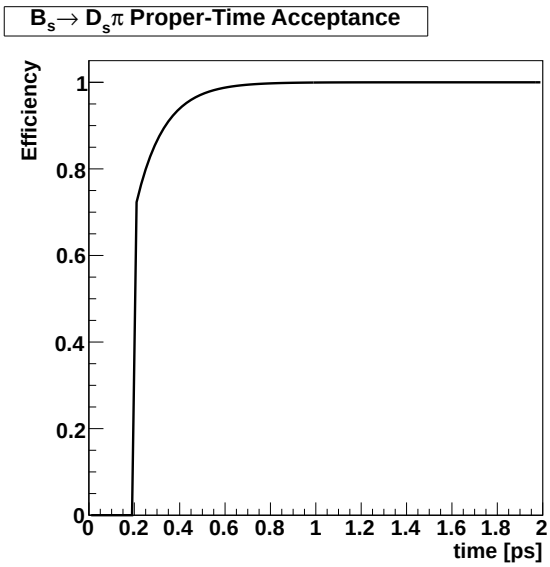

FIGURE 7.1: The shape acceptance parametrisation for ϵ^{comb}.

The fit and fit results for the mass distribution can be seen in Figure 7.2 and for the time distribution in Figure 7.3. These fit values will not be used for the results, rather they are presented to confirm that the PDFs give good descriptions of the data.

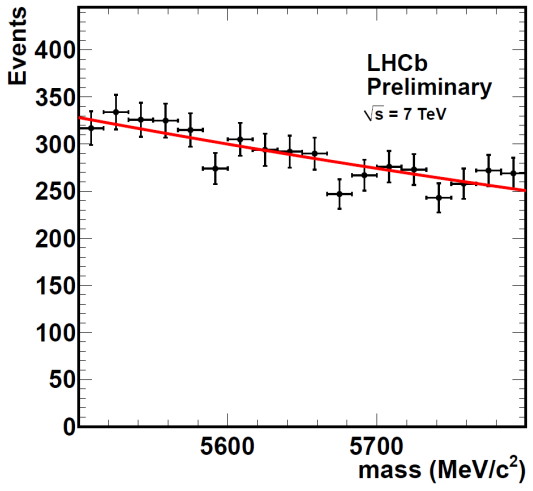

Parameter	Fit result and error
α_M^{comb}	0.0009 ± 0.0002

FIGURE 7.2: The mass projection and the fit results of a single exponential fit to the mass distribution of the combinatoric background in the B_s^0 upper mass side-band.

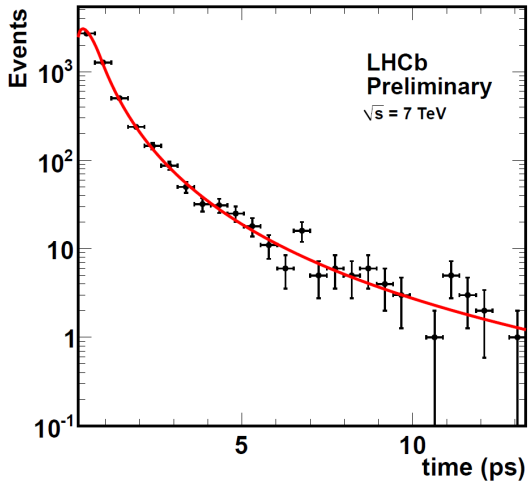

Parameter	Fit result and error
σ	$0.605 \pm 0.029\,\text{ps}$
α	-1.433 ± 0.048
η	2.93 ± 0.16
t_0	$0.2\,\text{ps}$
b	$9.6 \pm 6.5\,\text{ps}^{-1}$
Y	0.328 ± 0.068

FIGURE 7.3: The time projection and the fit results of a Crystal Ball and proper-time acceptance fit to the lifetime distribution of the combinatoric background in the B_s^0 upper mass side-band.

7.2.2 A Simultaneous Fit to the B_s^0 Mass Side-Bands

Fitting to the B_s^0 mass side-bands allows us to verify the contribution from the partially reconstructed background is as expected.

The lower B_s^0 mass side-band ($5188 - 5300\,\mathrm{MeVc}^{-2}$) has contributions from the combinatoric, partially reconstructed backgrounds and the B_d background; the upper B_s^0 mass side-band ($5500 - 5800\,\mathrm{MeVc}^{-2}$) only contains combinatoric backgrounds. A simultaneous fit is performed to the upper and the lower B_s^0 mass side-bands; the lower mass side-band is free to fit for both partially reconstructed and combinatoric backgrounds as well as the fraction between them, whereas the upper side-band only includes a PDF model for the combinatoric background. The simultaneous fit to the B_s^0 mass side-bands will yield the acceptance of the PR background distribution.

The SelA mass projections for the lower and upper side-bands are given in Figures 7.4 and 7.6; the lifetime projections can be seen in Figures 7.5 and 7.7.

The SelB mass projections for the lower and upper side-bands are given in Figures 7.10 and 7.12; the lifetime projections can be seen in Figures 7.11 and 7.13.

The full fit results are presented in Table 7.2.

A closer inspection of the lower proper-time region is shown in Figures 7.8 and 7.9. It is evident that both the lifetime models and the acceptance models provide a good fit to this background

It is evident that that the PR background acceptance parametrisations between the SelA and SelB datasets are not consistent with each other and therefore will be handled separately for each dataset. The acceptance parameters will be left free to fit in the data. The parameters describing the combinatoric background are consistent between the fits to SelA and SelB data, so these will be shared parameters in the simultaneous fit; again these will be left free.

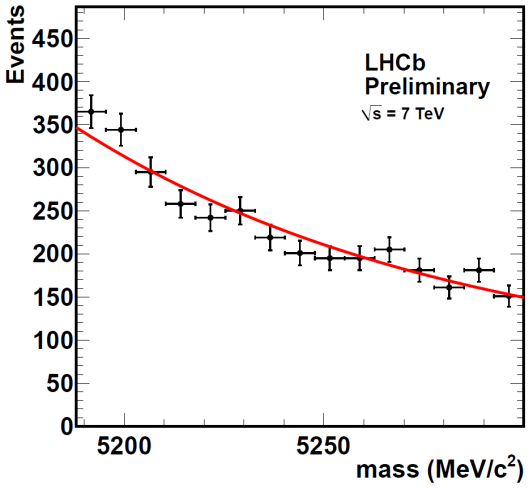

FIGURE 7.4: Projection of the lower mass side-band mass distribution and fit to the SelA dataset.

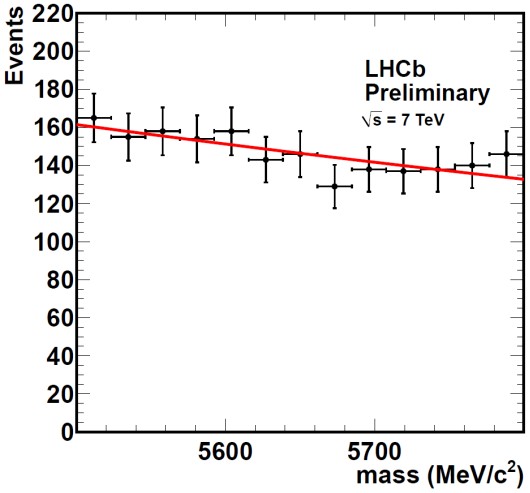

FIGURE 7.6: Projection of the upper mass side-band mass distribution and fit to the SelA dataset.

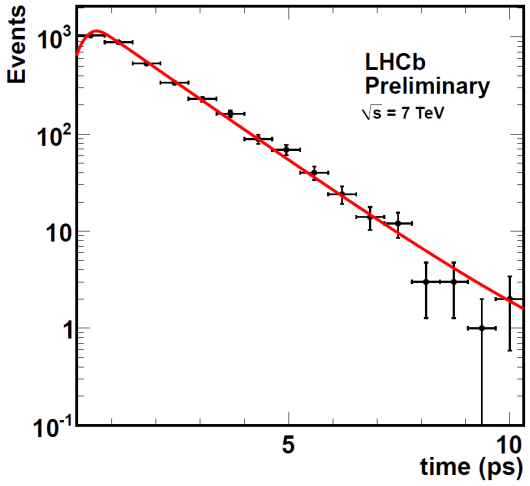

FIGURE 7.5: Projection of the lower mass side-band time distribution and fit to the SelA dataset.

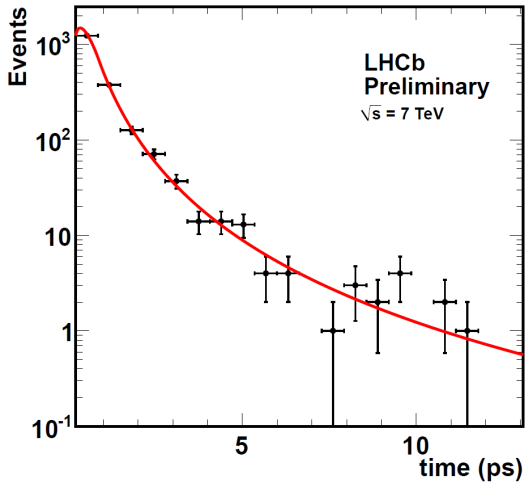

FIGURE 7.7: Projection of the upper mass side-band time distribution and fit to the SelA dataset.

				Fit Result and Error	
PDF		Parameters	Usage	SelA	SelB
bkg^{comb}	mass	α_M^{comb}	Free	0.0007 ± 0.0003	0.0012 ± 0.0002
	lifetime	σ^{comb}	Free	$0.611 \pm 0.036\,\text{ps}$	
		α^{comb}	Free	-1.426 ± 0.045	
		η^{comb}	Free	3.03 ± 0.17	
		t_0^{comb}	Fixed	$0.2\,\text{ps}$	
		b^{comb}	Free	$9.9 \pm 8.7\,\text{ps}^{-1}$	
		Y^{comb}	Free	0.305 ± 0.063	
bkg^{PR}	mass	α_M^{PR}	Free	0.0106 ± 0.0007	0.0108 ± 0.0013
	lifetime	τ^{PR}	Fixed	$1.425\,\text{ps}$	
		t_0^{PR}	Fixed	$0.2\,\text{ps}$	
		n^{PR}	Free	2.06 ± 0.24	
		b^{PR}	Free	$2.23 \pm 0.24\,\text{ps}^{-1}$	$2.93 \pm 0.47\,\text{ps}^{-1}$
		c^{PR}	Fixed	$-0.0261\,\text{ps}^{-1}$	
bkg^{B_d}	mass	$frac_{\sigma 1}^{B_d}$	Fixed	–	0.765
		$\sigma_1^{B_d}$	Fixed	–	$21.3\,\text{MeVc}^{-2}$
		$\sigma_2^{B_d}$	Fixed	–	$77.2\,\text{MeVc}^{-2}$
		$mean^{B_d}$	Fixed	–	$5321.1\,\text{MeVc}^{-2}$
	lifetime	τ^{B_d}	Fixed	–	$1.519\,\text{ps}$
		t_0^{mis-ID}	Fixed	–	$0.2\,\text{ps}$
		n^{mis-ID}	Fixed	–	1.88
		b^{mis-ID}	Fixed	–	$1.71\,\text{ps}^{-1}$
		c^{mis-ID}	Fixed	–	$-0.261\,\text{ps}^{-1}$
PDF Fractions	Comb bkg/Total bkg		Free	0.294 ± 0.022	0.347 ± 0.027
	PR bkg/Non-comb bkgs		Free	–	0.89 ± 0.02

TABLE 7.2: Fit results of the full simultaneous fit to SelA and SelB B_s^0 mass side-bands

7.3 Γ_{FS} from Data

The following sections present the fit results to SelA and SelB datasets individually, as well as a simultaneous fit to them both. Each fit uses the signal, partially reconstructed background and combinatoric background PDFs, with the fits to SelB data also making use of the B_d and Λ_b PDFs. A summary of the functions used by each PDF can be found in reference Table 7.1.

In all fits the signal acceptance parameters b and n are floated with t_0 fixed to $0.2\,\text{ps}$ and $c = -0.0261\,\text{ps}^{-1}$. The signal mass model restricts all the parameters of the double

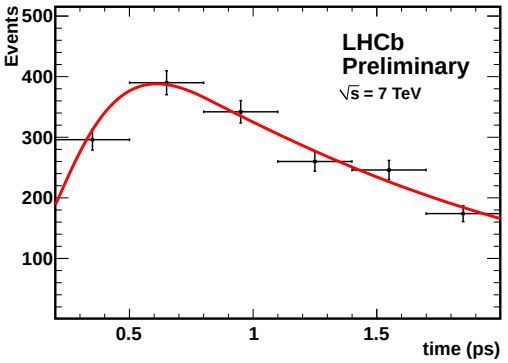

FIGURE 7.8: Projection of the lower side-band time distribution and fit to the SelA dataset in the lower proper-time acceptance region to demonstrate the fit to the proper-time acceptance.

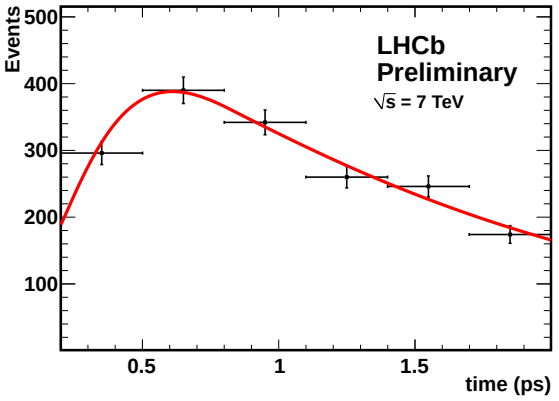

FIGURE 7.9: Projection of the upper side-band time distribution and fit to the SelA dataset in the lower proper-time acceptance region to demonstrate the fit to the proper-time acceptance.

Gaussian to the MC values with the exception of the Gaussian width (σ_1^{sig}) which is floated. The PR background is free to fit the mass exponent (α_M) and acceptance parameters b and n. Again $t_0 = 0.2\,\text{ps}$ and $c = -0.0261\,\text{ps}^{-1}$, the lifetime is also fixed to 1.425 ps.

The combinatoric background mass, lifetime and proper-time acceptance parameters are all floated as these can all be fitted from information in the upper B_s^0 mass side-band.

The B_d and Λ_b backgrounds are described entirely from MC.

7.3.1 Fits to SelA Data

The fit results for Γ_{FS} are given in Table 7.3, with the mass and time projection plots shown in Figures 7.14 and 7.15 respectively. The full correlation matrix can be found in Appendix B Table B.1.

12272 events are fitted; the numbers of events categorised under each PDF are shown in Table 7.4. The result of interest from the SelA dataset is $\Gamma_{FS} = 0.676 \pm 0.023\,\text{ps}^{-1}$. Γ_{FS}

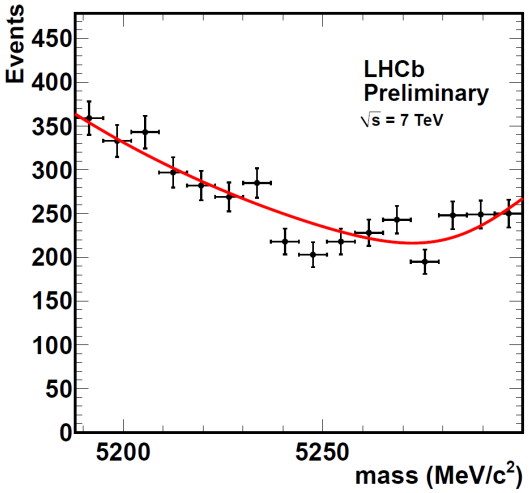

FIGURE 7.10: Projection of the lower mass side-band mass distribution and fit to the SelB dataset.

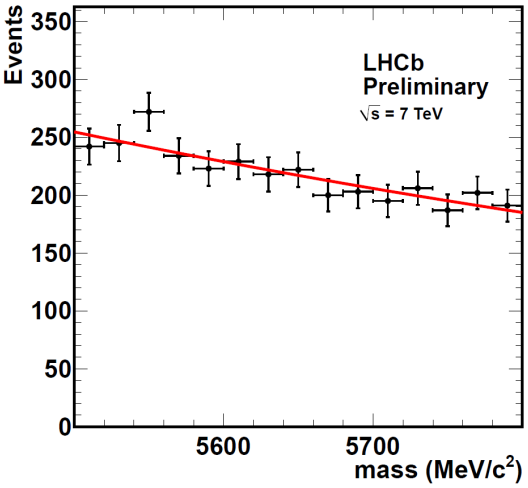

FIGURE 7.12: Projection of the upper mass side-band mass distribution and fit to the SelB dataset.

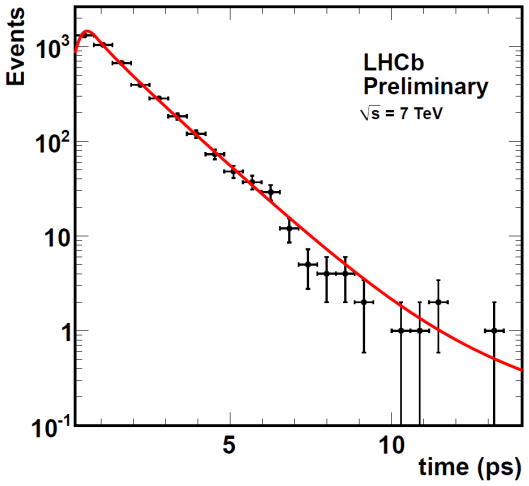

FIGURE 7.11: Projection of the lower mass side-band time distribution and fit to the SelB dataset.

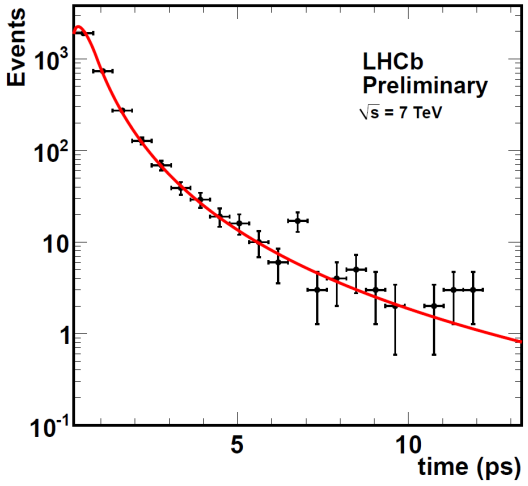

FIGURE 7.13: Projection of the upper mass side-band time distribution and fit to the SelB dataset.

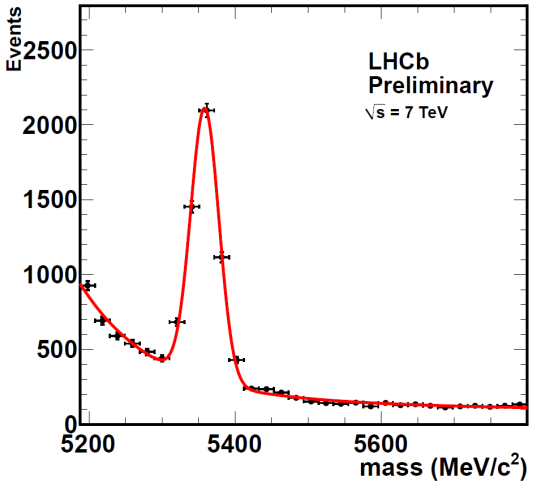

FIGURE 7.14: Mass projection of $0 - 15\,\text{ps}$ fit to SelA.

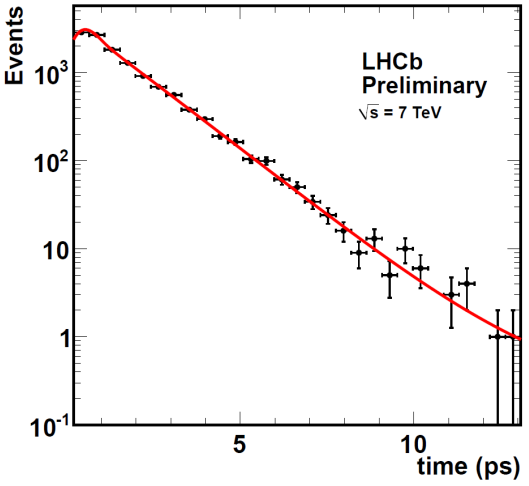

FIGURE 7.15: Time projection of $0 - 15\,\text{ps}$ fit to SelA.

is highly correlated with the signal proper-time acceptance functions, $\rho_{\Gamma_{FS},b^{sig}} = -0.85$, $\rho_{\Gamma_{FS},n^{sig}} = -0.62$, which accounts for the large uncertainty on the fit.

7.3.2 Fits to SelB Data

The fit results are summarised in Table 7.5; the mass and time projection plots are given in 7.16 and 7.17 respectively. Again the correlation matrix can be found in C.

15588 events are fitted. The numbers of events categorised under each PDF are shown in Table 7.6. The fit to the SelB dataset gives $\Gamma_{FS} = 0.658 \pm 0.025\,\text{ps}^{-1}$. Γ_{FS} is highly correlated with the signal proper-time acceptance functions, $\rho_{\Gamma_{FS},b^{sig}} = -0.8$, $\rho_{\Gamma_{FS},n^{sig}} = -0.61$, which accounts for the large uncertainty on the fit.

7.3.3 Simultaneous Fits to SelA and SelB Datasets

The measurement of Γ_{FS} from the individual fits to SelA and SelB datasets are consistent with each other. Here a simultaneous fit to both datasets is presented.

PDF		Parameters	Usage in fit	Fit Result and Error
Signal	mass	$frac_{\sigma_1}^{sig}$	Fixed	0.93
		$\sigma 1^{sig}$	Free	$19.31 \pm 0.37\,\mathrm{MeVc^{-2}}$
		$ratio_{21}^{sig}$	Fixed	10.5
		m_{B_s}	Free	$5358.6 \pm 0.4\,\mathrm{MeVc^{-2}}$
	lifetime	$\mathbf{\Gamma_{FS}}$	Free	$\mathbf{0.676 \pm 0.023}\,\mathrm{ps^{-1}}$
		t_0^{sig}	Fixed	$0.2\,\mathrm{ps}$
		n^{sig}	Free	1.15 ± 0.15
		b^{sig}	Free	$1.79 \pm 0.44\,\mathrm{ps^{-1}}$
		c^{sig}	Fixed	$-0.0261\,\mathrm{ps^{-1}}$
bkg^{comb}	mass	α_M^{comb}	Free	0.0005 ± 0.0002
	lifetime	σ^{comb}	Free	$0.626 \pm 0.022\,\mathrm{MeVc^{-2}}$
		α^{comb}	Free	-1.689 ± 0.097
		η^{comb}	Free	2.79 ± 0.30
		t_0^{comb}	Fixed	$0.2\,\mathrm{ps}$
		b^{comb}	Free	$25 \pm 36\,\mathrm{ps^{-1}}$
		Y^{comb}	Free	0.05 ± 0.12
bkg^{PR}	mass	α_M^{PR}	Free	0.0101 ± 0.0004
	lifetime	τ^{PR}	Fixed	$1.425\,\mathrm{ps}$
		t_0^{PR}	Fixed	$0.2\,\mathrm{ps}$
		n^{PR}	Free	1.80 ± 0.38
		b^{PR}	Free	$2.45 \pm 0.26\,\mathrm{ps^{-1}}$
		c^{PR}	Fixed	$-0.0261\,\mathrm{ps^{-1}}$
PDF Fractions	Signal Events/Total Events		Free	0.371 ± 0.007
	Comb bkg/Total bkg Events		Free	0.498 ± 0.021

TABLE 7.3: Fit results of the full fit to SelA data.

PDF	Percentage	# Events
Signal	37.1%	4553
Combinatoric Background	31.3%	3841
PR Background	31.6%	3878

TABLE 7.4: The percentage of the fit to SelA data allocated to each PDF and the corresponding number of events.

PDF		Parameters	Usage in fit	Fit Result and Error
Signal	mass	$frac_{\sigma 1}^{sig}$	Fixed	0.93
		$\sigma 1^{sig}$	Free	$17.00 \pm 0.53\,\mathrm{MeVc}^{-2}$
		$ratio_{21}^{sig}$	Fixed	10.5
		m_{B_s}	Free	$5359.0 \pm 0.6\,\mathrm{MeVc}^{-2}$
	lifetime	$\mathbf{\Gamma_{FS}}$	Free	$\mathbf{0.658 \pm 0.025}\,\mathrm{ps}^{-1}$
		t_0^{sig}	Fixed	0.2 ps
		n^{sig}	Free	1.45 ± 0.25
		b^{sig}	Free	$2.53 \pm 0.47\,\mathrm{ps}^{-1}$
		c^{sig}	Fixed	$-0.0261\,\mathrm{ps}^{-1}$
bkg^{comb}	mass	α_M^{comb}	Free	0.0007 ± 0.0002
	lifetime	σ^{comb}	Free	0.605 ± 0.028 ps
		α^{comb}	Free	-1.593 ± 0.080
		η^{comb}	Free	2.71 ± 0.32
		t_0^{comb}	Fixed	0.2 ps
		b^{comb}	Free	$7.3 \pm 4.8\,\mathrm{ps}^{-1}$
		Y^{comb}	Free	0.385 ± 0.048
bkg^{PR}	mass	α_M^{PR}	Free	0.0112 ± 0.0012
	lifetime	τ^{PR}	Fixed	0.1425 ps
		t_0^{PR}	Fixed	0.2 ps
		n^{PR}	Free	2.29 ± 0.43
		b^{PR}	Free	$2.56 \pm 0.34\,\mathrm{ps}^{-1}$
		c^{PR}	Fixed	$-0.261\,\mathrm{ps}^{-1}$
bkg^{B_d}	mass	$frac_{\sigma 1}^{B_d}$	Fixed	0.765
		$\sigma_1^{B_d}$	Fixed	$21.3\,\mathrm{MeVc}^{-2}$
		$\sigma_2^{B_d}$	Fixed	$77.2\,\mathrm{MeVc}^{-2}$
		$mean^{B_d}$	Fixed	$5321.1\,\mathrm{MeVc}^{-2}$
	lifetime	τ^{B_d}	Fixed	1.519 ps
		t_0^{mis-ID}	Fixed	0.2 ps
		n^{mis-ID}	Fixed	1.88
		b^{mis-ID}	Fixed	$1.71\,\mathrm{ps}^{-1}$
		c^{mis-ID}	Fixed	$-0.261\,\mathrm{ps}^{-1}$
bkg^{Λ_b}	mass	σ^{Λ_b}	Fixed	$51.2\,\mathrm{MeVc}^{-2}$
		α^{Λ_b}	Fixed	0.62
		η^{Λ_b}	Fixed	125
		$mean^{\Lambda_b}$	Fixed	$5430\,\mathrm{MeVc}^{-2}$
	lifetime	τ^{Λ_b}	Fixed	1.425 ps
		ϵ^{mis-ID}	–	––
PDF Fractions	Signal Events/Total Events		Free	0.222 ± 0.006
	Comb bkg/Total bkg		Free	0.592 ± 0.020
	PR bkg/Non-comb bkgs		Free	0.655 ± 0.042
	B_d bkg/Miss-ID bkg		Free	0.726 ± 0.037

TABLE 7.5: Fit results of the full fit to SelB data.

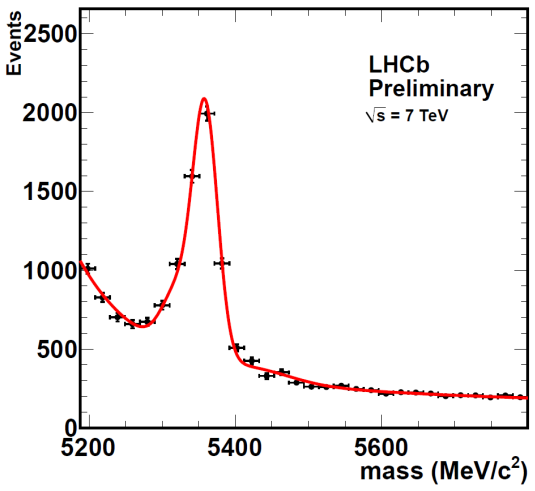

FIGURE 7.16: Mass projection of 0 – 15 ps fit to SelB with signal proper-time acceptance parameters free.

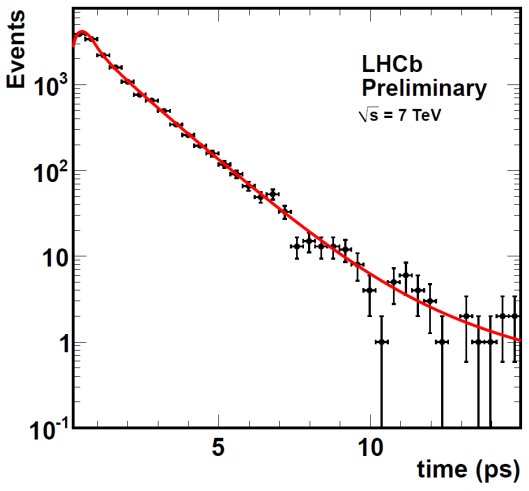

FIGURE 7.17: Time projection of 0 – 15 ps fit to SelB with signal proper-time acceptance parameters free.

PDF	Percentage	# Events
Signal	22.2%	3461
Combinatoric Background	46.1%	7186
PR Background	20.8%	3242
B_d Background	8.0%	1247
Λ_b Background	3.0%	468

TABLE 7.6: The percentage of the fit to SelB data allocated to each PDF and the corresponding number of events.

The shared parameters are those of the B_s^0 signal mass distribution, the signal acceptance ϵ^{sig}, all the combinatoric background lifetime parameters and the partially reconstructed acceptance parameter n.

The results are summarised in Table 7.7. The projection plots and correlation matrix provide no additional information for the individual fits but can be found in appendix B.

The numbers of events processed for each dataset are identical to the individual fits, however the number of events categorised under each PDF are slightly changed and so are shown in Table 7.8. The SelA portion of the fit identifies 4504 events as signal

				Fit Result and Error	
PDF		Parameters	Usage	SelA	SelB
Signal	mass	$frac_{\sigma 1}^{sig}$	Fixed	0.93	
		$\sigma 1^{sig}$	Free	$18.67 \pm 0.31\,\mathrm{MeVc}^{-2}$	
		$ratio_{21}^{sig}$	Fixed	10.493	
		m_{B_s}	Free	$5358.5 \pm 0.3\,\mathrm{MeVc}^{-2}$	
	lifetime	$\mathbf{\Gamma_{FS}}$	Free	$\mathbf{0.668 \pm 0.017}\,\mathrm{ps}^{-1}$	
		t_0^{sig}	Fixed	$0.2\,\mathrm{ps}$	
		n^{sig}	Free	1.25 ± 0.13	
		b^{sig}	Free	$2.08 \pm 0.34\,\mathrm{ps}^{-1}$	
		c^{sig}	Fixed	$-0.0261\,\mathrm{ps}^{-1}$	
bkg^{comb}	mass	α_M^{comb}	Free	0.0008 ± 0.0002	0.0005 ± 0.0001
	lifetime	σ^{comb}	Free	$0.625 \pm 0.015\,\mathrm{ps}$	
		α^{comb}	Free	-1.669 ± 0.053	
		η^{comb}	Free	2.63 ± 0.15	
		t_0^{comb}	Fixed	$0.2\,\mathrm{ps}^{-1}$	
		b^{comb}	Free	$14 \pm 9.0\,\mathrm{ps}^{-1}$	
		Y^{comb}	Free	0.259 ± 0.062	
bkg^{PR}	mass	α_M^{PR}	Free	0.0101 ± 0.0004	0.0096 ± 0.0008
	lifetime	τ^{PR}	Fixed	$1.425\,\mathrm{ps}$	
		t_0^{PR}	Fixed	$0.2\,\mathrm{ps}$	
		n^{PR}	Free	2.19 ± 0.31	
		b^{PR}	Free	$2.23 \pm 0.19\,\mathrm{ps}^{-1}$	$3.09 \pm 0.39\,\mathrm{ps}^{-1}$
		c^{PR}	Fixed	$-0.0261\,\mathrm{ps}^{-1}$	
bkg^{B_d}	mass	$frac_{\sigma 1}^{B_d}$	Fixed	–	0.765
		$\sigma_1^{B_d}$	Fixed	–	$21.3\,\mathrm{MeVc}^{-2}$
		$\sigma_2^{B_d}$	Fixed	–	$77.2\,\mathrm{MeVc}^{-2}$
		$mean^{B_d}$	Fixed	–	$5321.1\,\mathrm{MeVc}^{-2}$
	lifetime	τ^{B_d}	Fixed	–	$1.519\,\mathrm{ps}$
		t_0^{mis-ID}	Fixed	–	$0.2\,\mathrm{ps}$
		n^{mis-ID}	Fixed	–	1.88
		b^{mis-ID}	Fixed	–	$1.71\,\mathrm{ps}^{-1}$
		c^{mis-ID}	Fixed	–	$-0.261\,\mathrm{ps}^{-1}$
bkg^{Λ_b}	mass	σ^{Λ_b}	Fixed	–	$51.2\,\mathrm{MeVc}^{-2}$
		α^{Λ_b}	Fixed	–	0.62
		η^{Λ_b}	Fixed	–	125
		$mean^{\Lambda_b}$	Fixed	–	$5430\,\mathrm{MeVc}^{-2}$
	lifetime	τ^{Λ_b}	Fixed	–	$1.425\,\mathrm{ps}$
		ϵ^{mis-ID}	–	–	––
PDF Fractions	Signal Events/Total Events		Free	0.367 ± 0.006	0.233 ± 0.006
	Comb bkg/Total bkg		Free	0.528 ± 0.016	0.563 ± 0.017
	PR bkg/Non-comb bkgs		Free	–	0.739 ± 0.034
	B_d bkg/Miss-ID bkg		Free	–	0.739 ± 0.050

TABLE 7.7: Fit results of the full simultaneous fit to SelA and SelB data.

	SelA		SelB	
PDF	Percentage	# Events	Percentage	# Events
Signal	36.7%	4504	23.3%	3632
Combinatoric Background	33.4%	4099	43.2%	6735
PR Background	29.9%	3669	24.8%	3866
B_d Background	–	–	6.5%	1013
Λ_b Background	–	–	2.3%	359

TABLE 7.8: The percentage of the simultaneous fit to SelA and SelB datasets allocated to each PDF and the corresponding number of events.

events ($\sim$ 50 less than the individual SelA fit) and 3632 SelB signal events ($\sim$ 200 more than the individual SelB fit) giving us 8136 signal events. The simultaneous fit to both dataset gives $\Gamma_{FS} = 0.668 \pm 0.017\,\mathrm{ps}^{-1}$. Γ_{FS} is highly correlated with the signal proper-time acceptance functions, $\rho_{\Gamma_{FS},b^{sig}} = -0.84$, $\rho_{\Gamma_{FS},n^{sig}} = -0.64$. It is evident that the simultaneous fit has substantially increased the precision on Γ_{FS} from those found by the individual fits.

7.4 A Constrained Fit With Information From $B_s \to J/\psi\phi$

Although the primary result for this analysis is the measurement of Γ_{FS} it is worth reminding the reader that LHCb has measured Γ_s and $\Delta\Gamma_s$ from $B_s \to J/\psi\phi$. The addition of the Γ_s, $\Delta\Gamma_s$ and $\rho_{\Gamma_s,\Delta\Gamma_s}$ as external constraints to the Γ_{FS} fit will reduce correlations and uncertainties on the fit values.

The simultaneous fit described in section 7.3.3 is repeated, this time measuring Γ_s as opposed to Γ_{FS}. As discussed in section 4.1.2 an external constraint from the $B_s \to J/\psi\phi$ is applied. The β_s analysis presents measurements [37]:

$$\begin{aligned} \Gamma_s &= 0.657 \pm 0.009 \pm 0.008\,\mathrm{ps}^{-1} \\ \Delta\Gamma_s &= 0.123 \pm 0.029 \pm 0.011\,\mathrm{ps}^{-1} \\ \rho_{\Gamma_s,\Delta\Gamma_s} &= -0.3 \end{aligned}$$

The simultaneous fit is repeated with an additional χ^2 constraint of the form:

$$\chi^2_{constraint} = \mathbf{D}^T \begin{pmatrix} \sigma^2_{stat}(\Gamma_s) + \sigma^2_{sys}(\Gamma_s) & \rho_{(\Gamma_s,\Delta\Gamma_s)} \times \sigma(\Gamma_s) \times \sigma(\Delta\Gamma_s) \\ \rho_{(\Gamma_s,\Delta\Gamma_s)} \times \sigma(\Gamma_s) \times \sigma(\Delta\Gamma_s) & \sigma^2_{stat}(\Delta\Gamma_s) + \sigma^2_{sys}(\Delta\Gamma_s) \end{pmatrix}^{-1} \mathbf{D} \tag{7.2}$$

where σ_{sys} and σ_{stat} refer respectively to the systematic and the statistical error of the proceeding parameter; σ is the total error of the parameter (statistical and systematic errors combined in quadrature); ρ is the correlation between the parameters; and $\mathbf{D}$ is a vector giving the difference between the fit and the constraint values:

$$\begin{pmatrix} \Gamma_{fit} - \Gamma_{constraint} \\ \Delta\Gamma_{fit} - \Delta\Gamma_{constraint} \end{pmatrix} \tag{7.3}$$

The shared parameters are those of the B^0_s signal mass distribution, the signal acceptance ϵ^{sig}, all the combinatoric background lifetime parameters, and the partially reconstructed acceptance parameter n. The signal lifetime model is fitted with a double exponential as now we can fit for $\Delta\Gamma_s$.

The fit results for the full $0 - 15\,\text{ps}$ fit to Γ_s are given in Table 7.9, with the projection plots of the SelA mass and time, and the SelB mass and time shown in Figures 7.18, 7.20, 7.19, 7.21 respectively. The correlation matrix can be found in appendix C.

By applying this constraint and performing a simultaneous fit to SelA and SelB datasets, we obtain:

$$\begin{aligned} \Gamma_s &= 0.666 \pm 0.010\,\text{ps}^{-1} \\ \Delta\Gamma_s &= 0.107 \pm 0.026\,\text{ps}^{-1} \\ \rho_{\Gamma_s,\Delta\Gamma_s} &= -0.11 \end{aligned}$$

Table 7.10 summarises the fractions of events identified as each PDF in the fits. The fractions are consistent with those seen in the first simultaneous fit. In total 8136 signal events are identified.

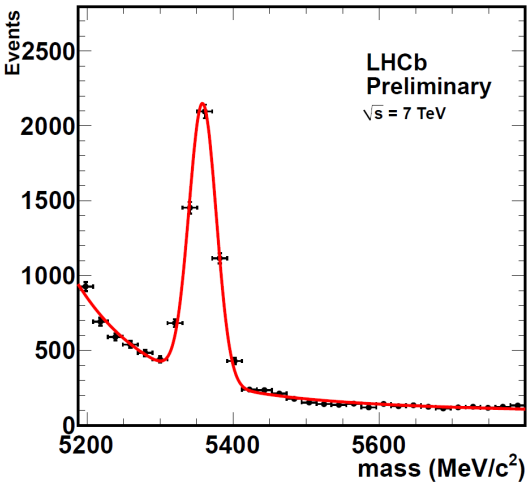

FIGURE 7.18: SelA mass projection of a full simultaneous fit to SelA and SelB data in the range $0-15$ ps with external constraints on Γ_s and $\Delta\Gamma_s$.

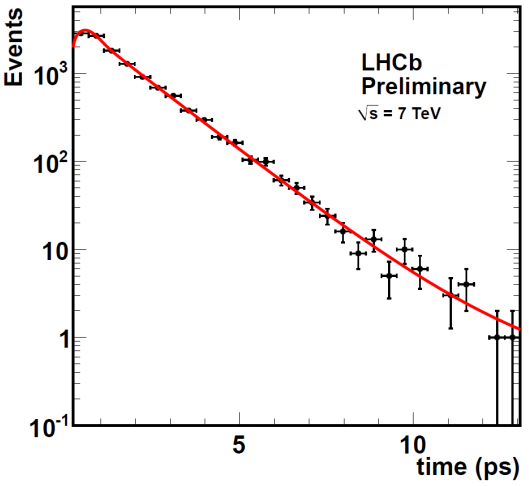

FIGURE 7.20: SelA time projection of a full simultaneous fit to SelA and SelB data in the range $0-15$ ps with external constraints on Γ_s and $\Delta\Gamma_s$.

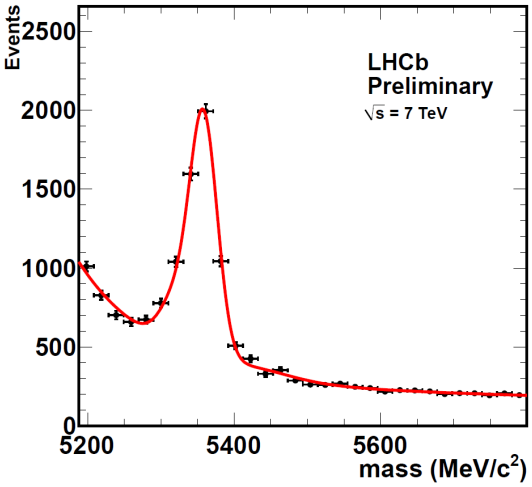

FIGURE 7.19: SelB mass projection of a full simultaneous fit to SelA and SelB data in the range $0-15$ ps with external constraints on Γ_s and $\Delta\Gamma_s$.

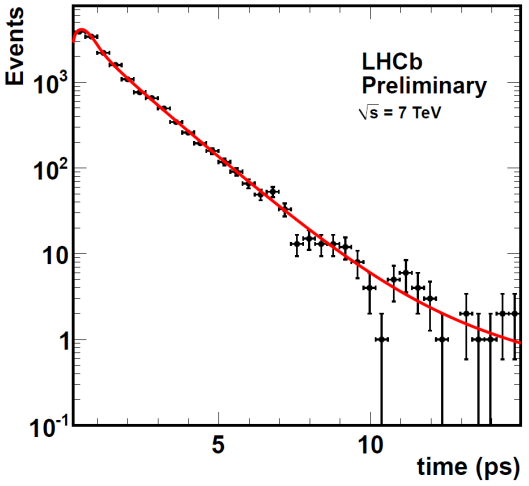

FIGURE 7.21: SelB time projection of a full simultaneous fit to SelA and SelB data in the range $0-15$ ps with external constraints on Γ_s and $\Delta\Gamma_s$.

				Fit Result and Error	
PDF		Parameters	Usage	SelA	SelB
Signal	mass	$frac_{\sigma 1}^{sig}$	Fixed	0.93	
		$\sigma 1^{sig}$	Free	$18.7 \pm 0.3\,\mathrm{MeVc^{-2}}$	
		$ratio_{21}^{sig}$	Fixed	10.493	
		m_{B_s}	Free	$5358.5 \pm 0.3\,\mathrm{MeVc^{-2}}$	
	lifetime	$\mathbf{\Gamma_s}$	Constrained	$\mathbf{0.666 \pm 0.010}\,\mathrm{ps^{-1}}$	
		$\Delta\Gamma_s$	Constrained	$0.107 \pm 0.026\,\mathrm{ps^{-1}}$	
		t_0^{sig}	Fixed	0.2 ps	
		n^{sig}	Free	1.32 ± 0.12	
		b^{sig}	Free	$2.26 \pm 0.25\,\mathrm{ps^{-1}}$	
		c^{sig}	Fixed	$-0.0261\,\mathrm{ps^{-1}}$	
bkg^{comb}	mass	α_M^{comb}	Free	0.0008 ± 0.0002	0.0005 ± 0.0001
	lifetime	σ^{comb}	Free	0.625 ± 0.014 ps	
		α^{comb}	Free	-1.666 ± 0.055	
		η^{comb}	Free	2.65 ± 0.16	
		t_0^{comb}	Fixed	0.2 ps	
		b^{comb}	Free	$15 \pm 10\,\mathrm{ps^{-1}}$	
		Y^{comb}	Free	0.259 ± 0.064	
bkg^{PR}	mass	α_M^{PR}	Free	0.0101 ± 0.0004	$.010 \pm 0.0008$
	lifetime	τ^{PR}	Fixed	1.425 ps	
		t_0^{PR}	Fixed	0.2 ps	
		n^{PR}	Free	2.19 ± 0.30	
		b^{PR}	Free	$2.22 \pm 0.20\,\mathrm{ps^{-1}}$	$3.10 \pm 0.41\,\mathrm{ps^{-1}}$
		c^{PR}	Fixed	$-0.0261\,\mathrm{ps^{-1}}$	
bkg^{B_d}	mass	$frac_{\sigma 1}^{B_d}$	Fixed	–	0.765
		$\sigma_1^{B_d}$	Fixed	–	$21.3\,\mathrm{MeVc^{-2}}$
		$\sigma_2^{B_d}$	Fixed	–	$77.2\,\mathrm{MeVc^{-2}}$
		$mean^{B_d}$	Fixed	–	$5321.1\,\mathrm{MeVc^{-2}}$
	lifetime	τ^{B_d}	Fixed	–	1.519 ps
		t_0^{mis-ID}	Fixed	–	0.2 ps
		n^{mis-ID}	Fixed	–	1.88
		b^{mis-ID}	Fixed	–	$1.71\,\mathrm{ps^{-1}}$
		c^{mis-ID}	Fixed	–	$-0.261\,\mathrm{ps^{-1}}$
bkg^{Λ_b}	mass	σ^{Λ_b}	Fixed	–	$51.2\,\mathrm{MeVc^{-2}}$
		α^{Λ_b}	Fixed	–	0.62
		η^{Λ_b}	Fixed	–	125
		$mean^{\Lambda_b}$	Fixed	–	$5430\,\mathrm{MeVc^{-2}}$
	lifetime	τ^{Λ_b}	Fixed	–	1.425 ps
		ϵ^{mis-ID}	–	–	––
PDF Fractions	Signal Events/Total Events		Free	0.367 ± 0.006	0.233 ± 0.006
	Comb bkg/Total bkg		Free	0.527 ± 0.017	0.562 ± 0.019
	PR bkg/Non-comb bkgs		Free	–	0.741 ± 0.036
	B_d bkg/Miss-ID bkg		Free	–	0.740 ± 0.051

TABLE 7.9: Fit results of the full simultaneous fit to SelA and SelB data with external constraints on Γ_s and $\Delta\Gamma_s$.

	SelA		SelB	
PDF	Percentage	# Events	Percentage	# Events
Signal	36.7%	4504	23.3%	3632
Combinatoric Background	33.4%	4099	43.1%	6718
PR Background	30.0%	3682	24.9%	3881
B_d Background	–	–	6.4%	998
Λ_b Background	–	–	2.3%	349

TABLE 7.10: The percentage of the simultaneous fit to SelA and SelB datasets allocated to each PDF and the corresponding number of events.

7.5 Summary of Results

Table 7.11 summarises the Γ_{FS} fit results found from $B_s^0 \to D_s^- \pi^+$ SelA and SelB datasets individually, as well as a simultaneous fit to both channels.

	$\Gamma_{FS}[\mathrm{ps}^{-1}]$
SelA	0.676 ± 0.023
SelB	0.658 ± 0.025
SelA and SelB	0.668 ± 0.017

TABLE 7.11: Summary of fit results of the full simultaneous fits for Γ_{FS}.

Table 7.12 summarises the Γ_s fit results from a simultaneous fit to SelA and SelB datasets, with a constraint on Γ_s and $\Delta\Gamma_s$ taken from the LHCb result from $B_s^0 \to J/\psi\phi$.

Γ_s	$= 0.666 \pm 0.010\,\mathrm{ps}^{-1}$
$\Delta\Gamma_s$	$= 0.107 \pm 0.026\,\mathrm{ps}^{-1}$
$\rho_{\Gamma_s,\Delta\Gamma_s}$	$= -0.11$

TABLE 7.12: Summary of fit results of the full simultaneous fits for Γ_s with external constraints on Γ_s and $\Delta\Gamma_s$.

Chapter 8

Systematic Uncertainties

This chapter discusses the systematic uncertainties in the measurement of Γ_{FS}.

8.1 Systematic Errors Associated with Signal

8.1.1 Sensitivity to Proper-Time Acceptance Parametrisation

The results presented in this thesis floated the acceptance parameters and performed a simultaneous fit to both the acceptance and the proper-time; therefore we do not assign any further systematic error. In this section we will simply perform cross checks of the parametrisation.

There are alternative options to compensate for the proper-time acceptance: the fit can be performed in the region where the acceptance is equal to 1; or the acceptance parameters can be fixed from MC data. If the fit is performed over a smaller proper-time range we negate the acceptance effects but we also lose a large amount of data.

This study fixes each acceptance parameter to those obtained in the full fit in SelA, SelB and the simultaneous fit; multiple fits are then performed on each data set with the lower proper-time boundary varied. The lower time cut is varied up to a value of

	$\Gamma_{FS}\,(\mathrm{ps}^{-1})$		
$t >$	SelA	SelB	Simultaneous Fit
0.0	0.676 ± 0.011	0.658 ± 0.014	0.668 ± 0.009
0.5	0.677 ± 0.012	0.657 ± 0.015	0.669 ± 0.009
1.0	0.678 ± 0.013	0.657 ± 0.016	0.670 ± 0.010
1.5	0.669 ± 0.015	0.664 ± 0.019	0.665 ± 0.012
2.0	0.664 ± 0.018	0.641 ± 0.022	0.654 ± 0.014
2.5	0.674 ± 0.021	0.655 ± 0.027	0.665 ± 0.017
3.0	0.680 ± 0.026	0.655 ± 0.032	0.666 ± 0.020

TABLE 8.1: The results for fits to Γ_{FS} in varying lower time ranges.

3 ps, as beyond this cut there is too little data to reliably fit for Γ_{FS}. The shape of the proper-time acceptance was shown in section 5.4.2. It can be seen that the 'turn-on' curve of the low proper-time acceptance plateaus at ~ 5 ps, and even then we have an acceptance on the upper proper-time region.

The results are summarised in Table 8.1 and shown graphically in Figure 8.1, which shows the fits on SelA, SelB and the simultaneous fit. We observe little fluctuation up to a cut of $t > 1$ ps as little data is removed. The fluctuations are more pronounced in subsequent result but are consistent across the range.

The upper proper-time acceptance bias (c) cannot be left free to fit in data as there is no information that lets it be fitted independently of Γ_{FS}. The value of of $c = -0.0261\,\mathrm{ps}^{-1}$ was determined from MC10 SelA and SelB data with the 2011 trigger and with the same stripping and selection as was applied to the data. To account for the systematic uncertainty of taking this value from MC the fits are repeated with $c = 0$, and the absolute difference in fit values are taken as a conservative systematic error.

The results of the fits are given in Table 8.2 with the corresponding time projection plot Figure 8.2. The systematic uncertainty relating to the choice in the value of c is taken to be $0.030\,\mathrm{ps}^{-1}$; this represents the largest contribution to the systematic uncertainty on the result.

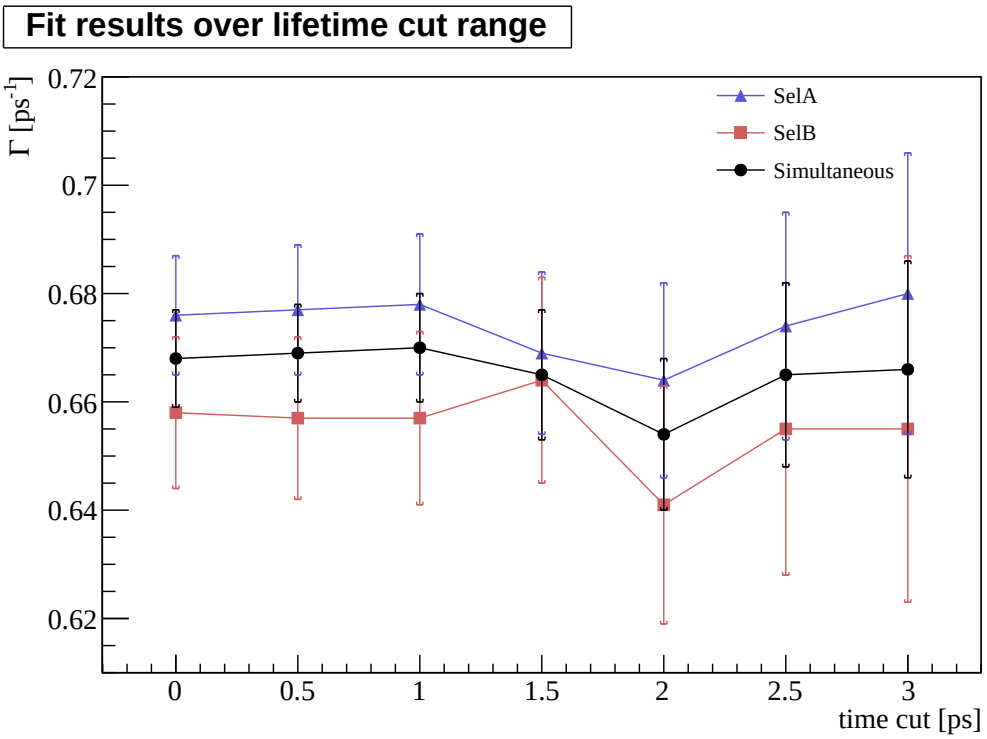

FIGURE 8.1: Fits for Γ_{FS} performed at different lower time cuts on SelA data (red triangles), SelB data (blue squares) and simultaneous fits (black circles)

	Γ_{FS} (ps^{-1})	
c	SelA	SelB
-0.0261	0.676 ± 0.023	0.658 ± 0.025
0	0.706 ± 0.025	0.687 ± 0.027
Δ	0.030	0.029

TABLE 8.2: A comparison of fit results for Γ_{FS} with c^{sig} fixed to $-0.0261\,\mathrm{ps}^{-1}$ and $0\,\mathrm{ps}^{-1}$

8.1.2 Sensitivity to Proper-Time Resolution

The proper-time resolution at LHCb is $\sim 50\,\mathrm{fs}$ for all channels. In this case a Gaussian fit to the proper-time residual gives $\sigma = 38\,\mathrm{fs}$. Refitting both with and without proper-time resolution gives results summarised in Table 8.3; it is evident that the the fit value and uncertainty for Γ_{FS} are entirely insensitive to the resolution and will not contribute towards a systematic uncertainty.

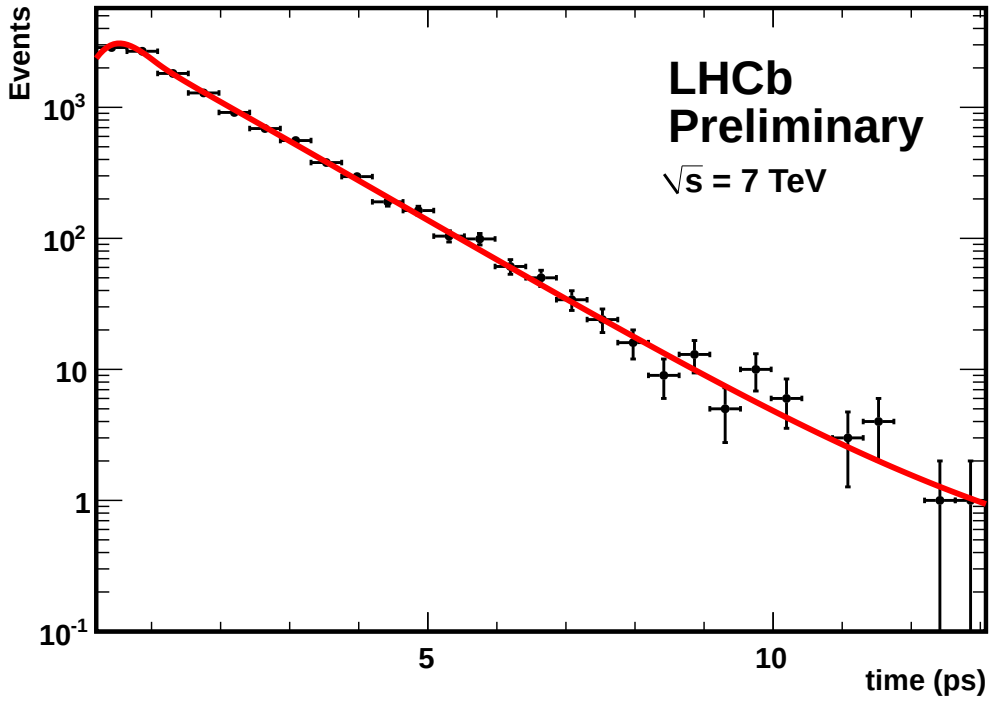

FIGURE 8.2: Time projection of Γ_{FS} fit to SelA data with $c = 0\,\mathrm{ps}^{-1}$.

	$\Gamma_{FS}\,(\mathrm{ps}^{-1})$	
	SelA	SelB
without PT resolution	0.676 ± 0.023	0.658 ± 0.025
with PT resolution	0.676 ± 0.023	0.658 ± 0.025
Δ	0.000	0.000

TABLE 8.3: A comparison of the fit results obtained in a fit for Γ_{FS} in both datasets with signal PT resolution toggled.

8.1.3 Signal Mass Model

The B_s^0 signal mass distribution has been modelled by a double Gaussian function for the fit results. We have observed in section 6.2.1 that the double Gaussian function does not provide an optimal fit to the data. We have tried using triple Gaussian and double Crystal Ball functions to fit the data but in both cases it proved difficult to get the fit to converge and behave well. A systematic study has been performed using

these alternative mass models but additional fit parameters have had to be constrained in order to obtain the fits.

Figures 8.3 and 8.4 show a double Gaussian fit to MC signal, and the subsequent mass projection of a full fit to SelB data using this model. An analogous set of figures can be seen for a triple Gaussian signal mass model (Figures 8.5 and 8.6), and a double Crystal Ball mass model (Figures 8.7 and 8.8).

The results of fits performed with these models can be seen in Table 8.4. It is evident that although the triple Gaussian or the double Crystal Ball functions would have fitted the signal distribution better, the choice of model has little effect on the final fit result. We take a systematic uncertainty of $0.001\,\mathrm{ps}^{-1}$ from the largest variation.

B_S^0 mass model	$\Gamma_{FS}\,(\mathrm{ps}^{-1})$
Double Gaussian	0.658 ± 0.025
Double Crystal Ball	0.659 ± 0.024
Triple Gaussian	0.658 ± 0.024
Max Δ	0.001

TABLE 8.4: A comparison of the fit results obtained in a fit for Γ_{FS} in which the B_s^0 mass model is described by a double Crystal Ball and by a triple Gaussian.

8.1.4 Other Possible Signal Systematics

8.1.4.1 Z-scaling, Momentum Scaling, and Offset

The alignment and the magnetic field calibration are not yet optimal at LHCb. The z and the momentum scale of the experiment are both known to about 0.01%. This is negligible and so no systematic error is assigned.

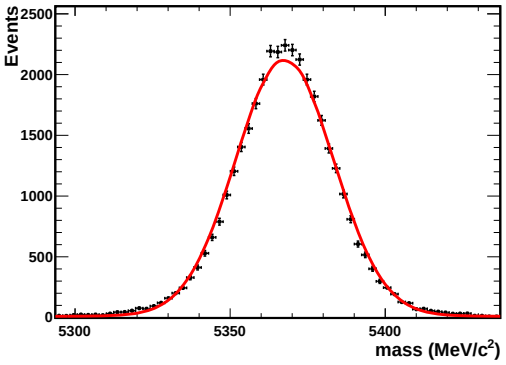

FIGURE 8.3: MC10 signal data fitted with a double Gaussian function.

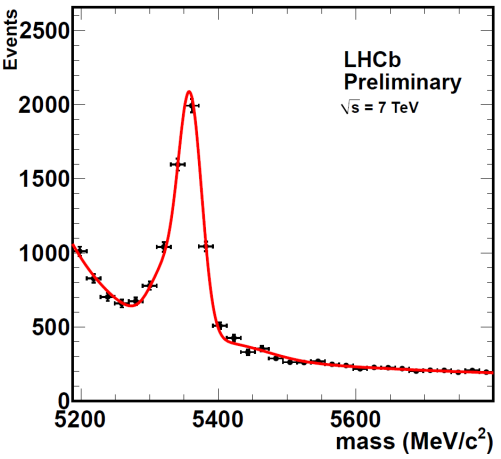

FIGURE 8.4: SelB mass projection of a fit using a double Gaussian signal mass model.

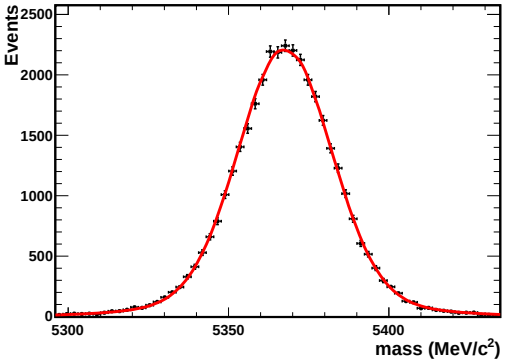

FIGURE 8.5: MC10 signal data fitted with a triple Gaussian function.

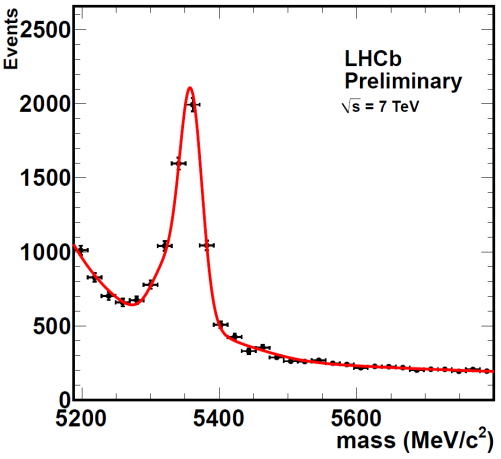

FIGURE 8.6: SelB mass projection of a fit using a triple Gaussian signal mass model.

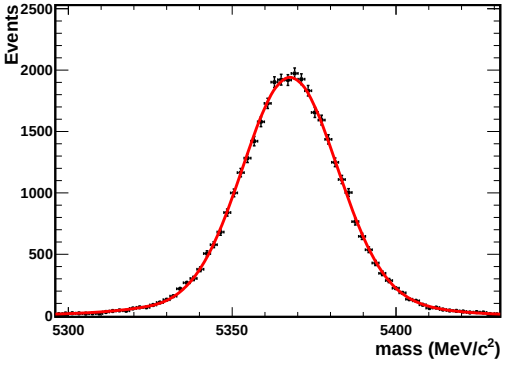

FIGURE 8.7: MC10 signal data fitted with a double Crystal Ball function.

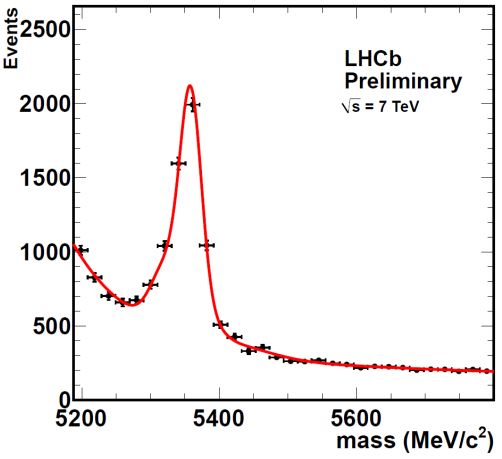

FIGURE 8.8: SelB mass projection of a fit using a double Crystal Ball signal mass model.

8.2 Systematic Errors Associated with Background

8.2.1 Sensitivity to PR Background Model

The full fit saw the PR acceptance parameters b and n floated, so no additional uncertainty will be applied. The of the PR background, τ_{PR}, was fixed to 1.425 ps and the upper proper-time acceptance bias fixed to $-0.0261\,\mathrm{ps}^{-1}$. These parameters cannot be separated so the systematic study repeats the fits with $c = 0\,\mathrm{ps}^{-1}$ and takes the absolute difference as the systematic uncertainty.

The results shown in Table 8.5 give the fit value of Γ_{FS} is obtained by varying the fixed value of c. The fit to Γ_{FS} is insensitive to the PR lifetime so will not contribute a systematic uncertainty.

	$\Gamma_{FS}\,(\mathrm{ps}^{-1})$	
c	SelA	SelB
-0.0261	0.676 ± 0.023	0.658 ± 0.025
0	0.676 ± 0.023	0.658 ± 0.025
Δ	0.0	0.0

TABLE 8.5: A comparison of fit results for Γ_{FS} with c^{PR} fixed to $-0.0261\,\mathrm{ps}^{-1}$ and $0\,\mathrm{ps}^{-1}$

In the fits for Γ_{FS} the PR background mass distribution was modelled as a single exponential with the exponent floated so there is not a systematic uncertainty associated with the mass exponent.

8.2.2 Sensitivity to the Mis-ID Background Model

The acceptance function for the Mis-ID background is somewhat ambiguous. The acceptance cannot be floated in the fit as both these backgrounds are under the signal peak, so the acceptance was taken from a limited amount of MC. For a systematic study the fit is repeated with with ϵ^{mis-ID} fixed to the fitted ϵ^{sig} values; this is obviously a circular argument so could not be implemented for the full fit, but is sufficient to gauge

the systematic uncertainty. The parameters used and the values of Γ_{FS} obtained are given in Table 8.6.

	$b\,(\mathrm{ps}^{-1})$	n	$\Gamma_{FS}\,(\mathrm{ps}^{-1})$
$\epsilon^{Mis-ID}(\mathrm{MC})$	1.71 ± 0.43	1.88 ± 0.33	0.658 ± 0.025
$\epsilon^{Mis-ID}(\epsilon^{sig})$	1.79 ± 0.44	1.15 ± 0.15	0.660 ± 0.024
Δ			0.002

TABLE 8.6: A comparison of fit results for Γ_{FS} with ϵ^{Mis-ID} taken from MC and from ϵ^{sig}

The lifetimes of the mis-ID background were fixed to their PDG values $\tau_{B_d} = 1.519\,\mathrm{ps}$ $\tau_{\Lambda_b} = 1.425\,\mathrm{ps}$ with the upper proper-time acceptance bias fixed to $-0.026\,\mathrm{ps}^{-1}$. The lifetimes and the upper acceptance cannot be separated from each other so the systematic study repeats the fits with $c = 0\,\mathrm{ps}^{-1}$ and takes the absolute difference as the systematic uncertainty.

The results shown in Table 8.7 give the fit value of Γ_{FS} obtained by varying the fixed value of c^{mis-ID}. It can be seen that the fit to Γ_{FS} is sensitive to the mis-ID lifetime so we take 0.007 as the contribution to the total systematic uncertainty.

	$\Gamma_{FS}\ (ps^{-1})$
-0.0261	0.658 ± 0.025
0	0.665 ± 0.025
Δ	0.007

TABLE 8.7: A comparison of fit results for Γ_{FS} with c^{PR} fixed to $-0.0261\,\mathrm{ps}^{-1}$ and $0\,\mathrm{ps}^{-1}$

The mis-ID background consists of B_d and Λ_b contributions. In the fit for Γ_{FS} all parameters defining these backgrounds were fixed to MC values. The mean of each mass distribution was fixed to $m_{MC} - 7.4\,\mathrm{MeVc}^{-2}$ to account for the shift in mass observed between MC and data. The systematic study is performed by repeating the fits and varying the mean of each background by $\pm 5\,\mathrm{MeVc}^{-2}$. The results of shifting the B_d central mass can be seen in Table 8.8. The equivalent results for the Λ_b background can be seen in Table 8.9; the Λ_b mass shift has no effect on the fit of Γ_{FS}.

mean	$\Gamma_{FS}\,(\mathrm{ps}^{-1})$
$-5MeV$	0.658 ± 0.026
0	0.658 ± 0.025
$+5MeV$	0.657 ± 0.025
Max Δ	0.001

TABLE 8.8: A comparison of fit results for Γ_{FS} with the mean mass of the B_d peak shifted

mean	$\Gamma_{FS}\,(\mathrm{ps}^{-1})$
$-5MeV$	0.658 ± 0.025
0	0.658 ± 0.025
$+5MeV$	0.658 ± 0.029
Δ	0.0

TABLE 8.9: A comparison of fit results for Γ_{FS} with the mean mass of the Λ_b peak shifted

8.2.3 Sensitivity to Combinatoric Background Model

In the fits to data all parameters pertaining to the combinatoric background are floated. No systematic error will therefore be assigned to the mass exponential fit. The lifetime model was developed in ansatz to the data, so in this section we compare the Crystal Ball model used with that of a double exponential.

Figures 8.9 and 8.10 show a Crystal Ball fit to the lifetime distribution in the B_s^0 lower mass side-band (i.e. the combinatoric background) and the subsequent mass projection of a full fit to SelB data using this model. An analogous set of figures can be seen for a double exponential lifetime model (Figures 8.11 and 8.12).

The results of the fits can be seen in Table 8.10. A slight difference is observed in the fit result for Γ_{FS} so we take 0.002 to be the contributing systematic uncertainty from the lifetime model.

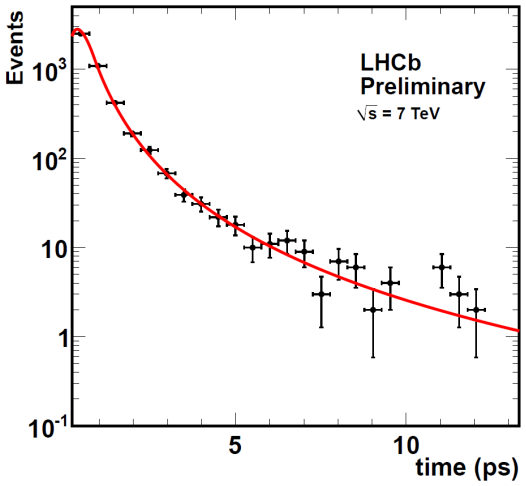

FIGURE 8.9: B_s^0 upper mass side-band fitted with a Crystal Ball function.

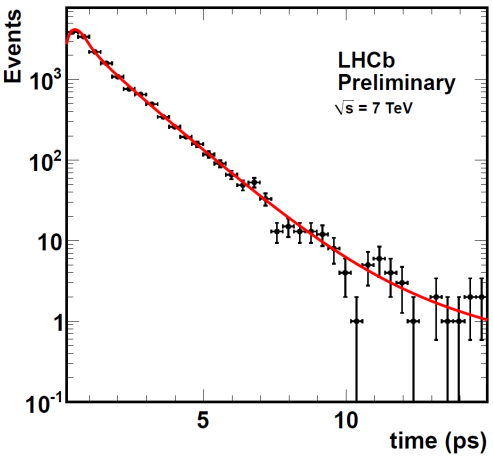

FIGURE 8.10: SelB mass projection of a fit using a Crystal Ball combinatoric mass model.

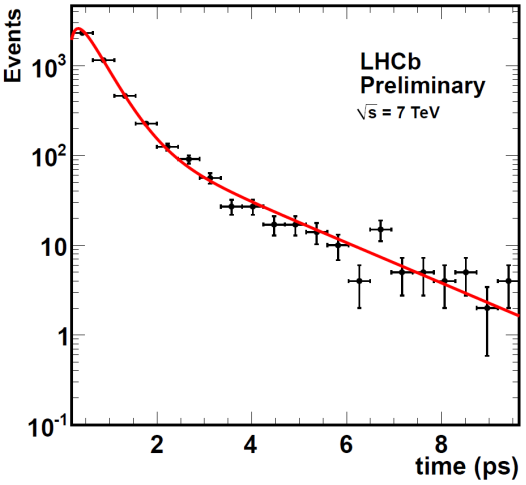

FIGURE 8.11: B_s^0 upper mass side-band fitted with a double exponential function.

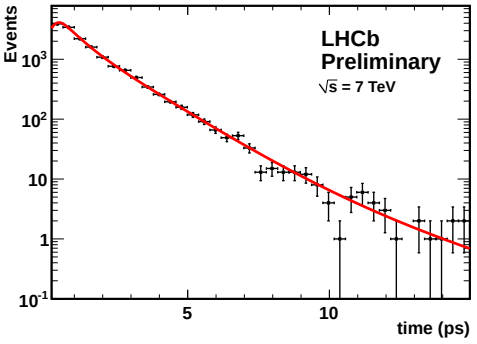

FIGURE 8.12: SelB mass projection of a fit using a double exponential combinatoric mass model.

	Γ_{FS} (ps^{-1})	
B_S^0 mass model	SelA	SelB
Crystal Ball	0.676 ± 0.023	0.658 ± 0.025
Double exponential	0.677 ± 0.023	0.656 ± 0.025
Max Δ	0.001	0.002

TABLE 8.10: A comparison of the fit results obtained in a fit for Γ_{FS} in which the combinatoric background time distribution is described by a Crystal Ball and by a double exponential model

8.3 Summary of Systematic Errors

The systematic errors assigned are shown in Table 8.11. The total systematic uncertainty of the measurement is taken to be the sum in quadrature. The uncertainty is dominated by the upper proper-time acceptance parameter c, which was fixed from a MC study.

	Systematic error assigned
Signal	
Upper proper time acceptance	± 0.030
B_s^0 Mass model	± 0.001
Background	
Mis-ID acceptance parameters	± 0.002
Mis-ID mass models	± 0.001
Mis-ID lifetime	± 0.007
Combinatoric lifetime	± 0.002
Total	
	± 0.0309

TABLE 8.11: A summary of the systematic errors analysed in this chapter.

Chapter 9

Conclusion

This study was dedicated to the analysis of the flavour specific decay: $B_s^0 \to D_s^- \pi^+$. The analysis was performed over LHCb 2011 data available up until the 7^{th} July 2011. This corresponds to an integrated luminosity of $340\,\mathrm{pb}^{-1}$.

The lifetime distribution of $B_s^0 \to D_s^- \pi^+$ is the sum of two exponentials. This class of channel gives a poor constraint on $\Delta\Gamma$, so we fit a single exponential to the distribution and hence measure the effective decay width Γ_{FS}. The distribution is heavily modified by a proper-time acceptance bias.

The dataset was divided into two exclusive selections based on the decay of the D_s: decays via a ϕ resonance $B_s^0 \to D_s^-((\phi \to K^-K^+)\pi^-)\pi^+$, and decays via a $K^*(892)$ resonance $B_s^0 \to D_s^-((K^-K^*(892)^0 \to K^+\pi^-))\pi^+$.

The $B_s^0 \to D_s^-((\phi \to K^-K^+)\pi^-)\pi^+$ dataset's only significant background contribution arises from combinatorial background, and the modelling of this is determined entirely by the data. From this channel we obtain:

$$\Gamma_{FS} = 0.676 \pm 0.023 \pm 0.030\,\mathrm{ps}^{-1}$$

The $B_s^0 \to D_s^-((K^-K^*(892)^0 \to K^+\pi^-))\pi^+$ dataset has a larger contribution from combinatoric and mis-identified background but provides an alternative measurement of:

$$\Gamma_{FS} = 0.658 \pm 0.025 \pm 0.031\,\text{ps}^{-1}$$

A simultaneous fit for Γ_{FS} was performed to both the datasets leading to a value of:

$$\Gamma_{FS} = 0.668 \pm 0.017 \pm 0.031\,\text{ps}^{-1}$$

The statistical uncertainty is dominated by the lower proper-time acceptance which is highly correlated with Γ_{FS}. The systematic uncertainty is dominated by the upper proper-time acceptance which was fixed in a Monte Carlo analysis.

This value, although somewhat higher, is consistent with the prediction of $\Gamma_{FS} = 0.613 \pm 0.009 \pm 0.008\,\text{ps}^{-1}$ from the LHCb $B_s^0 \to J/\psi\phi$ measurements of Γ_s and $\Delta\Gamma_s$.

Applying a constraint from $B_s^0 \to J/\psi\phi$ allows us to fit for Γ_s. A simultaneous fit to both the datasets yields:

$$\Gamma_s = 0.666 \pm 0.010 \pm 0.031\,\text{ps}^{-1}$$

Appendix A

Background Mother ID Tables

The full Mother ID tables for the $B_s^0 \to D_s X$ MC sample. Table A.1 gives the Mother IDs and percentages of the D_s's, 0 represents a prompt particle with no mother. Table A.2 gives the Mother IDs and percentages of the bachelor.

TABLE A.1: $B_s \to D_s X$ Mother ID of the 'D_s', particle codes found in [1]. M:Mother, GM:Grandmother, GGM:Grandgrandmother

M ID	%	GM ID	%	GGM ID	%
0	$4.94 \pm 0.18\%$	0	$100 \pm 0\%$	0	$100 \pm 0\%$
433	$52.13 \pm 0.41\%$	531	$95.26 \pm 0.24\%$	0	$11.96 \pm 0.38\%$
				533	$39.00 \pm 0.57\%$
		20433	$4.74 \pm 0.24\%$	531	$49.0 \pm 2.6\%$
511	$0.0135 \pm 0.0095\%$	513	$100 \pm 0\%$		

Continued on next page

M ID	%	GM ID	%	GGM ID	%
				0	$50 \pm 35\%$
513	$0.0067 \pm 0.0067\%$				
		0	$100 \pm 0\%$		
				0	$100 \pm 0\%$
521	$0.0067 \pm 0.0067\%$				
		0	$100 \pm 0\%$		
				0	$100 \pm 0\%$
523	$0.0067 \pm 0.0067\%$				
		0	$100 \pm 0\%$		
				0	$100 \pm 0\%$
531	$42.23 \pm 0.41\%$				
		0	$24.60 \pm 0.54\%$		
				0	$100 \pm 0\%$
		533	$75.37 \pm 0.54\%$		
				0	$48.63 \pm 0.72\%$
				541	$0.021 \pm 0.021\%$
		541	$0.032 \pm 0.023\%$		
				543	$100 \pm 0\%$
533	$0.027 \pm 0.013\%$				
		0	$100 \pm 0\%$		
				0	$100 \pm 0\%$
5122	$0.0067 \pm 0.0067\%$				
		0	$100 \pm 0\%$		
				0	$100 \pm 0\%$
20433	$0.633 \pm 0.065\%$				
		531	$100 \pm 0\%$		
				0	$11.7 \pm 3.3\%$
				533	$38.3 \pm 5.0\%$

TABLE A.2: $B_s \rightarrow D_s X$ Mother ID of the 'bachelor', particle codes found in [1], 0 represents a prompt particle with no mother. M:Mother, GM:Grandmother, GGM:Grandgrandmother

M ID	%	GM ID	%	GGM ID	%
0	$2.12 \pm 0.12\%$				
		0	$100 \pm 0\%$		
				0	$100 \pm 0\%$
15	$0.0067 \pm 0.0067\%$				
		511	$100 \pm 0\%$		
22	$0.040 \pm 0.016\%$				
		111	$100 \pm 0\%$		
				213	$100 \pm 0\%$
113	$1.75 \pm 0.11\%$				
		0	$2.7 \pm 1.0\%$		
				0	$100 \pm 0\%$
		331	$0.38 \pm 0.38\%$		
				431	$100 \pm 0\%$
		511	$0.38 \pm 0.38\%$		
		521	$0.38 \pm 0.38\%$		
		531	$2.30 \pm 0.93\%$		
				533	$50 \pm 20\%$
		20213	$93.8 \pm 1.5\%$		
				531	$53.3 \pm 3.2\%$
211	$0.115 \pm 0.028\%$				
		213	$41 \pm 12\%$		
				531	$71 \pm 17\%$
		531	$59 \pm 12\%$		
				0	$10 \pm 9.5\%$
				533	$40 \pm 15\%$

Continued on next page

M ID	%	GM ID	%	GGM ID	%
213	$49.48 \pm 0.41\%$				
		0	$0.095 \pm 0.036\%$		
				0	$100 \pm 0\%$
		215	$0.014 \pm 0.014\%$		
				0	$100 \pm 0\%$
		431	$0.014 \pm 0.014\%$		
				433	$100 \pm 0\%$
		511	$0.041 \pm 0.024\%$		
				513	$33 \pm 27\%$
		521	$0.027 \pm 0.019\%$		
		531	$95.46 \pm 0.24\%$		
				0	$12.74 \pm 0.40\%$
				533	$37.58 \pm 0.58\%$
				541	$0.029 \pm 0.020\%$
		20213	$4.34 \pm 0.24\%$		
				531	$51.4 \pm 2.8\%$
221	$0.0067 \pm 0.0067\%$				
		0	$100 \pm 0\%$		
				0	$100 \pm 0\%$
223	$0.027 \pm 0.013\%$				
		331	$25 \pm 22\%$		
				431	$100 \pm 0\%$
		511	$25 \pm 22\%$		
				535	$100 \pm 0\%$
		521	$50 \pm 25\%$		
				523	$50 \pm 35\%$
310	$0.0135 \pm 0.0095\%$				
		311	$50 \pm 35\%$		

Continued on next page

M ID	%	GM ID	%	GGM ID	%
		411	$50 \pm 35\%$		
313	$0.020 \pm 0.012\%$				
		421	$67 \pm 27\%$		
				413	$50 \pm 35\%$
				511	$50 \pm 35\%$
		431	$33 \pm 27\%$		
323	$0.182 \pm 0.035\%$				
		531	$100 \pm 0\%$		
				0	$14.8 \pm 6.8\%$
				533	$22.2 \pm 8.0\%$
333	$0.0067 \pm 0.0067\%$				
		431	$100 \pm 0\%$		
411	$0.027 \pm 0.013\%$				
		413	$50 \pm 25\%$		
				521	$50 \pm 35\%$
		511	$25 \pm 22\%$		
				513	$100 \pm 0\%$
		531	$25 \pm 22\%$		
421	$0.101 \pm 0.026\%$				
		413	$27 \pm 11\%$		
				511	$25 \pm 22\%$
		423	$53 \pm 13\%$		
				0	$12.5 \pm 12\%$
				521	$25 \pm 15\%$
		425	$6.7 \pm 6.4\%$		
				511	$100 \pm 0\%$
		511	$6.7 \pm 6.4\%$		
				535	$100 \pm 0\%$

Continued on next page

M ID	%	GM ID	%	GGM ID	%
		521	$6.7 \pm 6.4\%$		
431	$0.040 \pm 0.016\%$				
		433	$50 \pm 20\%$		
				531	$33 \pm 27\%$
		511	$17 \pm 15\%$		
		531	$33 \pm 19\%$		
				533	$50 \pm 35\%$
511	$0.027 \pm 0.013\%$				
		0	$25 \pm 22\%$		
				0	$100 \pm 0\%$
		513	$75 \pm 22\%$		
				0	$67 \pm 27\%$
521	$0.047 \pm 0.018\%$				
		0	$57 \pm 19\%$		
				0	$100 \pm 0\%$
		523	$43 \pm 19\%$		
				0	$67 \pm 27\%$
531	$45.89 \pm 0.41\%$				
		0	$24.75 \pm 0.52\%$		
				0	$100 \pm 0\%$
		533	$75.23 \pm 0.52\%$		
				0	$50.75 \pm 0.70\%$
				541	$0.039 \pm 0.028\%$
		541	$0.015 \pm 0.015\%$		
2214	$0.0067 \pm 0.0067\%$				
		521	$100 \pm 0\%$		
				523	$100 \pm 0\%$
3112	$0.0067 \pm 0.0067\%$				

Continued on next page

M ID	%	GM ID	%	GGM ID	%
		0	$100 \pm 0\%$		
				0	$100 \pm 0\%$
4122	$0.0067 \pm 0.0067\%$				
		4212	$100 \pm 0\%$		
5122	$0.020 \pm 0.012\%$				
		0	$67 \pm 27\%$		
				0	$100 \pm 0\%$
		5224	$33 \pm 27\%$		
10411	$0.0067 \pm 0.0067\%$				
		511	$100 \pm 0\%$		
20213	$0.054 \pm 0.019\%$				
		531	$100 \pm 0\%$		
				533	$50 \pm 18\%$
20223	$0.0067 \pm 0.0067\%$				
		0	$100 \pm 0\%$		
				0	$100 \pm 0\%$

Appendix B

Correlation Matrices

This appendix gives the full correlation matrices relating to the fits in section 7.

- Table B.1 gives the correlation matrix from the SelA fit to Γ_{FS}.
- Table B.2 gives the correlation matrix from the SelB fit to Γ_{FS}.
- Table B.3 gives the correlation matrix from the simultaneous fit (SelA and SelB datasets) to Γ_{FS}.
- Table B.4 gives the correlation matrix from the simultaneous fit (SelA and SelB datasets) to Γ_s with the constraint applied from the $B_s^0 \to J/\psi\phi$ information.

	$\sigma 1^{sig}$	m_{B_s}	Γ	b^{sig}	n^{sig}	α_M^{comb}	σ^{comb}	α^{comb}	η^{comb}	b^{comb}	γ^{comb}	α_M^{PR}	b^{PR}	n^{PR}	Frac1	Frac1
$\sigma 1^{sig}$	1	-0.084	0.0002	0.015	-0.0063	-0.033	0.05	0.066	0.033	0.001	0.018	0.29	0.012	-0.029	0.13	0.41
m_{B_s}		1	0.0031	0.00056	-0.0015	-0.016	-0.012	-0.021	-0.013	-0.0023	0.0056	-0.027	0.01	-0.01	-0.052	-0.071
Γ			1	**-0.85**	**-0.62**	-0.046	0.052	-0.092	-0.13	0.034	0.0018	0.00086	0.034	-0.032	-0.034	0.032
b^{sig}				1	**0.83**	0.012	-0.068	0.088	0.097	-0.042	0.019	-0.00013	-0.072	-0.042	0.0085	-0.0078
n^{sig}					1	0.14	-0.091	0.082	0.063	-0.05	-0.032	0.047	-0.13	-0.014	0.12	-0.091
α_M^{comb}						1	0.038	0.16	0.039	0.019	-0.28	0.29	**-0.52**	0.48	**0.75**	-0.11
σ^{comb}							1	-0.4	-0.18	-0.18	0.25	0.23	-0.19	-0.4	0.15	0.074
α^{comb}								1	**0.77**	0.05	-0.12	0.34	0.073	0.21	0.3	0.083
η^{comb}									1	0.031	-0.035	0.13	0.0016	0.0022	0.1	0.039
b^{comb}										1	0.34	0.021	-0.064	-0.048	0.026	0.0075
γ^{comb}											1	-0.079	0.16	-0.3	-0.25	0.047
α_M^{PR}												1	-0.23	0.074	**0.66**	0.36
b^{PR}													1	0.051	**-0.52**	0.038
n^{PR}														1	0.4	-0.065
Frac1															1	0.11
Frac1																1

TABLE B.1: Correlation table of free parameters in the full fit to SelA data with signal proper-time acceptance parameters free. Frac1 refers to the fraction of signal events to the total number of events. Frac2 refers the fraction of combinatoric background events to the total number of background events.

	$\sigma 1^{sig}$	m_{B_s}	Γ	b^{sig}	n^{sig}	α_M^{comb}	σ^{comb}	α^{comb}	η^{comb}	b^{comb}	Y^{comb}	α_M^{PR}	b^{PR}	n^{PR}	Frac4	Frac3	Frac2	Frac1
$\sigma 1^{sig}$	1	-0.42	0.038	-0.00021	-0.049	-0.11	-0.092	-0.1	-0.096	-0.072	0.014	-0.14	-0.062	0.019	0.09	0.34	0.0075	**0.61**
m_{B_s}		1	-0.027	0.025	0.053	0.12	0.12	0.14	0.12	0.085	-0.0015	0.25	0.076	0.00015	-0.23	-0.39	-0.081	-0.41
Γ			1	**-0.8**	**-0.61**	-0.23	-0.32	-0.33	-0.36	-0.32	-0.12	-0.13	-0.12	0.082	0.014	0.12	0.2	0.058
b^{sig}				1	**0.7**	0.095	0.23	0.24	0.24	0.24	0.15	0.086	0.066	-0.017	0.012	-0.086	-0.082	0.019
n^{sig}					1	0.27	0.28	0.31	0.31	0.32	0.1	0.17	0.18	-0.039	-0.0038	-0.17	-0.25	-0.11
α_M^{comb}						1	**0.57**	**0.64**	**0.65**	0.48	-0.083	0.5	**0.68**	-0.23	-0.055	-0.49	**-0.83**	-0.15
σ^{comb}							1	**0.82**	**0.86**	**0.87**	0.35	0.47	0.26	-0.11	-0.035	-0.42	**-0.58**	-0.088
α^{comb}								1	**0.95**	**0.81**	0.2	**0.52**	0.3	-0.19	-0.039	-0.46	**-0.65**	-0.1
η^{comb}									1	**0.82**	0.21	0.47	0.34	-0.16	-0.037	-0.43	**-0.62**	-0.1
b^{comb}										1	0.18	0.32	0.18	-0.28	-0.044	-0.29	-0.44	-0.087
Y^{comb}											1	-0.024	-0.25	0.032	-0.014	0.046	0.1	0.026
α_M^{PR}												1	0.41	0.0021	0.35	**-0.89**	**-0.69**	-0.063
b^{PR}													1	-0.021	-0.013	-0.41	**-0.71**	-0.076
n^{PR}														1	0.05	0.037	0.18	0.042
Frac4															1	-0.31	-0.015	0.14
Frac3																1	**0.59**	0.3
Frac2																	1	-0.0049
Frac1																		1

TABLE B.2: Correlation table of free parameters in the full fit to SelB data with signal proper-time acceptance parameters free. Frac1 refers to the fraction of signal events to the total number of events. Frac2 refers the fraction of combinatoric background events to the total number of background events. Frac3 refers the fraction of PR background events to the total number of non-combinatoric background events. Frac4 refers to the fraction of B_d events to mis-ID events

	$\sigma 1^{sig}$	m_{B_s}	Γ	b^{sig}	n^{sig}	$A.\alpha_M^{comb}$	σ^{comb}	α^{comb}	η^{comb}	b^{comb}	Y^{comb}	$A.\alpha_M^{PR}$	$A.b^{PR}$	n^{PR}	A.Frac2	A.Frac1	$B.\alpha_M^{comb}$	$B.\alpha_M^{PR}$	$B.b^{PR}$	B.Frac4	B.Frac3	B.Frac2	B.Frac1
$\sigma 1^{sig}$	1	-0.21	0.0024	0.019	-0.0059	-0.065	0.027	0.017	0.013	0.0093	-0.023	0.24	0.03	0.03	0.086	0.36	-0.016	0.0066	0.0026	0.035	0.15	0.068	0.37
m_{B_s}		1	0.0068	0.00051	0.0034	0.019	0.0099	0.022	0.0087	-0.0041	0.0046	-0.019	-0.0057	0.0079	-0.022	-0.099	0.0066	0.074	-0.0002	-0.13	-0.18	-0.0074	-0.22
Γ			1	**-0.84**	**-0.62**	-0.031	-0.015	-0.069	-0.13	-0.093	-0.0054	0.0093	0.023	0.019	-0.02	0.034	0.0042	0.023	-0.0077	0.0045	-0.02	0.018	0.013
b^{sig}				1	**0.8**	-0.002	0.019	0.067	0.093	0.12	-0.015	-0.0097	-0.046	0.046	-0.0078	-0.0072	-0.043	-0.0053	0.017	0.012	0.0043	-0.037	0.022
n^{sig}					1	0.12	-0.013	0.07	0.068	0.12	0.044	0.038	-0.1	0.024	0.11	-0.083	0.053	0.017	-0.03	0.0069	-0.013	0.045	-0.049
$A.\alpha_M^{comb}$						1	-0.039	0.16	0.084	-0.09	0.17	0.15	**-0.54**	-0.32	**0.67**	-0.13	0.23	0.16	-0.15	0.041	-0.15	0.26	-0.047
σ^{comb}							1	-0.31	-0.13	**0.51**	-0.13	0.14	0.00034	0.31	0.045	0.047	-0.024	0.17	0.11	0.057	-0.12	0.087	0.039
α^{comb}								1	**0.8**	-0.14	0.11	0.27	0.005	-0.16	0.29	0.036	0.21	0.38	-0.1	0.13	-0.31	0.38	0.033
η^{comb}									1	-0.069	0.053	0.16	-0.026	-0.015	0.16	0.022	0.13	0.22	-0.077	0.077	-0.18	0.23	0.021
b^{comb}										1	0.39	-0.055	0.17	-0.094	-0.11	-0.0019	-0.18	-0.13	0.23	-0.051	0.12	-0.2	-0.0017
Y^{comb}											1	0.04	-0.082	-0.27	0.17	-0.04	0.19	0.059	-0.19	0.0083	-0.069	0.17	-0.035
$A.\alpha_M^{PR}$												1	-0.18	0.0053	**0.56**	0.33	0.18	0.28	-0.096	0.1	-0.2	0.32	0.098
$A.b^{PR}$													1	-0.062	**-0.56**	0.055	-0.12	-0.095	0.13	-0.032	0.088	-0.14	0.018
n^{PR}														1	-0.27	0.053	-0.16	0.069	0.06	0.048	-0.03	-0.08	0.043
A.Frac2															1	0.087	0.29	0.3	-0.18	0.096	-0.24	0.4	0.022
A.Frac1																1	-0.02	0.033	0.012	0.031	0.033	0.033	0.16
$B.\alpha_M^{comb}$																	1	0.25	**-0.67**	0.013	-0.25	**0.7**	-0.062
$B.\alpha_M^{PR}$																		1	-0.27	**0.59**	**-0.86**	**0.67**	0.11
$B.b^{PR}$																			1	-0.042	0.26	**-0.66**	0.008
B.Frac4																				1	**-0.57**	0.23	0.11
B.Frac3																					1	**-0.54**	0.13
B.Frac2																						1	0.13
B.Frac1																							1

TABLE B.3: Correlation table of free parameters in the full simultaneous fit to both datasets with signal proper-time acceptance parameters free. Frac1 refers to the fraction of signal events to the total number of events. Frac2 refers the fraction of combinatoric background events to the total number of background events. Frac3 refers the fraction of PR background events to the total number of non-combinatoric background events. Frac4 refers to the fraction of B_d events to mis-ID events

	$\sigma 1^{sig}$	m_{B_s}	Γ	$\Delta\Gamma$	b^{sig}	n^{sig}	$A.\alpha_M^{comb}$	σ^{comb}	α^{comb}	η^{comb}	b^{comb}	Y^{comb}	$A.\alpha_M^{PR}$	$A.b^{PR}$	n^{PR}	A.Frac2	A.Frac1	$B.\alpha_M^{comb}$	$B.\alpha_M^{PR}$	$B.b^{PR}$	B.Frac4	B.Frac3	B.Frac2	B.Frac1
$\sigma 1^{sig}$	1	-0.21	-0.083	0.033	0.17	0.14	-0.059	0.025	0.024	0.02	0.03	-0.015	0.23	0.017	0.035	0.087	0.35	-0.02	0.0026	0.0036	0.027	0.15	0.057	0.37
m_{B_s}		1	0.021	-0.0095	-0.026	-0.024	0.02	0.0067	0.025	0.011	-0.014	0.0031	-0.014	-0.005	0.0051	-0.018	-0.096	0.012	0.075	-0.0063	-0.11	-0.17	0.00075	-0.21
Γ			1	0.11	**-0.63**	-0.4	-0.0085	-0.018	-0.038	-0.074	-0.063	-0.011	-0.01	0.0059	0.013	-0.013	-0.01	0.0085	0.016	-0.0091	0.0024	-0.026	0.01	-0.023
$\Delta\Gamma$				1	0.2	0.18	-0.0003	0.0023	0.027	0.056	0.031	0.0048	-0.0019	-0.0044	0.0018	-0.0014	0.0021	-0.011	-0.013	0.0078	-0.0022	0.016	-0.013	0.01
b^{sig}					1	**0.71**	-0.049	0.032	0.04	0.04	0.11	-0.012	0.016	-0.034	0.074	-0.03	0.075	-0.073	-0.0021	0.028	0.02	0.022	-0.045	0.1
n^{sig}						1	0.1	0.0047	0.049	0.028	0.13	0.063	0.077	-0.1	0.046	0.12	-0.022	0.046	0.026	-0.03	0.015	0.00047	0.054	0.011
$A.\alpha_M^{comb}$							1	-0.033	0.18	0.11	-0.14	0.13	0.17	**-0.55**	-0.27	**0.67**	-0.12	0.24	0.2	-0.17	0.065	-0.18	0.28	-0.041
σ^{comb}								1	-0.31	-0.14	**0.51**	-0.031	0.11	0.0034	0.25	0.032	0.037	-0.038	0.11	0.11	0.04	-0.073	0.043	0.031
α^{comb}									1	**0.81**	-0.2	0.063	0.31	-0.021	-0.12	0.32	0.046	0.25	0.43	-0.15	0.17	-0.36	0.43	0.041
η^{comb}										1	-0.13	0.024	0.19	-0.052	0.0042	0.19	0.029	0.17	0.27	-0.12	0.11	-0.22	0.27	0.028
b^{comb}											1	0.46	-0.11	0.22	-0.15	-0.18	0.00028	-0.25	-0.22	0.3	-0.094	0.21	-0.31	0.00095
Y^{comb}												1	0.024	-0.039	-0.25	0.13	-0.035	0.14	0.032	-0.13	0.0016	-0.042	0.12	-0.031
$A.\alpha_M^{PR}$													1	-0.21	0.017	**0.57**	0.33	0.2	0.31	-0.14	0.12	-0.23	0.34	0.096
$A.b^{PR}$														1	-0.12	**-0.58**	0.046	-0.15	-0.13	0.16	-0.052	0.12	-0.18	0.0096
n^{PR}															1	-0.22	0.049	-0.11	0.076	-0.0083	0.05	-0.04	-0.034	0.043
A.Frac2																1	0.091	0.32	0.34	-0.22	0.13	-0.28	0.43	0.027
A.Frac1																	1	-0.016	0.032	0.0071	0.029	0.028	0.032	0.15
$B.\alpha_M^{comb}$																		1	0.31	**-0.7**	0.05	-0.31	**0.72**	-0.058
$B.\alpha_M^{PR}$																			1	-0.34	**0.62**	**-0.87**	**0.71**	0.1
$B.b^{PR}$																				1	-0.084	0.32	**-0.7**	0.0037
B.Frac4																					1	**-0.6**	0.27	0.1
B.Frac3																						1	**-0.58**	0.12
B.Frac2																							1	0.12
B.Frac1																								1

TABLE B.4: Correlation table of free parameters in the full simultaneous fit to both datasets with the constraint applied from $B_s^0 \to J/\psi\phi$ with signal proper-time acceptance parameters free. Frac1 refers to the fraction of signal events to the total number of events. Frac2 refers the fraction of combinatoric background events to the total number of background events. Frac3 refers the fraction of PR background events to the total number of non-combinatoric background events. Frac4 refers to the fraction of B_d events to mis-ID events

Appendix C

Additional Results

This appendix presents the results to fits to data with ϵ^{sig} fixed to MC. This differs from the fits located in the chapter 7 which floated the proper-time acceptance parameters.

C.1 A Fit to SelA

The fit was performed over the full proper-time range $(0-15\,\mathrm{ps})$ with a full description of the proper-time acceptance fixed to the MC values. The fit results for Γ_{FS} are given in Table C.1, the mass and time projection plots shown in Figures C.1 and C.2 respectively.

A total of $12,272$ events passed the SelA cuts, the PDF fractions reflect the embedded nature of the PDF model. However we can use these values to identify the number of events categorised by each PDF, the results are shown in Table C.2. The fit to SelA data gives $\Gamma_{FS} = 0.679 \pm 0.012\,\mathrm{ps}^{-1}$.

PDF		Parameters	Usage in fit	Fit Result and Error
Signal	mass	$frac_{\sigma 1}^{sig}$	Fixed	0.93
		$\sigma 1^{sig}$	Free	$19.3 \pm 0.4\,\mathrm{MeVc}^{-2}$
		$ratio_{21}^{sig}$	Fixed	10.5
		m_{B_s}	Free	$5358.6 \pm 0.4\,\mathrm{MeVc}^{-2}$
	lifetime	$\mathbf{\Gamma_{FS}}$	Free	$\mathbf{0.67936 \pm 0.011578}\,\mathrm{ps}^{-1}$
		$\Delta\Gamma_s$	Fixed	$0.0\,\mathrm{ps}^{-1}$
		t_0^{sig}	Fixed	0.2 ps
		n^{sig}	Fixed	1.19
		b^{sig}	Fixed	$1.77\,\mathrm{ps}^{-1}$
		c^{sig}	Fixed	$-0.0261\,\mathrm{ps}^{-1}$
bkg^{comb}	mass	α_M^{comb}	Free	0.0006 ± 0.0002
	lifetime	σ^{comb}	Free	$0.614 \pm 0.040\,\mathrm{ps}^{-1}$
		α^{comb}	Free	-1.67 ± 0.14
		η^{comb}	Free	2.90 ± 0.36
		t_0^{comb}	Fixed	0.2 ps
		b^{comb}	Free	$2 \pm 27\,\mathrm{ps}^{-1}$
		Y^{comb}	Free	0.07 ± 0.7
bkg^{PR}	mass	α_M^{PR}	Free	0.0099 ± 0.0004
	lifetime	τ^{PR}	Free	1.42 ± 0.05 ps
		t_0^{PR}	Fixed	0.2 ps
		n^{PR}	Free	2.18 ± 0.60
		b^{PR}	Free	$2.65 \pm 0.30\,\mathrm{ps}^{-1}$
		c^{PR}	Fixed	$0.0\,\mathrm{ps}^{-1}$
PDF Fractions	Signal Events/Total Events		Free	0.371 ± 0.021
	Comb bkg/Total bkg Events		Free	0.505 ± 0.021

TABLE C.1: Fit results of the full fit to SelA data with signal proper-time acceptance parameters fixed from MC.

PDF	Percentage	# Events
Signal	37.1%	4553
Combinatoric Background	32.3%	3964
PR Background	31.6%	3878

TABLE C.2: The percentage of the fit to SelA data allocated to each PDF and the corresponding number of events.

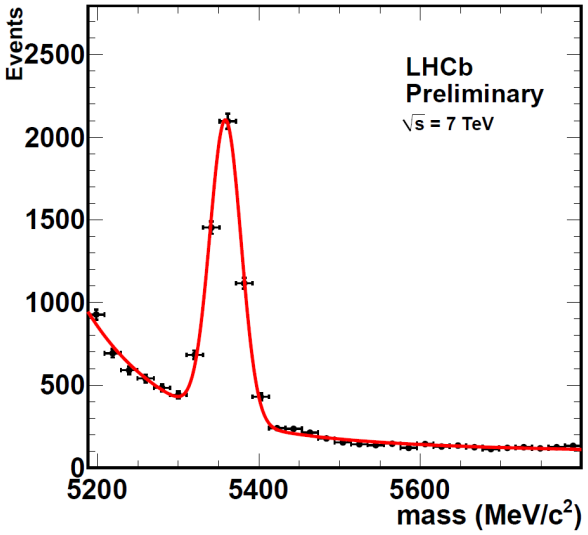

FIGURE C.1: Mass projection of $0 - 15\,\text{ps}$ fit to SelA with signal proper-time acceptance parameters fixed from MC.

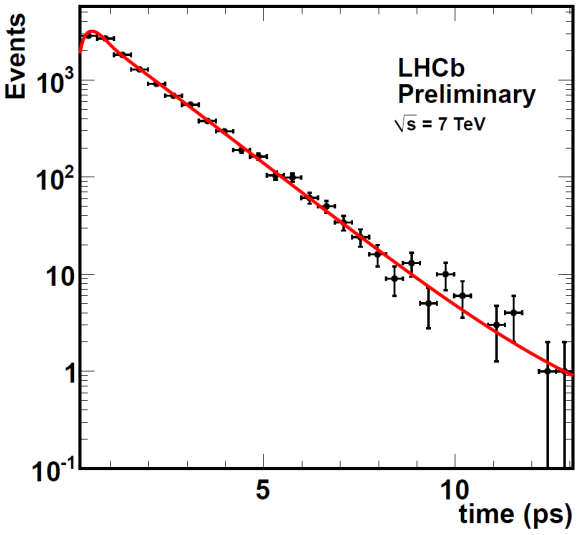

FIGURE C.2: Time projection of $0 - 15\,\text{ps}$ fit to SelA with signal proper-time acceptance parameters fixed from MC.

C.2 A fit to SelB

The fit results for the full range fit to Γ_{FS} are given in Table C.3, the mass and time projection plots shown in Figures C.3 and C.4 respectively.

A total of 15588 events passed the SelB cuts and are consistent with the fit phase-space, the PDF fractions reflect the embedded nature of the PDF model, however we can use these values to identify the number of events categorised by each PDF, the results are shown in Table C.4. The fit to SelB data concludes $\Gamma_{FS} = 0.687 \pm 0.015\,\text{ps}^{-1}$.

C.3 A Simultaneous Fit

The fit results for the full range fit to Γ_{FS} with proper-time acceptance fixed to MC are given in Table C.5, the projection plots of the SelA mass and time, and the SelB mass and time shown in Figures C.5, C.7, C.6, C.8 respectively.

PDF		Parameters	Usage in fit	Fit Result and Error
Signal	mass	$frac_{\sigma 1}^{sig}$	Fixed	0.93
		$\sigma 1^{sig}$	Free	$16.8 \pm 0.5\,\mathrm{MeVc}^{-2}$
		$ratio_{21}^{sig}$	Fixed	10.5
		m_{B_s}	Free	$5359.2 \pm 0.6\,\mathrm{MeVc}^{-2}$
	lifetime	$\mathbf{\Gamma_{FS}}$	Free	$\mathbf{0.68566 \pm 0.014878}\,\mathrm{ps}^{-1}$
		$\Delta\Gamma_s$	Fixed	$0.0\,\mathrm{ps}^{-1}$
		t_0^{sig}	Fixed	0.2 ps
		n^{sig}	Fixed	1.19
		b^{sig}	Fixed	$1.77\,\mathrm{ps}^{-1}$
		c^{sig}	Fixed	$-0.0261\,\mathrm{ps}^{-1}$
bkg^{comb}	mass	α_M^{comb}	Free	0.0006 ± 0.0001
	lifetime	σ^{comb}	Free	0.586 ± 0.075 ps
		α^{comb}	Free	-1.619 ± 0.092
		η^{comb}	Free	2.62 ± 0.20
		t_0^{comb}	Fixed	0.2 ps
		b^{comb}	Free	$4.0 \pm 5.6\,\mathrm{ps}^{-1}$
		Y^{comb}	Free	0.42 ± 0.19
bkg^{PR}	mass	α_M^{PR}	Free	0.0114 ± 0.0012
	lifetime	τ^{PR}	Free	1.285 ± 0.061 ps
		t_0^{PR}	Fixed	0.2 ps
		n^{PR}	Free	1.78 ± 0.47
		b^{PR}	Free	$2.16 \pm 0.49\,\mathrm{ps}^{-1}$
		c^{PR}	Fixed	$0\,\mathrm{ps}^{-1}$
bkg^{B_d}	mass	$frac_{\sigma 1}^{B_d}$	Fixed	0.765
		$\sigma_1^{B_d}$	Fixed	$21.3\,\mathrm{MeVc}^{-2}$
		$\sigma_2^{B_d}$	Fixed	$77.2\,\mathrm{MeVc}^{-2}$
		$mean^{B_d}$	Fixed	$5321.1\,\mathrm{MeVc}^{-2}$
	lifetime	τ^{B_d}	Fixed	1.43 ps
		ϵ^{sig}	–	––
bkg^{Λ_b}	mass	σ^{Λ_b}	Fixed	$51.2\,\mathrm{MeVc}^{-2}$
		α^{Λ_b}	Fixed	0.62
		η^{Λ_b}	Fixed	125
		$mean^{\Lambda_b}$	Fixed	$5430\,\mathrm{MeVc}^{-2}$
	lifetime	τ^{Λ_b}	Fixed	1.48 ps
		ϵ^{sig}	–	––
PDF Fractions	Signal Events/Total Events		Free	0.220 ± 0.006
	Comb bkg/Total bkg		Free	0.579 ± 0.017
	PR bkg/Non-comb bkgs		Free	0.635 ± 0.038
	B_d bkg/Miss-ID bkg		Free	0.730 ± 0.035

TABLE C.3: Fit results of the full fit to SelB data with signal proper-time acceptance parameters fixed from MC.

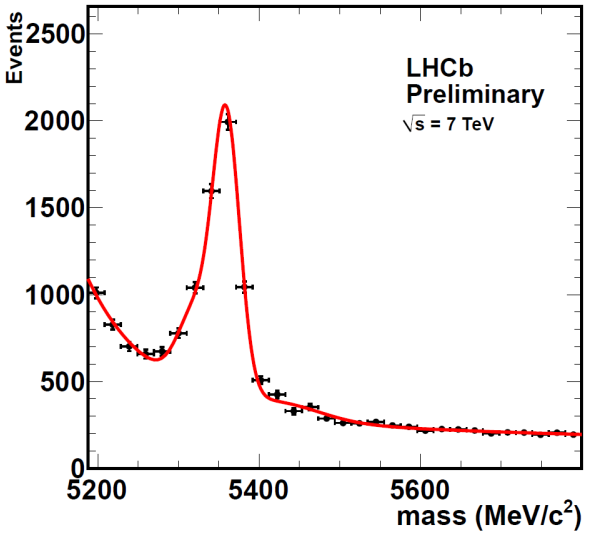

FIGURE C.3: Mass projection of 0 – 15 ps fit to SelB.

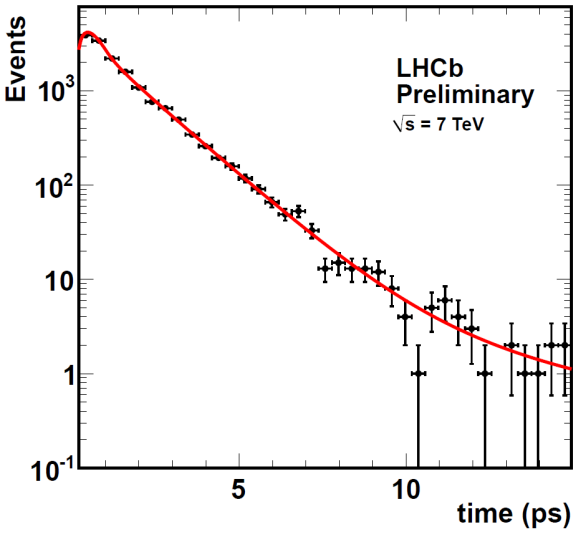

FIGURE C.4: Time projection of 0 – 15 ps fit to SelB.

PDF	Percentage	# Events
Signal	22.0%	3429
Combinatoric Background	45.2%	7046
PR Background	20.9%	3258
B_d Background	8.7%	1356
Λ_b Background	3.2%	499

TABLE C.4: The percentage of the fit to SelB data allocated to each PDF and the corresponding number of events.

It is important to compare the simultaneous fit results to those obtain in the individual fit to ensure that fit parameters are not being overly constrained. A good indication of the similarity between fits is the breakdown of events categorised by each contributing PDF. Table C.6 summarises the fractions of events identified as each PDF in the fits, this table can be compared to Tables C.2 and C.4. It can be seen that a greater percentage of the SelB data is assigned as signal in the simultaneous fit compared to the individual fit, this corresponds to ~ 200 events; the SelA signal PDF includes ~ 60 fewer events than found by the SelA individual fit. These differences can be attributed to the shared B_s^0 mass peak in the simultaneous fits.

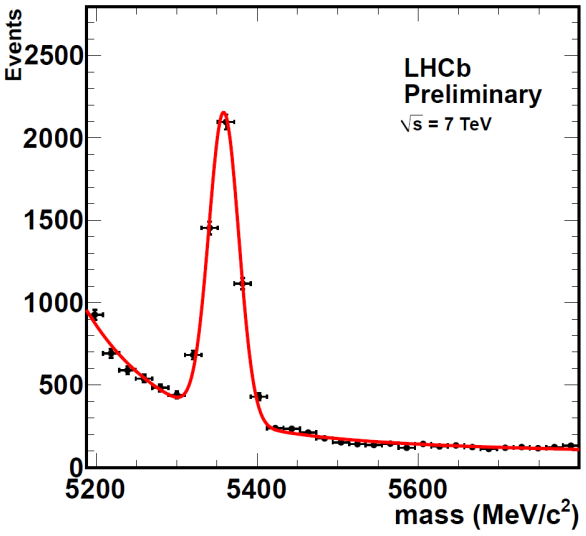

FIGURE C.5: SelA mass projection of a full simultaneous fit to SelA and SelB data in the range $0 - 15$ ps.

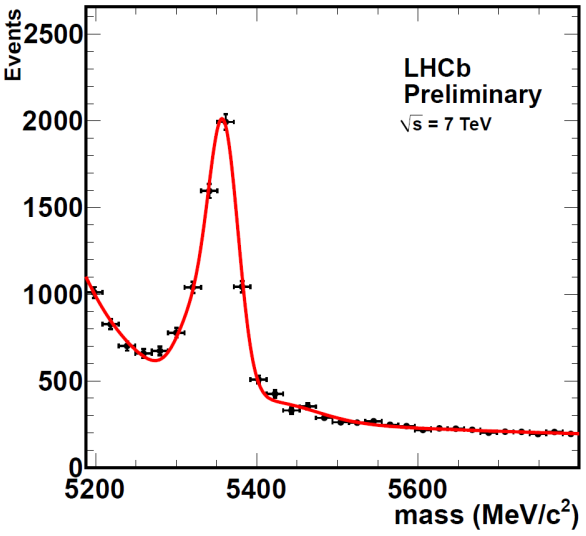

FIGURE C.6: SelB mass projection of a full simultaneous fit to SelA and SelB data in the range $0 - 15$ ps.

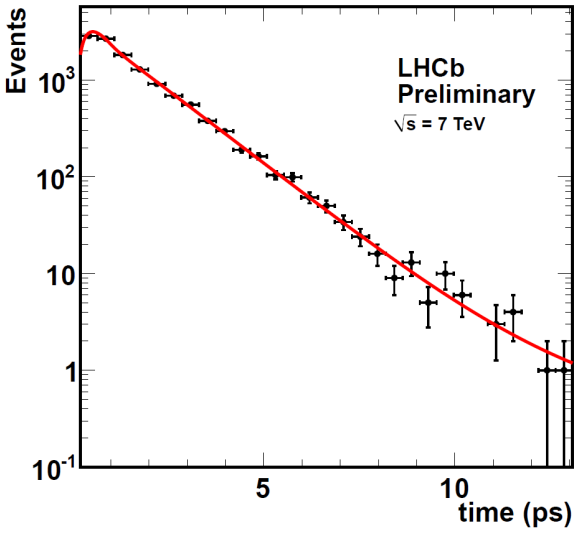

FIGURE C.7: SelA time projection of a full simultaneous fit to SelA and SelB data in the range $0 - 15$ ps.

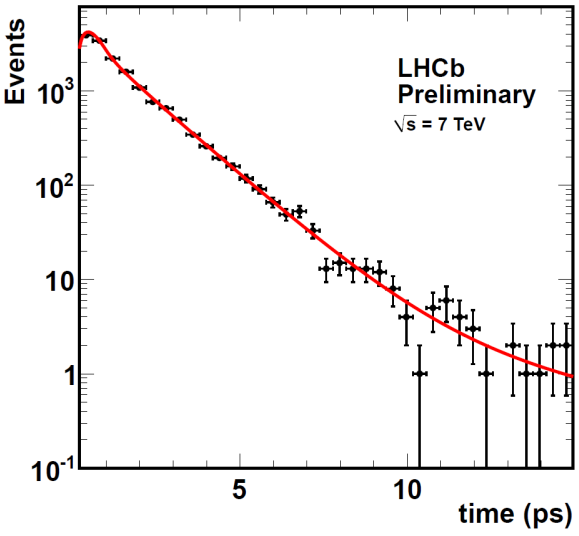

FIGURE C.8: SelB time projection of a full simultaneous fit to SelA and SelB data in the range $0 - 15$ ps.

				Fit Result and Error	
PDF		Parameters	Usage	SelA	SelB
Signal	mass	$frac_{\sigma 1}^{sig}$	Fixed	0.93	
		$\sigma 1^{sig}$	Free	$18.6 \pm 0.3\,\mathrm{MeVc}^{-2}$	
		$ratio_{21}^{sig}$	Fixed	10.493	
		m_{B_s}	Free	$5358.6 \pm 0.3\,\mathrm{MeVc}^{-2}$	
	lifetime	$\mathbf{\Gamma_{FS}}$	Free	$\mathbf{0.68169 \pm 0.0090989}\,\mathrm{ps}^{-1}$	
		$\Delta\Gamma_s$	Fixed	$0.0\,\mathrm{ps}^{-1}$	
		t_0^{sig}	Fixed	0.2 ps	
		n^{sig}	Fixed	1.19	
		b^{sig}	Fixed	$1.77\,\mathrm{ps}^{-1}$	
		c^{sig}	Fixed	$-0.0261\,]ps^{-1}$	
bkg^{comb}	mass	α_M^{comb}	Free	0.0008 ± 0.0014	0.0005 ± 0.0001
	lifetime	σ^{comb}	Free	$0.625 \pm 0.015\,\mathrm{ps}$	
		α^{comb}	Free	-1.665 ± 0.052	
		η^{comb}	Free	2.63 ± 0.15	
		t_0^{comb}	Fixed	0.2 ps	
		b^{comb}	Free	$14.1 \pm 9.2\,\mathrm{ps}^{-1}$	
		Y^{comb}	Free	0.256 ± 0.061	
bkg^{PR}	mass	α_M^{PR}	Free	0.0102 ± 0.0004	0.0098 ± 0.0009
	lifetime	τ^{PR}	Free	$1.425 \pm 0.046\,\mathrm{ps}$	$1.328 \pm 0.051\,\mathrm{ps}$
		t_0^{PR}	Fixed	0.2 ps	
		n^{PR}	Free	2.51 ± 0.67	2.10 ± 0.50
		b^{PR}	Free	$2.41 \pm 0.23\,\mathrm{ps}^{-1}$	$2.85 \pm 0.50\,\mathrm{ps}^{-1}$
		c^{PR}	Fixed	$0\,]ps^{-1}$	
bkg^{B_d}	mass	$frac_{\sigma 1}^{B_d}$	Fixed	–	0.765
		$\sigma_1^{B_d}$	Fixed	–	$21.3\,\mathrm{MeVc}^{-2}$
		$\sigma_2^{B_d}$	Fixed	–	$77.2\,\mathrm{MeVc}^{-2}$
		$mean^{B_d}$	Fixed	–	$5321.1\,\mathrm{MeVc}^{-2}$
	lifetime	τ^{B_d}	Free	–	1.43 ps
		ϵ^{sig}	–	–	–
bkg^{Λ_b}	mass	σ^{Λ_b}	Fixed	–	$51.2\,\mathrm{MeVc}^{-2}$
		α^{Λ_b}	Fixed	–	0.62
		η^{Λ_b}	Fixed	–	125
		$mean^{\Lambda_b}$	Fixed	–	$5430\,\mathrm{MeVc}^{-2}$
	lifetime	τ^{Λ_b}	Free	–	1.48 ps
		ϵ^{sig}	–	–	–
PDF Fractions	Signal Events/Total Events		Free	0.366 ± 0.006	0.232 ± 0.006
	Comb bkg/Total bkg		Free	0.531 ± 0.018	0.556 ± 0.018
	PR bkg/Non-comb bkgs		Free	–	0.720 ± 0.036
	B_d bkg/Miss-ID bkg		Free	–	0.738 ± 0.047

TABLE C.5: Fit results of the full simultaneous fit to SelA and SelB data.

	SelA		SelB	
PDF	Percentage	# Events	Percentage	# Events
Signal	36.6%	4492	23.2%	3616
Combinatoric Background	33.7%	4136	42.7%	6656
PR Background	29.7%	3645	24.6%	3835
B_d Background	–	–	7.0%	1091
Λ_b Background	–	–	2.5%	390

TABLE C.6: The percentage of the fit to SelB data allocated to each PDF and the corresponding number of events.

The simultaneous fit gives $\Gamma_{FS} = 0.682 \pm 0.009\,\mathrm{ps}^{-1}$ as expected. This result gives the middle ground of the individual fits, as well as a higher precision due to the increased amount of data fitted.

Appendix D

LHCb-2009-014

LHCb internal note "Measurements of $\Delta\Gamma_s$ and Γ_s at LHCb using $B_s \to J/\psi\phi$ and flavour specific B_s decays." is included in full. The paper provides background motivation for the analysis presented in this thesis.

Measurement of $\Delta\Gamma_s$ and $\bar{\Gamma}_s$ at $LHCb$ using $B_s \to J/\psi\phi$ and flavour specific B_s decays

Internal note

Issue: 1
Revision: 0

Reference: LHCb-2009-014
Created: Jan 05, 2009
Last modified: March 17, 2010

Prepared by: P. Clarke[a], G. A. Cowan[a], G. C. Fardell[a]
[a]The University of Edinburgh

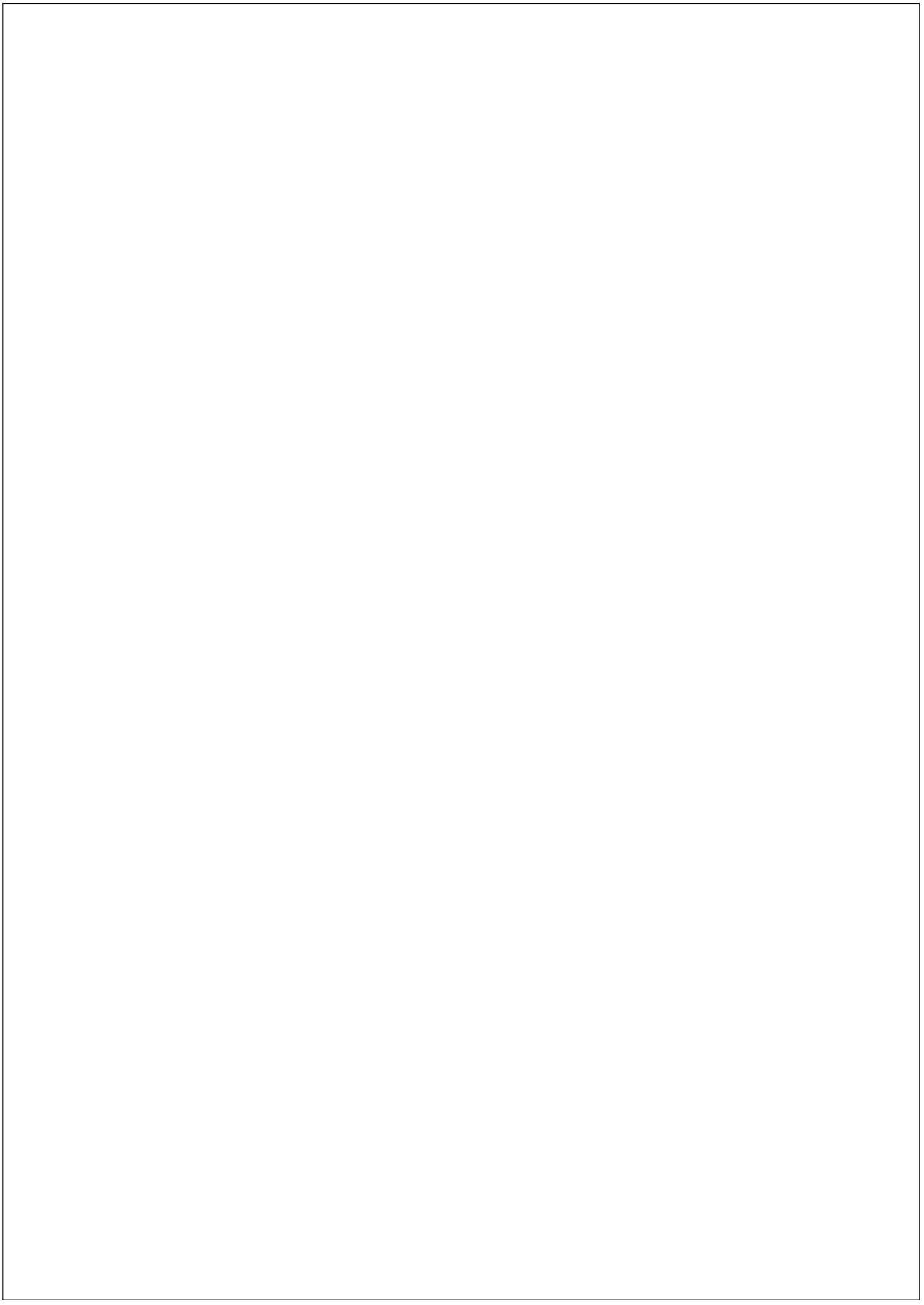

Abstract

$LHCb$ will measure the average B_s^0 decay width ($\bar{\Gamma}_s$) and the B_s^0 decay width difference ($\Delta\Gamma_s$). Information on both of these quantities will be obtained from flavour specific channels such as $B_s \to D_s\pi$ and from CP eigenstate (admixture) channels such as $B_s \to J/\psi\phi$. From $B_s \to J/\psi\phi$ alone $LHCb$ expects to make an early data measurement which will be competitive with the world averages. In this note we quantify why it is important to use data from all channels simultaneously. Each channel has different correlations between the lifetimes which combine to produce a more precise result with a significantly reduced correlation.

1 Introduction

1.1 Motivation

The B_s^0 meson system is described in terms of the two high and low mass eigenstates, B_H and B_L, each having distinct decay widths Γ_H and Γ_L. These are often equivalently referred to as $\bar{\Gamma}_s = (\Gamma_H + \Gamma_L)/2$ and $\Delta\Gamma_s = (\Gamma_L - \Gamma_H)$.

The B_s^0 average lifetime is $\bar{\Gamma}_s = 0.677^{+0.020}_{-0.022} ps^{-1}$ [1]. This measurement is found from combined time-dependant measurements from several experiments (ALEPH, BABAR, BELLE, CDF, D0, DELPHI, L3, OPAL and SLD).

The above value of $\bar{\Gamma}_s$ is found using a single exponential which ignores any decay width difference. The true value of $\bar{\Gamma}_s$ differs by corrections of order $(\Delta\Gamma_s/2\bar{\Gamma}_s)^2$. The standard model predicts $|\Delta\Gamma_s| > 0$ and the current theoretical prediction is $\Delta\Gamma_s = 8.8 \times 10^{-2} \pm 1.7 \times 10^{-2} ps^{-1}$ [2].

A combined result of $\Delta\Gamma_s$ in the B_s^0 system is found from a global fit of all available direct measurements of $\Delta\Gamma_s/\bar{\Gamma}_s$ as well as the lifetime measurements from $B_s \to J/\psi\phi$ decays and flavour-specific decays (CDF, D0, ALEPH and DELPHI data). The resulting $\bar{\Gamma}_s$ and $\Delta\Gamma_s$ values are given in Table 1.

$\bar{\Gamma}_s$	$6.60 \times 10^{-1} \pm 1.5 \times 10^{-2} ps^{-1}$
$\Delta\Gamma_s$	$0.102 \times 10^{-1} \pm 4.3 \times 10^{-2} ps^{-1}$

Table 1: Value and precision of $\Delta\Gamma_s$ and $\bar{\Gamma}_s$ taken from [1].

It is expected that by the time $LHCb$ takes data the Tevatron experiments will approximately halve the error on $\Delta\Gamma_s$ using their final data set ($\sim 4 fb^{-1}$).

The lifetime difference is of particular interest to us. Firstly because it is a fundamental parameter which $LHCb$ will be able to measure well, and secondly because it potentially tells us about sources of new physics. $\Delta\Gamma_s$ can be written as, [2]

$$\Delta\Gamma_s = 2|\Gamma_{12}|\cos(X)$$

The parameter X is defined by,

$$X = \arg(-M_{12}/\Gamma_{12})$$

In this expression Γ_{12} is the off diagonal decay matrix element which is dominated by tree level decays and as such is fairly unaffected by new physics appearing in loops.

We have no intention of introducing a new parameter (X) but simply wish to point out that although this is sometimes called ϕ_s in literature it is not the same as the phase measured in the interference between mixing and decay, which in the SM is the relevant UT angle $\phi_s = -2\beta_s$. What we have called X can be calculated with some precision and is very small $\approx 0.0042 \pm 0.0014$ resulting in: [2]

$$\Delta\Gamma_{SM} = 8.8 \times 10^{-2} \pm 1.7 \times 10^{-2} ps^{-1} \quad (1)$$

New physics gives rise to new phases in M_{12} (but not in Γ_{12}) and hence $X \to X + \phi_{NP}$ and we therefore expect

$$\Delta\Gamma_s \approx \Delta\Gamma_{SM}\cos(\phi_{NP}) \quad (2)$$

The interesting point to note is that the observed value is less than the SM value in the presence of new physics. As we show below, with $0.2 fb^{-1}$ at $LHCb$ we can expect to measure $\Delta\Gamma_s$ to a precision of $\pm 5.82 \times 10^{-2} ps^{-1}$ making this a worth while first year result.

1.2 Lifetime Measurements

The purpose of this note is not to discuss how to measure lifetimes per se, other notes describe this, see references [3, 4, 5]. This note looks at the precison obtainable on a measurement of $\Delta\Gamma_s$ at $LHCb$ including:

1. The limitations of measuring $\Delta\Gamma_s$ from flavour-specific deacys alone (e.g. $B_s \to D_s\pi$).
2. The complimentary information from $B_s \to J/\psi\phi$ and in particular its different correlation between $\Delta\Gamma_s$ and $\bar{\Gamma}_s$.
3. The power of combining the types of decay to reduce the correlation between lifetimes and hence the overall error.

The class of channels which includes $B_s \to D_s\pi$ and $D_s\ell\nu$ are B flavour specific final states and are not CP eigenstates. As such they measure the combination $\exp(-\Gamma_L t) + \exp(-\Gamma_H t)$. Fitting for a single exponential results in a measurement of the average lifetime up to corrections of order $(\Delta\Gamma_s/2\bar{\Gamma}_s)^2$. These channels give a poor constraint on $\Delta\Gamma_s$.

The class of channels which includes $B_s \to J/\psi\phi$ are CP eigenstates and hence have the potential to measure either Γ_L or Γ_H. In the case of $B_s \to J/\psi\phi$, because the final state is a mixture of CP even and CP odd, an angluar analysis must be performed to (at least partially) separate the two components.

It is clear that each of these channels makes a measurement of the two parameters $[\Gamma_L, \Gamma_H]$ or equivalently $[\bar{\Gamma}_s, \Delta\Gamma_s]$ with different precisions and correlations. By combining them in a simultaneous negative log-likelihood (NLL) fit there will be a reduction on both the overall error on each parameter and the overall correlation between the parameters.

This note uses both Monte Carlo (MC) toy studies and data generated by using the 2006 $LHCb$ geometry to study the sensitivity and correlations in the channels.

2 Channels

2.1 $B_s \to D_s\pi$

$B_s \to D_s\pi$ is a flavour specific decay, i.e. the B_s^0 flavour at the point of its decay is known from the charge of its decay products. The B_s^0 decays to $D_s^-\pi^+$ final state, and the $\bar{B}_s$ to a $D_s^+\pi^-$ final state. The $B_s \to D_s\pi$ channel has a large branching fraction $(3.4 \pm 0.7) \times 10^{-3}$ and can be cleanly reconstructed. This decay has only one dominant tree diagram, Figure 1.

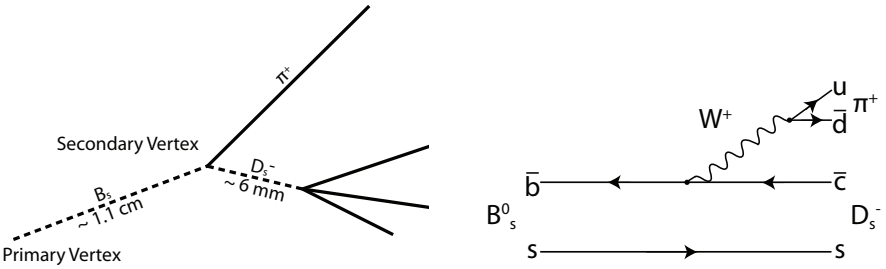

Figure 1: $B_s \to D_s\pi$ decay (left) and tree diagram (right).

No CP violation is expected in these decays. The proper time distribution for this decay is given by Equation 3 where R(t) is the decay rate. It can be seen that the distribution is given by a superposition of two exponentials of decay widths $\Gamma_s \pm \Delta\Gamma_s/2$ overlaid with a sinusoidal term.

$$R(t) \propto \frac{1}{2}\{e^{-\Gamma_H t} + e^{-\Gamma_L t} + rDe^{-\bar{\Gamma}_s t}\cos(\Delta M_s t)\} \tag{3}$$

where $r = +1$ for B_s^0 decays tagged as unmixed, -1 for B_s^0 decays tagged as mixed, and 0 for untagged B_s^0 decays and $D = 1 - 2\omega$ is the dilution factor due to the mistagging rate ω. This study is only concered with untagged events, hence the last term is dropped and the distribution becomes,

$$R(t) \propto \frac{1}{2}\{e^{-\Gamma_H t} + e^{-\Gamma_L t}\} \tag{4}$$

Flavour specific decays are traditionally used to make lifetime measurements using a single exponential fit to both lifetimes in order to make a measurment of the average. Fitting for a single exponential one obtains a measurement of the observed flavour-specific lifetime, Γ_{obs}. If $\Delta\Gamma_s$ is small it becomes hard to differentiate between the two exponentials, hence Γ_{obs} is approximately $\bar{\Gamma}_s$. Γ_{obs} is related to $\bar{\Gamma}_s$ by a second order correction $(\Delta\Gamma_s/2\bar{\Gamma}_s)^2$, as shown in Equation 5. This method of measuring $\bar{\Gamma}_s$ is valid whilst the correction is less than the statistical precision of the measurement.

$$\frac{1}{\Gamma_{obs}} = \frac{1}{\Gamma_s}\frac{1 + \left(\frac{\Delta\Gamma_s}{2\Gamma_s}\right)^2}{1 - \left(\frac{\Delta\Gamma_s}{2\Gamma_s}\right)^2} \tag{5}$$

It can be seen that the correction gives a 0.5% effect when $\Delta\Gamma_s \sim 0.1ps^{-1}$ and $\bar{\Gamma}_s \sim 0.7ps^{-1}$. At $LHCb$ the statistical precision will exceed this very early in the data taking and thus naive fitting to flavour specific channels will not be meaningful without making some assertion about $\Delta\Gamma_s$.

The alternative is to perform a simultaneous fit for both $\bar{\Gamma}_s$ and $\Delta\Gamma_s$. However as we shall see in Section 3.2.1 this does not work well in practice using this channel alone.

2.2 $B_s \to J/\psi\phi$

The $B_s \to J/\Psi(\mu^+\mu^-)\phi(K^+K^-)$ channel involves decays to both CP even and CP odd eigenstates. The phenomenology is fully described in [3, 6]. The different CP eigenstates are predominantly the result of either B_H or B_L decays and hence dependent upon Γ_H or Γ_L respectively.

Equation 6 shows the differential cross section as a function of the single decay angle, θ_{tr}, known as the *transversity* angle. θ_{tr} along with decay angles θ_ϕ, ϕ_{tr} are defined in reference [3], along with the analogous expressions of their differential cross sections.

$$\begin{aligned}\frac{d\Gamma(t)}{d\cos\theta_{tr}} \quad \propto \quad & (1-R_\perp)[(1+\cos\phi_s)e^{-\Gamma_L t}+(1-\cos\phi_s)e^{-\Gamma_H t}]\frac{1}{2}(1+\cos^2\theta_{tr}) \\ & + R_\perp[(1-\cos\phi_s)e^{-\Gamma_L t}+(1+\cos\phi_s)e^{-\Gamma_H t}]\sin^2\theta_{tr}\end{aligned} \tag{6}$$

In this expression $R_\perp$ is the fraction of the CP odd component at time $t = 0$, equivelently in the analogous expressions R_0 is the fraction of the CP even component at time $t = 0$. $R_\perp$ is expected to be ~ 0.2 in the SM. If we set $\phi_s = 0$ (a good approximation in the SM) this simplifies to equation 7.

$$\frac{d\Gamma(t)}{d\cos\theta_{tr}} \propto (1-R_\perp)e^{-\Gamma_L t}(1+\cos^2\theta_{tr}) + 2R_\perp e^{-\Gamma_H t}\sin^2\theta_{tr} \tag{7}$$

We can see the salient features: the expression is the sum of two exponentials with different weights, but these can at least be partially separated by using the angular information. If the angular analysis gave perfect separation then this channel would yield independent measurements of Γ_H and Γ_L with no correlation. In fact the separation is not perfect and hence there remains some negative correlation. It is trivial to understand the negative correlation as any angular overlap contains information from both Γ_H and Γ_L; if a fit to increase the number of one it must reduce the number of the other to maintain a fit and hence there will be a negative correlation between Γ_H and Γ_L.

The analogous expressions when all three decay angles are used is significantly more complicated. The characteristics are the same and the separation of the different CP final states is naturally better (as more information is available) and hence the measurements of Γ_H and Γ_L have less correlation.

3 MC Toy Study Without Detector Effects

3.1 About the study

To illustrate the fitting power of the channels MC toy studies were performed at an ideal level (i.e. without taking proper time acceptance, resolution or background taken into consideration). Simultaneous negative log-likliehood fit (refered to onwards as simultaneous fits) for both $\Delta\Gamma_s$ and $\bar{\Gamma}_s$ were performed with input values of $0.1ps^{-1}$ and $0.7ps^{-1}$ respectively, the input values can be seen in Table **??**. These toy studies were performed on each channel independently, and then on the channels combined.

$\bar{\Gamma}_s$	$0.70ps^{-1}$
$\Delta\Gamma_s$	$0.10ps^{-1}$
$R_\perp$	0.20
R_0	0.20

Table 2: The initial values used in the MC toy study.

At $LHCb$ in one nominal year of running we expect $2fb^{-1}$ of data, this corresponds to 140k $B_s \to D_s\pi$ events [7] and 100k $B_s^0 \to J/\psi(\mu\mu)\phi$ events [8]. When performing the combined channel study the event yields have been chosen in the correct proportion for the decay channels.

We used RooFit to generate and fit the toy MC data accordingly to PDFs written by us. In each experiment ≈ 100 toys were generated. The fit was then a simultaneous fit of all free parameters. In the case of $B_s \to D_s\pi$ the free parameters were only $\Delta\Gamma_s$ and $\bar{\Gamma}_s$, $R_\perp$ and R_0 were also floated for fits using $B_s \to J/\psi\phi$. Other parameters described in [3] were not consequencial to the conclusion of this note and thus were fixed to $\delta_1 = -0.46, \delta_2 = 2.92$, $\phi_s = -0.04$ and $\Delta m_s = 17.77$.

3.2 Results

3.2.1 MC Toy study in $B_s \to D_s\pi$

The NLL distribution of $\bar{\Gamma}_s$ is always parabolic and well behaved. Figures 3, 4 and 5 show a range of the possible NLLs of $\Delta\Gamma_s$ which result, and Figures 6, 7, and 8 show the corresponding correlation plots for $\Delta\Gamma_s$ and $\bar{\Gamma}_s$; the 1σ and 2σ contours are shown and the central value is shown by the point.

It is evident that $\Delta\Gamma_s$ does not behave as a simple parabolic variable. The NLL curve is symmetric about zero (depending upon $\cosh(\Delta\Gamma_s)$) and the height of the central bump ranges from zero upward and depends upon statistical fluctuations. Therefore it is clear that, depending upon the height of the bump, the meaning of $\Delta(NLL) = +1/2, +1$ etc is not well defined and the constraint upon $\Delta\Gamma_s$ cannot be given with a simple gaussian error. It is evident from Figures 3 -8 that the simultaneous fit gives a non elliptical correlation due to the shape of the $\Delta\Gamma_s$ NLL.

We futher illustrate this in Figure 2 by showing the pull distribution of $\Delta\Gamma_s$ when it is unconstrained. This demonstrates the instability of a simultaneous fit for both parameters.

We conclude that it is not likely to be very useful to try to perform a simultaneous fit with this channel alone. With more than 10k events, the precision on $\bar{\Gamma}_s$ becomes similar to the error introduced by an unknown value of $\Delta\Gamma_s$ so some assertion about $\Delta\Gamma_s$ would be needed.

For completness the precisions obtained on $\bar{\Gamma}_s$ with a fixed $\Delta\Gamma_s$ are given in Table 3.

3.2.2 MC Toy study in $B_s \to J/\psi\phi$

The contour plot and correlation matrix for a simultaneous fit to $\bar{\Gamma}_s$, $\Delta\Gamma_s$, $R_\perp$ and R_0 in this channel is shown in given in Figure 9 and Table 6. Both NLL plots are parabolic and the simultaneous

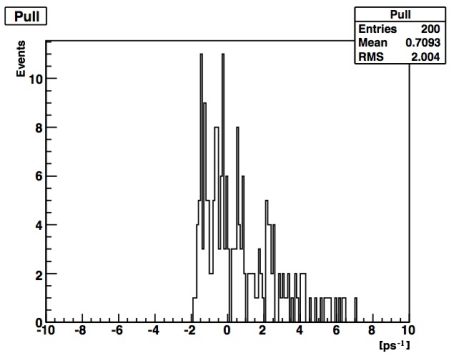

Figure 2: The pull distrubution of $\Delta\Gamma_s$ fit values for 200 experiments. A simultaneous fit of $\bar{\Gamma}_s$ and $\Delta\Gamma_s$ was performed in $B_s \to D_s\pi$

# $D_s\pi$ events	$\bar{\Gamma}_s$ precision with $\Delta\Gamma_s$ constrained $[ps^{-1}]$
100k	2.18×10^{-3}
10k	6.88×10^{-3}
1k	2.21×10^{-2}

Table 3: A comparison of the average precision obtained on $\bar{\Gamma}_s$ from a fit to $\bar{\Gamma}_s$ when $\Delta\Gamma_s$ is fixed to $0.1ps^{-1}$.

fit gives an elliptical contour plot due to the correlation between $\Delta\Gamma_s$ and $\bar{\Gamma}_s$. This is because $B_s \to J/\psi\phi$ is the channel closest to making independent measurements of Γ_L and Γ_H.

The precision obtained on $\bar{\Gamma}_s$ and $\Delta\Gamma_s$ for this channel at a range of event yields is given in Table 4. We may compare this to the $B_s \to D_s\pi$ case where we observe that the overall error on $\bar{\Gamma}_s$ is similar when comparing equal numbers of events, but is actually somewhat better due to the much stronger constraint upon $\Delta\Gamma_s$.

# $J/\psi\phi$ events	$\Delta\Gamma_s$ precision $[ps^{-1}]$	$\bar{\Gamma}_s$ precision $[ps^{-1}]$
100k	8.90×10^{-3}	3.04×10^{-3}
10k	2.79×10^{-2}	9.56×10^{-3}
1k	8.61×10^{-2}	3.05×10^{-2}

Table 4: Average precision obtained for $\bar{\Gamma}_s$ and $\Delta\Gamma_s$ for a simultaneous fit.

3.2.3 MC Toy Study in Both Channels Combined

The contour plot (Figure 10) and correlation matrix (Table 7) are shown for a simultaneous fit to $\bar{\Gamma}_s$, $\Delta\Gamma_s$, $R_\perp$ and R_0 using infomation from both $B_s \to J/\psi\phi$ and $B_s \to D_s\pi$ at one nominal years worth of events. The correlation between $\Delta\Gamma_s$ and $\bar{\Gamma}_s$ seen when the channels are combined is ≈ 0 compared with the correlation obtained by a fit using $B_s \to J/\psi\phi$ alone ≈ -0.64. The reduction in the correlation between $\bar{\Gamma}_s$ and $\Delta\Gamma_s$ achieved by a combined fit is clear.

It is worth noting that although it seems that the correlation between $\Delta\Gamma_s$ and $\bar{\Gamma}_s$ completely vanishes by combining the channels this is an function of the ratio of events used and varies for different proportions. A detailed correlation study can be found in the Appendix B.3. The message is that the correlation is significantly reduced when the channel information is combined.

The precision on $\bar{\Gamma}_s$ and $\Delta\Gamma_s$ obtained from combining the channels are shown in Table 5. The precision is shown at nominal luminosities of 2, 0.2 and 0.02 fb^{-1}. The precision of $\bar{\Gamma}_s$ is incresed by a factor of 2, and $\Delta\Gamma_s$'s precison increased by a factor of 1.5 by combining the channels.

As was discussed inSection 3.2.1 the best precision on $\bar{\Gamma}_s$ was obtained in the $B_s \to D_s\pi$ channel when $\Delta\Gamma_s$ was constrained. By combining the channels $B_s \to J/\psi\phi$ provides the required constraint to make full use of the $B_s \to D_s\pi$ information.

# $J/\phi\psi$ events	# $D_s\pi$ events	$\Delta\Gamma_s$ precision $[ps^{-1}]$	$\bar{\Gamma}_s$ precision $[ps^{-1}]$
100k	140k	5.64×10^{-3}	1.44×10^{-3}
10k	14k	1.79×10^{-2}	4.56×10^{-3}
1k	1.4k	5.77×10^{-2}	1.48×10^{-2}

Table 5: Average fit value and precision using both channels, of 200 experiments for $\bar{\Gamma}_s$ and $\Delta\Gamma_s$ for a simultaneous fit at a range of luminosities.

3.3 Conclusion

By combining the results from both the $B_s \to J/\psi\phi$ and $B_s \to D_s\pi$ channels an improvement on the precision of $\bar{\Gamma}_s$ and $\Delta\Gamma_s$ is obtained. The improvement in the $\bar{\Gamma}_s$ value is simply from adding primary information from a different channel; the improvement seen in the precision of $\Delta\Gamma_s$ is not from additional information but because the correlation between $\Delta\Gamma_s$ and $\bar{\Gamma}_s$ is reduced. This is an important message of this study: that $LHCb$ will produce its best statement on $\Delta\Gamma_s$ through a combined fit which correctly takes the correlations from each channel into account.

We therefore now investigate the precision that can be obtained if the study is extended past the ideal level to include proper time resolution; acceptance and background in both channels.

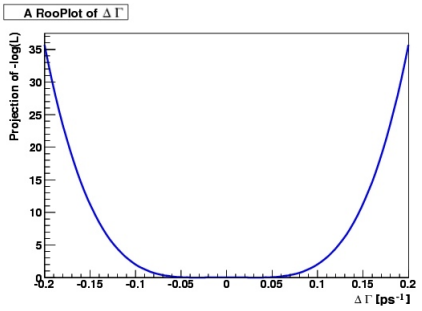

Figure 3: The NLL curve of $\Delta\Gamma_s$ at $\bar{\Gamma}_s = 0.7$. It is symmetric about zero and in this data set no central bump results. The input value of $\Delta\Gamma_s$ is $+0.1$.

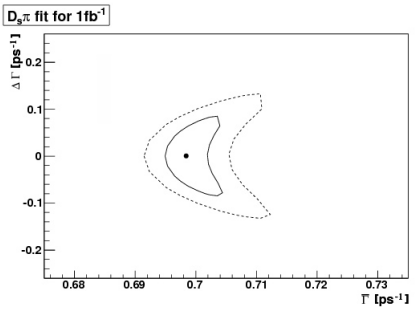

Figure 6: The 2d NLL contour plot corresponding to Figure 3. The solid line is 1σ and the dotted line is 2σ. The minimum of $\Delta\Gamma_s$ is found at zero due to the symmetric flat bottomed likelihood. The contours are also symmetric about zero.

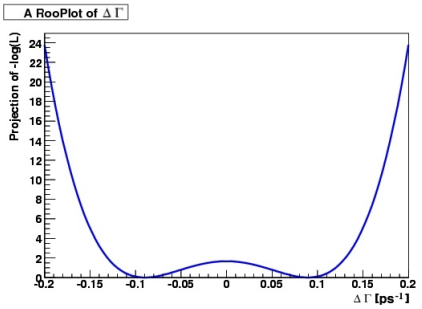

Figure 4: The NLL curve of $\Delta\Gamma_s$ at $\bar{\Gamma}_s = 0.7$. It is symmetric about zero and in this data set a small central peak results, giving two symmetric troughs with minima at $\Delta\Gamma_s = \pm 0.09$. The input value of $\Delta\Gamma_s$ is $+0.1$.

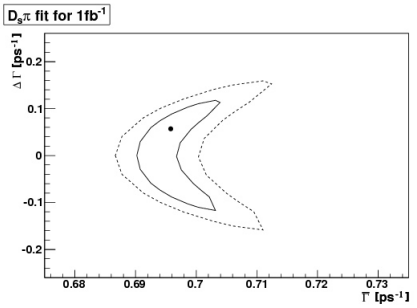

Figure 7: The 2d NLL contour plot corresponding to Figure 4. The solid line is 1σ and the dotted line is 2σ. The minimum of $\Delta\Gamma_s$ is now not at zero. The contours are still symmetric about zero because the bump is lower than the 1σ contour height.

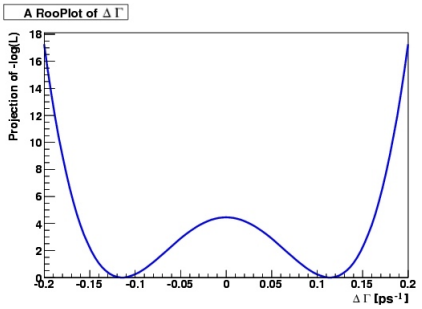

Figure 5: The NLL curve of $\Delta\Gamma_s$ at $\bar{\Gamma}_s = 0.7$. It is symmetric about zero and in this data set a slightly larger central peak results, giving two symmetric troughs with minima at $\Delta\Gamma_s = \pm 0.13$; the input value of $\Delta\Gamma_s$ is $+0.1$.

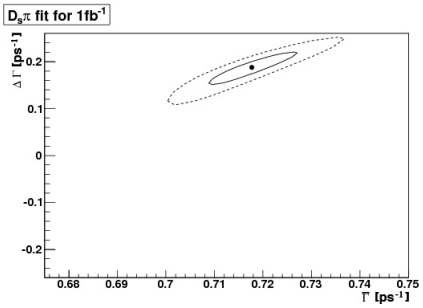

Figure 8: The 2d NLL contour plot corresponding to Figure 5. The solid line is 1σ and the dotted line is 2σ. The contours are now not symmetrical about about zero as the 1σ and 2σ boundaries are now constrained within one trough of $\Delta\Gamma_s$'s NLL. This results in a precision on $\Delta\Gamma_s$ that cannot be believed.

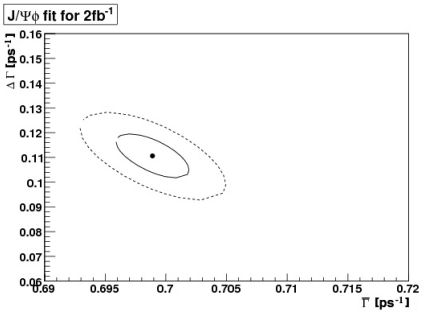

Figure 9: The 2d NLL contour plot between free parameters $\bar{\Gamma}_s$ and $\Delta\Gamma_s$. The solid line is 1σ and the dotted line is 2σ, the best fit is represented by the marker.

	R_0	$R_\perp$	$\Delta\Gamma_s$	$\bar{\Gamma}_s$
R_0	1.00	-0.58	0.16	-0.16
$R_\perp$	-0.58	1.00	-0.65	0.48
$\Delta\Gamma_s$	0.17	-0.65	1.00	-0.64
$\bar{\Gamma}_s$	-0.16	0.48	-0.64	1.00

Table 6: The correlation matrix of parameters in a simultaneous fit to $\bar{\Gamma}_s$, $\Delta\Gamma_s$, $R_\perp$ and R_0, this fit is performed using information from $B_s \to J/\psi\phi$ only.

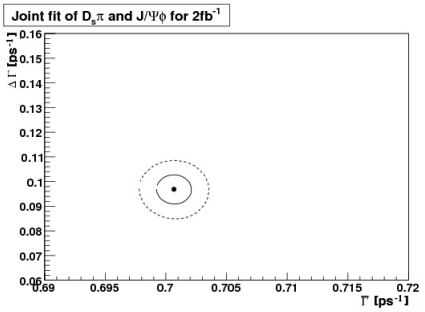

Figure 10: The 2d NLL contour plot between free parameters $\bar{\Gamma}_s$ and $\Delta\Gamma_s$. The solid line is 1σ and the dotted line is 2σ, the best fit is represented by the marker.

	R_0	$R_\perp$	$\Delta\Gamma_s$	$\bar{\Gamma}_s$
R_0	1.0	-0.58	0.07	-0.05
$R_\perp$	-0.58	1.0	-0.47	0.07
$\Delta\Gamma_s$	0.07	-0.47	1.0	0.00
$\bar{\Gamma}_s$	-0.05	0.07	0.00	1.0

Table 7: The correlation matrix of parameters in a simultaneous fit to $\bar{\Gamma}_s$, $\Delta\Gamma_s$, $R_\perp$ and R_0, this fit is performed using information from both channels.

4 Detector Effects

4.1 Resolution, Acceptance and Background

4.1.1 Including Resolution

The proper time resolution of $B_s \to D_s\pi$ in $LHCb$ is modelled by a single Gaussian of $\sigma_{core} = 33fs$ and the proper time resolution of $B_s \to J/\psi\phi$ in $LHCb$ is modelled by a single gaussian of $\sigma_{core} = 30fs$ for simplicity. The resolution effect in $B_s \to D_s\pi$ is shown in the propertime distribution in Figure 11.

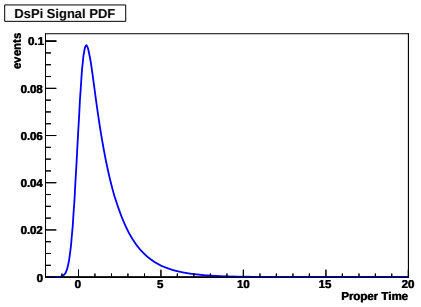

Figure 11: $B_s \to D_s\pi$ PDF with resolution.

4.1.2 Including Acceptance

The $B_s \to D_s\pi$ selection efficiency is a function of propertime. This non-flat acceptance function is of the form [7],

$$A(\tau) = \frac{(s_{low} * \tau)^{\eta}}{1 + (s_{low} * \tau)^{\eta}}(1 + s_{high} * \tau) \tag{8}$$

where s_{high} and s_{low} are two slope parameters.

For events after off-line acceptance and the trigger the parameters are:

s_{low}	=	$2.83ps^{-1}$
s_{high}	=	$0.0014ps^{-1}$
η	=	2.4

Table 8: $B_s \to D_s\pi$ PT Acceptance parameters.

This acceptance function is shown in Figure 12 and the $B_s \to D_s\pi$ PDF with acceptance in Figure 13. Events with small propertime are not reconstructed efficiently due to the requirement of $B_s \to D_s\pi$ events to have a displaced vertex.

For $B_s \to J/\psi\phi$ the actual cuts which will be used on the day of analysis cannot be known for certain now, but the emerging selection may well not include any cuts which significantly bias the propertime distribution. $B_s \to J/\psi\phi$ is not triggered on the displaced vertex for simplicity we therefore assume a perfect propertime acceptance for this channel.

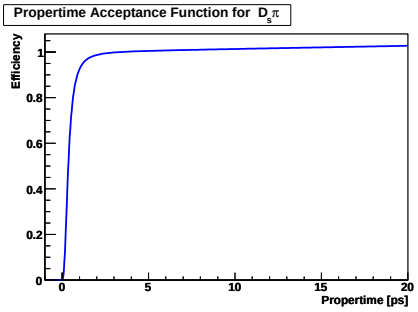

Figure 12: Propertime acceptance efficiency for $B_s \to D_s\pi$.

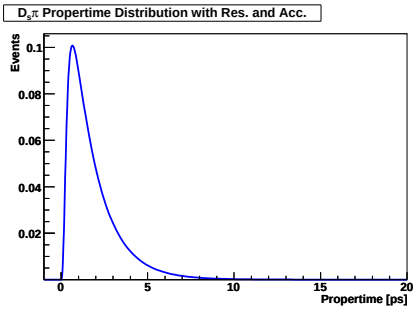

Figure 13: $B_s \to D_s\pi$ PDF with propertime acceptance efficiency.

Decay Channel	B/S
$B_d \to D^-\pi^+$	0.044 ± 0.014
$B_s^0 \to D_s^{\mp}K^{\pm}$	0.013 ± 0.003
$B_s^0 \to D_s^-\ell^+\nu X$	< 0.02 at 90% CL
$B_s^0 \to D_s^{*-}\pi^+$	< 0.004 at 90% CL
$B_s^0 \to S_s^-\rho^+$	< 0.002 at 90% CL

Table 9: Specific background contributions for $B_s \to D_s\pi$ [7].

4.1.3 Including Background

For $B_s \to D_s\pi$ decay $b\bar{b}$ quark pairs are the main source of background. Due to their displaced vertex the events are readily accepted by the trigger. Table 9 shows specific backgrounds for this channel [7].

After the trigger only combinatorial backgrounds are reconstructed for $B_s \to D_s\pi$ giving a background of 0.05 (90% CL). Table 9 shows that the background is mainly from $B_d \to D^-\pi^+$. The MC toy study approximates the background on $B_s \to D_s\pi$ to include only this background at 5% of events, it is modelled as a single exponential decay with the lifetime of the B_d meson.

For the $B_s \to J/\psi\phi$ channel the background is divided in to a prompt and long-lived exponential background. The signal and background ratios are given in Table 10. The prompt background is a delta function convoluted with propertime resolution and the long-lived background is an exponential with a lifetime of 0.36 ps [8].

For the purposes of the MC toy, only the prompt background was considered as this is the most dominant.

	fraction of sample
Signal	0.33
Prompt	0.60
Exponential	0.067

Table 10: The background and signal fractions for $B_s \to J/\psi\phi$ [8].

4.2 MC Toy Study

Detector effects were added to the MC Toy study of the previous section. All input values remained the same and detector effects were modelled as previousy described.

The fitting precision obtained when all detector effects are included is sumarised in tables 11 and 12. It is worth noting that in all cases we still use the same number of accepted events whether acceptance is applied in the PDF or not.

Throughout this study ROOT v5/12.00 was used. This is due to the later versions available not fitting correctly with the inclusion of an acceptance function.

# $J/\phi\psi$ events	# $D_s\pi$ events	Ideal $[ps^{-1}]$	w. res. and acc. $[ps^{-1}]$	w. background $[ps^{-1}]$
100k	140k	5.64×10^{-3}	5.50×10^{-3}	6.53×10^{-3}
10k	14k	1.79×10^{-2}	1.76×10^{-2}	2.09×10^{-2}
1k	1.4k	5.77×10^{-2}	5.73×10^{-2}	7.11×10^{-2}

Table 11: Average precision of $\Delta\Gamma_s$ obtained as detector effects are cumulatively added for a simultaneous fit of $\Delta\Gamma_s$ and $\bar{\Gamma}_s$ using the combination of both channels.

# $J/\phi\psi$ events	# $D_s\pi$ events	Ideal $[ps^{-1}]$	w. res. and acc. $[ps^{-1}]$	w. background $[ps^{-1}]$
100k	140k	1.44×10^{-3}	1.42×10^{-3}	2.47×10^{-3}
10k	14k	4.56×10^{-3}	4.51×10^{-3}	7.87×10^{-3}
1k	1.4k	1.48×10^{-2}	1.45×10^{-2}	2.76×10^{-2}

Table 12: Average precision of $\bar{\Gamma}_s$ obtained as detector effects are cumulatively added for a simultaneous fit of $\Delta\Gamma_s$ and $\bar{\Gamma}_s$ using the combination of both channels.

Tables 11 and 12 show the break down of results as each detector effect is added. On both parameters the effect of resolution is negligable whereas acceptance appears to increase the presicion obtained, however as the number of accepted events was kept constant this is not an important feature. With all detector effects considered the precison on $\bar{\Gamma}_s$ is decreased by a factor of 1.7 from the ideal, and the precison on $\Delta\Gamma_s$ is decreased by 1.2 from the ideal study.

4.3 DC06 signal study

The previous sections presented the expected sensitivity on a measurement of $\Delta\Gamma_s$ and $\bar{\Gamma}_s$ from individual and joint likelihood fits to toy Monte-Carlo events from $B_s \to D_s\pi$ and $B_s \to J/\psi\phi$ decays. In this section, we present the results of our sensitivity studies when fitting to candidate B_s^0 events selected from fully simulated $B_s \to D_s\pi$ and $B_s \to J/\psi\phi$ signal samples which were generated using the 2006 $LHCb$ geometry conditions. We use the same PDFs as were described in the previous sections.

The aim of this study is to show that the results remain valid when derived from fully simulated events. In this study we have not included background.

4.3.1 Selection

The DC06 data that was used in this study was selected by running DaVinci v20r3 over the stripped $B_s \to J/\psi\phi$ and $B_s \to D_s\pi$ signal samples. The standard selection code was used.

4.3.2 Combined fit

A resolution of $30fs$ was assumed for $B_s \to J/\psi\phi$ and $33fs$ for $B_s \to D_s\pi$ in the PDF. The acceptance function as described in Section 4.1.2 was used for $B_s \to D_s\pi$. There was no acceptance function on $B_s \to J/\psi\phi$.

Tables 13 and 14 show the precision obtained for $\Delta\Gamma_s$ and $\bar{\Gamma}_s$ respectivly, in a simultaneous fit of $\Delta\Gamma_s$ and $\bar{\Gamma}_s$. The event numbers correspond to the equivelent events in $0.2fb^{-1}$ and $0.02fb^{-1}$ os data, there were not enough events avaliable to perform the same study at $2fb^{-1}$. The tables

compare the precisons with those obtained in the toy study in section 4.2, the toy study resoluts include both propertime acceptance and resolution.

The individual fit projections are shown in Figures 14 and 15. The data points represent the generated data, the solid line is the fit to the data. The correlation of the floating parameters is given in Table 15.

# $J/\phi\psi$ events	# $D_s\pi$ events	Toy Study $[ps^{-1}]$	Fully Simulated Data $[ps^{-1}]$
10k	14k	1.76×10^{-2}	1.91×10^{-2}
1k	1.4k	5.73×10^{-2}	6.30×10^{-2}

Table 13: Comparision of precisions of $\Delta\Gamma_s$ obtained using MC Toys and fully simulated data under equivlent conditions and event numbers

# $J/\phi\psi$ events	# $D_s\pi$ events	Toy Study $[ps^{-1}]$	Fully Simulated Data $[ps^{-1}]$
10k	14k	4.51×10^{-3}	4.59×10^{-3}
1k	1.4k	1.45×10^{-2}	1.42×10^{-2}

Table 14: Comparision of precisions of $\bar{\Gamma}_s$ obtained using MC Toys and fully simulated data under equivlent conditions and event numbers

	R_0	$R_\perp$	$\Delta\Gamma_s$	$\bar{\Gamma}_s$
R_0	1.00	-0.68	0.14	-0.06
$R_\perp$	-0.68	1.00	-0.45	0.14
$\Delta\Gamma_s$	0.14	-0.45	1.00	-0.22
$\bar{\Gamma}_s$	-0.06	0.14	-0.22	1.00

Table 15: Correlation Matrix for a fit of $\Delta\Gamma_s$, $\bar{\Gamma}_s$, $R_\perp$ and R_0 in DC06 data with 10,000 $B_s \to J/\psi\phi$ events and 14,000 $B_s \to D_s\pi$ events.

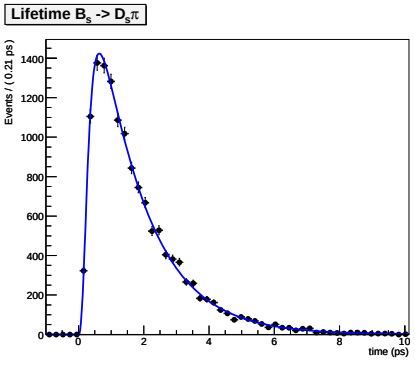

Figure 14: $B_s \to D_s\pi$ with 14000 signal events.

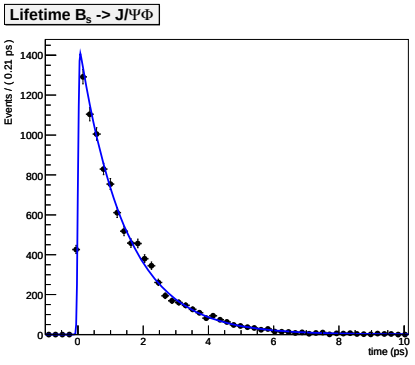

Figure 15: $B_s \to J/\psi\phi$ with 10000 signal events.

5 Conclusion

In this note we have quantified the power of simultaneously using the flavour specific $B_s \to D_s\pi$ channel and the CP eigenstate admixture $B_s \to J/\psi\phi$ channel to measure $\bar{\Gamma}_s$ and $\Delta\Gamma_s$ at $LHCb$ with differing integrated luminosities in the early years. We have shown that the flavour specific channels alone can only measure $\bar{\Gamma}_s$ with any precision and cannot usefully measure $\Delta\Gamma_s$. Importantly the systematic error introduced to $\bar{\Gamma}_s$ by ignoring $\Delta\Gamma_s$ in this channel is similar to the statistical precision. Thus to utilise the information in the $B_s \to D_s\pi$ channel requires an external constraint on $\Delta\Gamma_s$.

In contrast the $B_s \to J/\psi\phi$ channel can measure both parameters simultaneously albeit with an correlation of -0.75. However, the combination of the two channels improves the measurement of both parameters and reduces the correlation to around -0.22, as taken from the DC06 fits. The message of the note is that the best precision on both parameters at $LHCb$ can only be obtained by a simultaneous fit to properly account for the correlations [a].

We find that for a luminosity corresponding to approximately $0.2fb^{-1}$ the precisions (ignoring detector effects) on $\bar{\Gamma}_s$ and $\Delta\Gamma_s$ are 9.56×10^{-3} and 2.79×10^{-2} respectively from the $B_s \to J/\psi\phi$ channel alone and 4.56×10^{-3} and 1.79×10^{-2} respectively when both channels are combined as described.

According to the MC toy studies, when taking in to account detector effects and background the precison obtainable in $0.2fb^{-1}$ of data for $\bar{\Gamma}_s$ and $\Delta\Gamma_s$ is 7.87×10^{-3} and 2.09×10^{-2} respectively when using the combined fit.

[a] or by a complicated multi-dimensional parameterisation of the likelihood surfaces from each fit done separately and then combined

6 References

[1] HFAG. *Averages of b-hadron Properties at the End of 2007*, 2008.

[2] A.Lenz; U.Nierste. *Theoretical Update of $B_s - \bar{B}_s$ mixing*, 2006.

[3] Peter Clarke; Colin McLean; Andres Osorio. *LHCb-2007-101*. LHCb note.

[4] Vladimir Vava Gligorov. *Measurement of the CKM angle and B meson lifetimes at the LHCb detector*. PhD thesis, St. John's College Oxford, 2007.

[5] V. V. Gligorov; J. Rademacker. *2007-053*. LHCb.

[6] I.Dunietz. *B_s- $\bar{B}_s$ Mixing, CP Violation and Extraction of CKM Phases from Untagged Bs Data Samples*. *Physical Review D*, 52:3048, 1995.

[7] Jeremie Borel; Louis Nicolas; Olivier Schneider; Jeroen Van Hunend. *LHCb-2007-017*. LHCb note.

[8] Olivier Leroy. *$J/\psi\phi$ mixing parameters v1*, 05 2008.

A Transformations between $(\bar{\Gamma}_s, \Delta\Gamma_s)$ and (Γ_L, Γ_H)

The two parameter sets $[\bar{\Gamma}_s, \Delta\Gamma_s]$ and $[\Gamma_L, \Gamma_H]$ are related by a simple parameter transformation $\bar{\Gamma}_s = \frac{1}{2}(\Gamma_L + \Gamma_H)$ and $\Delta\Gamma_s = \Gamma_L - \Gamma_H$. It is often easier to visualise the errors and correlations on $[\Gamma_L, \Gamma_H]$ but we are interested in understanding our precision on $\Delta\Gamma_s$ in terms of the precision of Γ_L and Γ_H. Therefore we explore here the relation between the two.

For two sets of parameters [X,Y] and [A,B] related by a parmeter transformation the following relation holds:

$$\sigma_x^2 = \Big(\frac{\partial X}{\partial A}\Big)^2 \sigma_a^2 + \Big(\frac{\partial X}{\partial B}\Big)^2 \sigma_b^2 + 2\frac{\partial X}{\partial A}\frac{\partial X}{\partial B}\sigma_a\sigma_b\,\rho_{ab} \tag{9}$$

$$\sigma_y^2 = \Big(\frac{\partial Y}{\partial A}\Big)^2 \sigma_a^2 + \Big(\frac{\partial Y}{\partial B}\Big)^2 \sigma_b^2 + 2\frac{\partial Y}{\partial A}\frac{\partial Y}{\partial B}\sigma_a\sigma_b\,\rho_{ab} \tag{10}$$

$$\sigma_x\sigma_y\,\rho_{xy} = \frac{\partial X}{\partial A}\frac{\partial Y}{\partial A}\sigma_a^2 + \frac{\partial X}{\partial B}\frac{\partial Y}{\partial B}\sigma_b^2 + \Big(\frac{\partial X}{\partial A}\frac{\partial Y}{\partial B} + \frac{\partial X}{\partial B}\frac{\partial Y}{\partial A}\Big)\sigma_a\sigma_b\,\rho_{ab} \tag{11}$$

where σ_i is the error on parameter i and ρ_{ij} is the correlation coefficient between parameters i and j.

With $[X, Y] = [\bar{\Gamma}_s, \Delta\Gamma_s]$ and $[A, B] = [\Gamma_L, \Gamma_H]$ the derivatives are trivial yielding:

$$\sigma_{\bar{\Gamma}}^2 = \frac{1}{4}(\sigma_{\Gamma_L}^2 + \sigma_{\Gamma_H}^2 + 2\sigma_{\Gamma_L}\sigma_{\Gamma_H}\,\rho_{\Gamma_L,\Gamma_H}) \tag{12}$$

$$\sigma_{\Delta\Gamma}^2 = \sigma_{\Gamma_L}^2 + \sigma_{\Gamma_H}^2 - 2\sigma_{\Gamma_L}\sigma_{\Gamma_H}\,\rho_{\Gamma_L,\Gamma_H} \tag{13}$$

$$\rho_{\bar{\Gamma},\Delta\Gamma} = \frac{(\sigma_{\Gamma_L}^2 - \sigma_{\Gamma_H}^2)}{2\sigma_{\bar{\Gamma}}\sigma_{\Delta\Gamma}} \tag{14}$$

Using there (less complicated than they look) expressions we can now understand what drives the errors and correlations on $\Delta\Gamma_s$.

B Understanding correlations

B.1 Understanding correlations in $B_s \to D_s\pi$

The expression for the time evolution of the $B_s \to D_s\pi$ channel (untagged) is given by Equation 4. In essence it is the sum of two exponentials with decay constants Γ_L and Γ_H. To a first approximation, for small $\Delta\Gamma_s$, the overall time distribution looks approximately like a single exponential with average decay constant $\bar{\Gamma}_s = \frac{1}{2}(\Gamma_L + \Gamma_H)$. In the simplest picture a given set of data may be thought of as "fixing" $\bar{\Gamma}_s$ and if we fit for it alone we might expect it to be well determined. It follows that if instead we fit for Γ_L and Γ_H simultaneously then we would expect a large negative correlation between them to maintain a fixed central value for $\bar{\Gamma}_s$.

It is somewhat difficult to guess the correlation between $\bar{\Gamma}_s$ and $\Delta\Gamma_s$ when fiting for both simultaneously, and as we show below it is varies considerably depending upon central values.

We show how to predict the errors and correlation for the $[\bar{\Gamma}_s, \Delta\Gamma_s]$ set from a parameter transformation on those for the $[\Gamma_L, \Gamma_H]$ set. Broadly we see that:

- The large negative correlation between $[\Gamma_L, \Gamma_H]$ tends to give a small error for $\bar{\Gamma}_s$ and a large error for $\Delta\Gamma_s$.
- If the errors on $[\Gamma_L, \Gamma_H]$ are similar then the correlation between $[\bar{\Gamma}_s, \Delta\Gamma_s]$ is expected to be very small.

σ_{Γ_L}	σ_{Γ_H}	ρ_{Γ_L,Γ_H}		$\sigma_{\bar{\Gamma}}$	$\sigma_{\Delta\Gamma}$	$\rho_{\bar{\Gamma},\Delta\Gamma}$
For case $\Gamma_L = \Gamma_H = 0.7$						
0.044	0.044	-0.99	$\to$	**0.003**	**0.087**	**0.00**
				0.003	0.060	0.19
For case $\Gamma_L = 0.75$, $\Gamma_H = 0.65$						
0.025	0.015	-0.95	$\to$	**0.006**	**0.040**	**0.91**
				0.007	0.047	0.93
For case $\Gamma_L = 0.65$, $\Gamma_H = 0.75$						
0.014	0.025	-0.96	$\to$	**0.006**	**0.038**	**-0.91**
				0.006	0.031	-0.90

Table 16: Errors and correlations in fits to toy MC $B_s \to D_s\pi$ data. The numbers are for fits for two distinct parameter sets. The first (on left) is $[\Gamma_L, \Gamma_H]$. The second (on right) is $[\bar{\Gamma}_s, \Delta\Gamma_s]$. The numbers in bold on the right are not from a fit, but from a parameter transform on the direct fit numbers on the left.

- If the error on Γ_L is larger than the error on Γ_H then the correlation between $[\bar{\Gamma}_s, \Delta\Gamma_s]$ is expected to be positive.
- If the error on Γ_L is smaller than the error on Γ_H then the correlation between $[\bar{\Gamma}_s, \Delta\Gamma_s]$ is expected to be negative.

We have tested these predictions. In Table 16 we show the errors and correlation resulting from (i) toy MC fits for $[\Gamma_L, \Gamma_H]$, (ii) predictions for $[\bar{\Gamma}_s, \Delta\Gamma_s]$ using the parameter transformations and (ii) toy MC fits for $[\bar{\Gamma}_s, \Delta\Gamma_s]$. We do this for three cases, $\Gamma_L = \Gamma_H$, $\Gamma_L > \Gamma_H$, $\Gamma_L < \Gamma_H$. We run 5 fits and take a naive average for all numbers. We observe the following:

- The reported errors on $[\Gamma_L, \Gamma_H]$ in all cases had a large spread indicating (as we knew) that the fit is not particularly well behaved, i.e. this is not a good channel for a simultaneous fit.
- The correlation between $[\Gamma_L, \Gamma_H]$ is large and negative as expected.
- For both the cases where $\Gamma_L \neq \Gamma_H$ the errors on each become unequal. We then see good agreement between the prediction and the direct fits for the error on $\bar{\Gamma}_s$ and the correlation between $[\bar{\Gamma}_s, \Delta\Gamma_s]$. In particular the sign and magnitude of the correlation is exactly as expected.
- For the case where $\Gamma_L = \Gamma_H$ the situation was not so nice. The direct fit results varied widely and close inspection suggested there were two "fit points", one where the error and correlation agree roughly with prediction and another where they do not. This is simply a manifestation of the very non parabolic nature of the NLL.
- The error on $\Delta\Gamma_s$ is in all cases poorly constrained (we say more on this later in the context of the NLL scan).

Overall we observe quite good agreement, at least qualitatively, supporting the simplistic picture we have presented. The broad stable conclusions are that:

- The correlation between $[\Gamma_L, \Gamma_H]$ is large and negative.
- $\bar{\Gamma}_s$ is reasonably constrained but $\Delta\Gamma_s$ is not and this is not a good channel for a simultaneous fit.
- The correlation between $[\bar{\Gamma}_s, \Delta\Gamma_s]$ varies enormously depending upon central values.
- The correlation between $[\bar{\Gamma}_s, \Delta\Gamma_s]$ is mainly driven by the difference between the errors on $[\Gamma_L, \Gamma_H]$ and not by the correlation between them.

B.2 Understanding correlations in $B_s \to J/\psi\phi$

The expression for the time evolution of decays in the $B_s \to J/\psi\phi$ channel are given in $LHCb$ physics note [3]. Let us consider the simplest case of untagged events and set $\phi_s = 0$ which is close to the SM expectation (Equation 7).

If the decay angular information were able to completely separate the CP-even eigenstates (CP+1) from the CP-odd eigenstates (CP-1), then this channel would make independent measurements of Γ_L (from the CP+1 component) and Γ_H (from the CP-1 component) with zero correlation. In practice the separation is not perfect and there is some mixture of two exponentials, i.e. there is an element looking more like $A\exp(-\Gamma_L t)+B\exp(-\Gamma_H t)$ for which we expect a negative correlation coefficient for the same reasons as in $B_s \to D_s\pi$.

Both the relative size of errors on Γ_L and Γ_H and the size of the correlation depend in detail upon upon $R_\perp$, the fraction of CP-1 eigenstate present . For example, the SM expectation of $R_\perp = 0.2$ means there is more of the CP+1 eigenstate present than the CP-1 and hence we expect Γ_L to have a smaller error than Γ_H.

The left hand set of numbers in Table 17 shows direct fits to 100,000 toy MC events for $[\Gamma_L, \Gamma_H]$. The first two rows show results for (i) $R_\perp = 0.2$ fixed (ii) $R_\perp = 0.2$ a free fit parameter. As expected Γ_L is measured better than Γ_H and there is a negative correlation with magnitude less than 1. The correlation is naturally greater with extra free parameters. The next few rows illustrate how things change if $R_\perp$ is changed. We see a systematic change in the relative size of the errors although perhaps surprisingly the correlation remains unchanged.

The right hand numbers show how we can interpret the information for the $[\bar{\Gamma}_s, \Delta\Gamma_s]$ parameter set. As before the numbers in italics are obtained using the parameter transformation expressions whereas the second set are obtained from direct fits. The values agree well. The sign and magnitude of the correlation between $[\bar{\Gamma}_s, \Delta\Gamma_s]$ is driven by the value of $\sigma^2_{\Gamma_L} - \sigma^2_{\Gamma_H}$. Note the clearly understandable evolution as $R_\perp$ is changed from 0.05 to 0.95. The errors on both $[\bar{\Gamma}_s, \Delta\Gamma_s]$ are minimal when $R_\perp = 0.5$ and the magnitude and sign of the correlation evolves exactly as expected.

All of the above were carried out for $\Delta\Gamma_s = 0$.

In summary we can make the following observations:

- Both Γ_L and Γ_H are well measured as is $\bar{\Gamma}_s$. This is different from the $B_s \to D_s\pi$ case where both Γ_L and Γ_H are poorly measured due to the very high correlation but $\bar{\Gamma}_s$ is well measured.
- The error on Γ_L will be smaller than that in Γ_H if $R_\perp < 0.5$.
- The correlation ρ_{Γ_L,Γ_H} will always be negative but have magnitude less than 1 due to the separating power of the decay angles.
- The correlation $\rho_{\bar{\Gamma},\Delta\Gamma}$ will be negative if $R_\perp < 0.5$.
- The errors on $[\bar{\Gamma}_s, \Delta\Gamma_s]$ are mimimum for $R_\perp = 0.5$.

σ_{Γ_L}	σ_{Γ_H}	ρ_{Γ_L,Γ_H}		$\sigma_{\bar{\Gamma}}$	$\sigma_{\Delta\Gamma}$	$\rho_{\bar{\Gamma},\Delta\Gamma}$
For case $\Gamma_L = \Gamma_H = 0.7$ and $\phi_s = 0$, $R_\perp = 0.2$ fixed						
0.0026	0.0063	-0.22	$\to$	**0.0031**	**0.0074**	**-0.71**
				0.0031	0.0074	-0.71
For case $\Gamma_L = \Gamma_H = 0.7$ and $\phi_s = 0$, $R_\perp = 0.2$ free						
0.0030	0.0086	-0.46	$\to$	**0.0038**	**0.0103**	**-0.82**
				0.0038	0.0100	-0.69
For case $\Gamma_L = \Gamma_H = 0.7$ and $\phi_s = 0$, $R_\perp = 0.05, 0.2, 0.5, 0.8, 0.95$ fixed						
0.0024	0.0164	-0.24	$\to$	**0.0080**	**0.0171**	**-0.96**
				0.0078	0.0168	-0.96
0.0026	0.0063	-0.22	$\to$	**0.0031**	**0.0074**	**-0.71**
				0.0031	0.0074	-0.71
0.0036	0.0037	-0.25	$\to$	**0.0022**	**0.0058**	**0.00**
				0.0022	0.0057	0.00
0.0065	0.0028	-0.28	$\to$	**0.0031**	**0.0077**	**0.71**
				0.0033	0.0081	0.75
0.0168	0.0028	-0.28	$\to$	**0.0082**	**0.0175**	**0.96**
				0.0083	0.0179	0.96

Table 17: Errors and correlations in fits to 100,000 toy MC $B_s \to J/\psi\phi$ data. The numbers are for fits for two distinct parameter sets. The first (on left) is $[\Gamma_L, \Gamma_H]$. The second (on right) is $[\bar{\Gamma}_s, \Delta\Gamma_s]$. The numbers in bold on the right are not from a fit, but from a parameter transformations on the direct fit numbers on the left.

B.3 Understanding correlations in the combined channels

A study between the correlations obtained through various ratios of event numbers for $B_s \to J/\psi\phi$ and $B_s \to D_s\pi$ was performed. The fits were performed both to MC toy data and to DC06. Propertime resolution and acceptance were applied for all the fits. The number of events was limited by the avalibility of DC06 data and so low statistics account for the differences obtained between DC06 and MC toys.

Tables 18 - 27 show the results from this study. The correlation difference between the MC toy fits and the DC06 fits is within 10% and so is considered negligible.

The differences seen in the correlations between fits using the same ratio of $B_s \to D_s\pi$ events to $B_s \to J/\psi\phi$ events but with different overall numbers of events is due to statistical fluctuations caused by the low input values.

It is clear that the ratio of events significantly affects the correlation between $\bar{\Gamma}_s$ and $\Delta\Gamma_s$. In this note it is assumed $140,000$ $B_s \to D_s\pi$ events and $100,000$ $B_s \to J/\psi\phi$ events will be the ratio in a nominal year, however this is not confirmed until data taking begins.

	R_0	$R_\perp$	$\Delta\Gamma_s$	$\bar{\Gamma}_s$
R_0	1.00	-0.59	0.05	-0.05
$R_\perp$	-0.59	1.00	-0.44	0.08
$\Delta\Gamma_s$	0.05	-0.44	1.00	-0.03
$\bar{\Gamma}_s$	-0.05	0.08	-0.03	1.00

Table 18: MC toy data, 1,000 $B_s \to J/\psi\phi$ events, 1,400 $B_s \to D_s\pi$ events.

	R_0	$R_\perp$	$\Delta\Gamma_s$	$\bar{\Gamma}_s$
R_0	1.00	-0.68	0.23	-0.06
$R_\perp$	-0.68	1.00	-0.57	0.09
$\Delta\Gamma_s$	0.23	-0.57	1.00	-0.06
$\bar{\Gamma}_s$	-0.06	0.09	-0.06	1.00

Table 19: DC06 data, 1,000 $B_s \to J/\psi\phi$ events, 1,400 $B_s \to D_s\pi$ events.

	R_0	$R_\perp$	$\Delta\Gamma_s$	$\bar{\Gamma}_s$
R_0	1.00	-0.58	0.07	-0.04
$R_\perp$	-0.58	1.00	-0.47	0.05
$\Delta\Gamma_s$	0.07	-0.47	1.00	0.03
$\bar{\Gamma}_s$	-0.04	0.05	0.03	1.00

Table 20: MC toy data, 10,000 $B_s \to J/\psi\phi$ events, 14,000 $B_s \to D_s\pi$ events.

	R_0	$R_\perp$	$\Delta\Gamma_s$	$\bar{\Gamma}_s$
R_0	1.00	-0.68	0.14	-0.06
$R_\perp$	-0.68	1.00	-0.45	0.14
$\Delta\Gamma_s$	0.14	-0.45	1.00	-0.22
$\bar{\Gamma}_s$	-0.06	0.14	-0.22	1.00

Table 21: DC06 data, 10,000 $B_s \to J/\psi\phi$ events, 14,000 $B_s \to D_s\pi$ events.

	R_0	$R_\perp$	$\Delta\Gamma_s$	$\bar{\Gamma}_s$
R_0	1.00	-0.58	0.16	-0.16
$R_\perp$	-0.58	1.00	-0.65	0.48
$\Delta\Gamma_s$	0.17	-0.65	1.00	-0.64
$\bar{\Gamma}_s$	-0.16	0.48	-0.64	1.00

Table 22: MC toy data, 10,000 $B_s \to J/\psi\phi$ events, 0 $B_s \to D_s\pi$ events.

	R_0	$R_\perp$	$\Delta\Gamma_s$	$\bar{\Gamma}_s$
R_0	1.00	-0.68	0.27	-0.23
$R_\perp$	-0.68	1.00	-0.66	0.53
$\Delta\Gamma_s$	0.27	-0.66	1.00	-0.75
$\bar{\Gamma}_s$	-0.23	0.53	-0.75	1.00

Table 23: DC06 data, 10,000 $B_s \to J/\psi\phi$ events, 0 $B_s \to D_s\pi$ events.

	R_0	$R_\perp$	$\Delta\Gamma_s$	$\bar{\Gamma}_s$
R_0	1.00	-0.58	0.08	-0.06
$R_\perp$	-0.58	1.00	-0.50	0.15
$\Delta\Gamma_s$	0.08	-0.50	1.00	-0.16
$\bar{\Gamma}_s$	-0.06	0.15	-0.16	1.00

Table 24: MC toy data, 10,000 $B_s \to J/\psi\phi$ events, 8,000 $B_s \to D_s\pi$ events.

	R_0	$R_\perp$	$\Delta\Gamma_s$	$\bar{\Gamma}_s$
R_0	1.00	-0.68	0.16	-0.09
$R_\perp$	-0.68	1.00	-0.48	0.20
$\Delta\Gamma_s$	0.16	-0.48	1.00	-0.31
$\bar{\Gamma}_s$	-0.09	0.20	-0.31	1.00

Table 25: DC06 data, 10,000 $B_s \to J/\psi\phi$ events, 8,000 $B_s \to D_s\pi$ events.

	R_0	$R_\perp$	$\Delta\Gamma_s$	$\bar{\Gamma}_s$
R_0	1.00	-0.58	0.08	-0.06
$R_\perp$	-0.58	1.00	-0.48	0.10
$\Delta\Gamma_s$	0.08	-0.48	1.00	-0.05
$\bar{\Gamma}_s$	-0.06	0.10	-0.05	1.00

Table 26: MC toy data, 10,000 $B_s \to J/\psi\phi$ events, 10,000 $B_s \to D_s\pi$ events.

	R_0	$R_\perp$	$\Delta\Gamma_s$	$\bar{\Gamma}_s$
R_0	1.00	-0.68	0.15	-0.08
$R_\perp$	-0.68	1.00	-0.47	0.17
$\Delta\Gamma_s$	0.15	-0.47	1.00	-0.27
$\bar{\Gamma}_s$	-0.08	0.17	-0.27	1.00

Table 27: DC06 data, 10,000 $B_s \to J/\psi\phi$ events, 10,000 $B_s \to D_s\pi$ events.

Bibliography

[1] T. Sjostrand, S. Mrenna, and P. Z. Skands, "Pythia 6.4 physics and manual," *JHEP* **0605** (2006) 026, hep-ph/0603175v2.

[2] J. J. Thomson, "Cathode Rays," *Philosophical Magazine* **44** (1897) 293.

[3] "Cern public web." http://public.web.cern.ch/public/.

[4] C. Lefèvre, "The cern accelerator complex," Dec, 2008. https://cdsweb.cern.ch/record/126045.

[5] AC Team, "Diagram of an LHC Dipole Magnet," June, 1999. https://cdsweb.cern.ch/record/40524.

[6] P. Ball, R. Fleischer, G. Tartarelli, P. Vikas, G. Wilkinson, *et al.*, "B decays at the LHC," arXiv:0003238 [hep-ph]. CERN-TH-2000-101.

[7] A. Augusto Alves Jr *et al.*, "The LHCb Detector at the LHC," *JINST* **3** (2008) S08005.

[8] S. Amato *et al.*, "LHCb Technical Proposal." CERN-LHCC-98-04, 1998.

[9] LHCb Collaboration, "LHCb VELO (VErtex LOcator): Technical Design Report." CERN-LHCC-2001-011, 2001.

[10] LHCb Collaboration, "LHCb Reoptimized Detector Design and Performance: Technical Design Report," tech. rep., CERN, 2003. CERN-LHCC-2003-030.

[11] The LHCb Silicon Tracker group, "LHCb Silicon Tracker." `http://www.physik.unizh.ch/groups/lhcb/public/material/`.

[12] LHCb Collaboration, "LHCb Inner Tracker: Technical Design Report." CERN-LHCC-2002-029, 2002.

[13] LHCb Collaboration, "LHCb Outer Tracker: Technical Design Report." CERN-LHCC-2001-024, 2001.

[14] M. Adinolfi *et al.*, "LHCb RICH 2 Engineering Design Review Report." LHCb-2002-009, 2002.

[15] LHCb Collaboration, "RICH Technical Design Report." CERN LHCC 2000-037, 2000.

[16] LHCb Collaboration, "LHCb Muon System: Technical Design Report." CERN-LHCC-2001-010, 2001.

[17] L. de Paula, "The LHCb Experiment," *Brazilian Journal of Physics* **30** (2000) 2.

[18] M. Williams and V. Gligorov and C. Thomas and H. Dijkstra and J. Nardulli and P. Spradlin, "The HLT2 Topological Lines." LHCb-PUB-2011-002, 2011.

[19] R. Aaij, "The lhcb trigger: present and future.," June, 2011.

[20] G. Barrand *et al.*, "GAUDI - A Software Architecture and Framework for building HEP Data Processing Applications," *Computer Physics Communications* **140** no. 1-2, (2001) 45–55.

[21] The LHCb Collaboration, "LHCb Computing Technical Design Report." CERN-LHCC-2005-019, 2005.

[22] D. Lange, "The EvtGen Particle Decay Simulation Package," *Nucl.Instrum.Meth.* **A462** (2001) 152.

[23] S. Agostinelli *et al.*, "GEANT4: A Simulation Toolkit.," *Nucl.Instrum.Meth.* **A506** (2003) 250.

[24] I. I. Bigi and A. J. Sanda, *CP Violation*. Cambrige University Press, 2 ed., 2010.

[25] I. I. Bigi and L. Moroni, *Heavy flavour physics: a probe of nature's grand design*. IOS Press, 1998.

[26] S. Uozumi, *Measurement of the B meson Lifetimes with the Collider Detector at Fermilab*. PhD thesis, University of Tsukuba, 2006.

[27] MuLan Collaboration, D. M. Webber *et al.*, "Measurement of the Positive Muon Lifetime and Determination of the Fermi Constant to Part-per-Million Precision," *Phys. Rev. Lett.* **106** (Jan, 2011) 041803. http://link.aps.org/doi/10.1103/PhysRevLett.106.041803.

[28] K. Nakamura *et al.*, "The Review of Particle Physics," *J. Phys. G* **37** no. 075021, (2010) . http://pdg.lbl.gov.

[29] S. Stone, *B Decays*. World Scientific, revised 2nd ed., 1994.

[30] U. Nierste, "CP asymmetry in flavor-specific B decays.," arXiv:0406300v2 [hep-ph]. FERMILAB-CONF-04-094-T.

[31] K. Anikeev, D. Atwood, F. Azfar, *et al.*, "B physics at the Tevatron: Run II and beyond," arXiv:0201071 [hep-ph]. FERMILAB-PUB-01-197.

[32] A.Lenz and U.Nierste, "Theoretical Update of $B_s - \bar{B}_s$ mixing," *Journal of High Energy Physics* **0607** (2007) 072, hep-ph/0612167v3.

[33] I.Dunietz, "B_s- $\bar{B}_s$ Mixing, CP Violation and Extraction of CKM Phases from Untagged B_s Data Samples," *Physical Review D* **52** (1995) 3048, arXiv:9501287 [hep-ph].

[34] I. Dunietz, R. Fleischer, and U. Nierste, "In pursuit of new physics with B_s decays," *Phys. Rev. D* **63** no. 11, (May, 2001) 114015.

[35] A.Lenz and U.Nierste, "Numerical updates of lifetimes and mixing parameters of B mesons," in *CKM2010 Proceedings, Warwick*. 2011. arXiv:1102.4274 [hep-ph].

[36] K. Hartkorn and H. Moser, "A new method of measuring $\frac{\Delta\Gamma}{\Gamma}$ in the $B_s^0\bar{B}_s^0$ system," *The European Physical Journal* **8** (1999) 381.

[37] R. Aaij *et al.*, "Measurement of the CP-violating phase ϕ_s in the decay $B_s \to J/\psi\phi$," *Phys. Rev. Lett.* **108** (2012) 101803, `arXiv:1112.3183 [hep-ex]`.

[38] J. Charles, O. Deschamps, S. Descotes-Genon, R. Itoh, H. Lacker, *et al.*, "Predictions of selected flavour observables within the Standard Model," *Phys. Rev. D* **84** (2011) 033005, `arXiv:1106.4041 [hep-ph]`.

[39] F. James and M. Roos, "'MINUIT' a System for Function Minimisation and Analysis of the Parameter Errors and Correlations," *Comput. Phys. Commun.* **10** (1975) 343–367.

[40] **Heavy Flavor Averaging Group** Collaboration, D. Asner *et al.*, "Averages of $b-$hadron, $c-$hadron, and $\tau-$lepton Properties," `arXiv:1010.1589 [hep-ex]`. `http://www.slac.stanford.edu/xorg/hfag`.

[41] V. V. Gligorov, "Reconstruction of the decay modes $B_d^0 \to D_d^{\pm}\pi^{\mp}$, $B_s^0 \to D_s^-\pi^+$, and $B_s^0 \to D_s^{\pm}K^{\mp}$ at LHCb." LHCb-PUB-2009-003, 2009.

[42] R. Aaij *et al.*, "Measurement of the $B_s^0 - \bar{B}_s^0$ oscillation frequency Δm_s in $B_s^0 \to D_s^-(3)\pi$ decays," *Physics Letters B* **709** (2012) 177, `hep-ex:1112.4311v1 [arXiv]`.

[43] A. Powell, "Particle Identification at LHCb," in *ICHEP 2010, Paris*. 2010. LHCb-PROC-2011-008.

[44] M. Gersabeck, V. V. Gligorov, J. Imong, and J. Rademacker, "A Monte Carlo simulation free method of measuring lifetime using event-by-event acceptance functions at LHCb." LHCb-PUB-2009-022, 2009.

[45] "b-hadron lifetime measurements with exclusive $B \to J/\psi X$ decays reconstructed in the 2010 data." LHCb-CONF-2011-001, March, 2011.

[46] V. V. Gligorov, *Measurement of the CKM angle γ and B meson lifetimes at the LHCb detector*. PhD thesis, St. John's College Oxford, 2007.

[47] B. LIU, *Measurements of the B meson production cross-sections at LHCb*. PhD thesis, Tsinghua University, 2012.

[48] J. Gaiser, "Charmoniom Spectroscopy from Radiative Decays of the J/ψ and ψ',". SLAC-0255.